Characterisation of Cobalt/Manganese Fischer-Tropsch Catalysts using *In Situ* Gas Cell Analytical Transmission Electron Microscopy

A thesis submitted to the University of Manchester
for the degree of Doctor of Philosophy in the
Faculty of Science and Engineering

2022

Matthew Lindley

School of Natural Sciences
Department of Materials

[Blank page]

Contents

Word count: 26,184

List of Figures

List of Abbreviations

ADF	Annular dark field
BF	Bright field
BFP	Back focal plane
CCD	Charge coupled device
CNF	Carbon nanofibre
CTEM	Conventional transmission electron microscope/microscopy
DED	Direct electron detector
DF	Dark field
DFT	Density functional theory
DP	Diffraction pattern
EDS	Energy dispersive x-ray spectroscopy
EELS	Electron energy-loss spectroscopy
E(S)TEM	Environmental (scanning) transmission electron microscope/microscopy
EXAFS	Extended x-ray absorption fine structure
FT	Fischer-Tropsch
GTL	Gas to liquid
HAADF	High-angle annular dark field
HDP	Homogeneous deposition precipitation
HEA	High entropy alloy
HRTEM	High resolution transmission electron microscope/microscopy
IWI	Incipient wetness impregnation
IR	Infra-red
LCF	Linear combination fitting
LPG	Liquid petroleum gas
MEMS	Micro electromechanical systems
MS	Mass spectrometer/spectrometry
MPG	Micropressure gauge
NP	Nanoparticle
ORR	Oxygen reduction reaction
PCTF	Phase contrast transfer function
ROI	Region of interest
RT	Room temperature
SAED	Selected area electron diffraction
SBR	Signal-to-background ratio
SEA	Strong electrostatic adsorption
SMSI	Strong metal-support interaction
SNR	Signal-to-noise ratio
SSITKA	Steady-state isotopic transient kinetic analysis
STEM	Scanning transmission electron microscope/microscopy
TEM	Transmission electron microscope/microscopy
TOF	Turnover frequency
TPR	Temperature programmed reduction

TWC	Three-way catalyst
WGS	Water gas shift
XANES	X-ray absorption near edge fine structure
XAS	X-ray absorption spectroscopy
XPS	X-ray photoelectron spectroscopy
XRD	X-ray diffraction
ZLP	Zero-loss peak

Abstract

The emergence of gas cell scanning transmission electron microscopy (STEM) has provided a platform for characterising the dynamic morphological, structural and chemical features of materials during exposure to gaseous environments at elevated temperatures. These developments have significant relevance to heterogeneous catalysis, where the adsorption/desorption processes of reactants and products can lead to dramatic changes in the dispersion and crystallographic nature of the system and, subsequently, the catalysts functionality.

In this work gas cell STEM has been used to investigate the effect of an H_2 reduction treatment on titania-supported, cobalt-based catalysts used industrially for Fischer-Tropsch (FT) synthesis of hydrocarbon fuels, including the impact of this treatment with the inclusion of a manganese promoter. Reduction treatments are an essential component of FT chemistry, as the starting calcined catalyst is typically in the form of cobalt oxide and is only catalytically active to FT synthesis when in its metallic form. *In situ* gas cell STEM observations, combined with energy dispersive x-ray spectroscopy (EDS) have demonstrated the dispersion-inducing effect of manganese and the consequence of its presence during the reduction process on the resulting particulate-formation of active cobalt catalyst.

This work also established some key limitations in using gas cell STEM, specifically when performing electron energy loss spectroscopy (EELS). The requirement of membrane windows to encapsulate the specimen and gas within the vacuum of the microscope effectively increases the extent of plural scattering, making observations of specimen core-loss edges challenging. The situation is made worse when considering additional effects, such as high dispersion, support thickness and large background peaks from the windows which reduce edge peak intensities signals to levels comparable to the spectrum noise. STEM-EELS observations have determined the significant extent of scatting is from the membranes windows and revealed a temperature dependent relationship of scattering from the encapsulated gas, arising from a decrease in gas density due to membrane bowing.

Declaration

No portion of the work referred to in the thesis has been submitted in support of an application for another degree or qualification of this or any other university or other institute of learning.

Copyright Statement

i. The author of this thesis (including any appendices and/or schedules to this thesis) owns certain copyright or related rights in it (the “Copyright") and s/he has given The University of Manchester certain rights to use such Copyright, including for administrative purposes.

ii. Copies of this thesis, either in full or in extracts and whether in hard or electronic copy, may be made only in accordance with the Copyright, Designs and Patents Act 1988 (as amended) and regulations issued under it or, where appropriate, in accordance with licensing agreements which the University has from time to time. This page must form part of any such copies made.

iii. The ownership of certain Copyright, patents, designs, trademarks and other intellectual property (the “Intellectual Property") and any reproductions of copyright works in the thesis, for example graphs and tables (“Reproductions", which may be described in this thesis, may not be owned by the author and may be owned by third parties. Such Intellectual Property and Reproductions cannot and must not be made available for use without the prior written permission of the owner(s) of the relevant Intellectual Property and/or Reproductions.

iv. Further information on the conditions under which disclosure, publication and commercialisation of this thesis, the Copyright and any Intellectual Property and/or Reproductions described in it may take place is available in the University IP Policy (see http://documents.manchester.ac.uk/DocuInfo.aspx?DocID=24420), in any relevant Thesis restriction declarations deposited in the University Library, The University Library’s regulations (see http://www.library.manchester.ac.uk/about/regulations) and in The University’s policy on Presentation of Theses.

Acknowledgements

I have been fortunate to work alongside some incredibly talented people during my PhD, many of whom generously gave their time in supporting the work presented in this thesis. So, before I start with names I would like to thank everyone for their contributions to this research and for the enjoyable time I had during this project.

Firstly, I would like to thank my supervisor. Prof Sarah Haigh, for her enduring support, enthusiasm and patience during this project. The Covid-19 pandemic brought many challenges, both in and outside of my academic studies and I am very grateful for the understanding and guidance she has provided throughout. I would like to thank my co-supervisor Prof Chris Hardacre, as well as Dr James Paterson and Mark Peacock for their roles as industrial supervisors, their inputs were invaluable at every stage of the project. I would also like to thank Matt Smith and Duc-The Ngo for training me on the various microscopes, particularly Matt, who has been instrumental in assisting with all practical aspects of in situ microscopy.

The skills I have gained during my PhD are in no small part due to the help from numerous members of the Materials Science and Chemical Engineering groups I have been part of: Drs Dan Kelly, Yichi Wang and Nick Clark I have to thank for guiding me on all matters in microscopy and data processing; Sarayute Chansai and Adam Greer, who were always there to provide catalysis advice; and Rongsheng Cai for sharing in frustrations when in situ experiments didn’t quite go as planned. I would like to extend my gratitude to all the members of both groups, past and present. I would also like to thank Dr Andrew Logsdail and Dr Pavel Stishenko for their DFT work during our collaborations, and everyone else I have had the privilege of collaborating with. It has been a pleasure working with all of you.

Project aside, I would like to thank my Mum, Karen, and my in laws Paul and Sue for their support, especially for their on-call childcare services. I would like to give a special mention to Max, Miles and Chloe, who made all the hard work worthwhile. Finally, a big thank you goes to my wife, Aimée, who has been an unwavering source of love and encouragement during the past 4 years.

List of Publications

Lindley, M., Stishenko, P., Crawley, J.W.M., Paterson, J., Hardacre, C., Logsdail, A.J., Haigh, S.J. Effect of Mn-promotion on the Reduction of Co-based Fischer-Tropsch Catalysts using *In Situ* Gas Cell Scanning Transmission Electron Microscopy. *In preparation.*

Lindley, M., Paterson, J., Hardacre, C., Haigh, S.J. Determining the Limits of Electron Energy-Loss Spectroscopy of Heterogeneous Catalysts during *In Situ* Gas Cell Scanning Transmission Electron Microscopy. *In preparation.*

Ye, Z., Li, C., Celentano, M., **Lindley, M.**, O'Reilly, T., Greer, A.J., Huang, Y., Hardacre, C., Haigh, S.J., Xu, Y., Bell, S.E.J. Surfactant-free Synthesis of Spikey Hollow Ag-Au Nanostars with Chemically Exposed Surfaces for Enhanced Catalysis and Single-particle SERS. *JACS Au* 2, 178-187 (2022).

Forster, L., D'Agostino, C., Llosa-Tanco, M.A., Spallina, V., Brencio, C., Gallucci, F., **Lindley, M.**, Haigh, S.J., Pacheco-Tanaka, D.A. (2021). Tailoring Pore Structure and Surface Chemistry of Microporous Alumina-Carbon Molecular Sieve Membranes (Al-CMSMs) by Altering Carbonization Temperature for Optimal Gas Separation Performance: An Investigation using Low-field NMR Relaxation Measurements. *Chem. Eng. J.* 424, 129313 (2021).

Bayram, V., Ghidiu, M., Byun, J.J., Rawson, S.D., Yang, P., Mcdonald, S.A., **Lindley, M.**, Fairclough, S., Haigh, S.J., Withers, P.J., Barsoum, M.W., Kinloch, I.A., Barg, S. MXene Tunable Lamellae Architectures for Supercapacitor Electrodes. *ACS Appl. Energy Mater.* 3, 411-422 (2020).

Kelly, D., Clark, N., Zhou, M., **Lindley, M.**, Lewis, E., Burke, M.G., Gorbachev, R.V., Haigh, S.J. Liquid-Phase STEM-EDS in Graphene and Silicon Nitride Cells. *Microscopy and Microanalysis*, *25*(S2), 1500-1501 (2019).

Chapter 1

Introduction

1.1. Project Objectives

The aim of this research project is to investigate the elemental redistribution and structural evolution of cobalt-based nanoparticle catalysts during exposure to reactive gas environments using recently developed *in situ* gas cell (scanning) transmission electron microscopy ((S)TEM). These catalysts are industrially important to the Fischer-Tropsch process: the synthesis of long-chain hydrocarbons, which can be processed to yield a range of clean fuels, such as petrol and diesel. It is already well understood that the size and morphology of cobalt nanoparticles is critical for their effective catalytic operation. Catalytic reaction testing has also shown that the addition of manganese can change the nanoparticle size distribution and shift selectivity from methane to commercially desirable C_{5+} products. Here, *in situ* STEM is used to provide observations into the relationship between cobalt and manganese distribution and their response during exposure to industrially relevant reaction processes. This offers the potential for new insights which will ultimately aid in the future design of Fischer-Tropsch catalysts. A parallel aim is to demonstrate the applications and limitations of the *in situ* gas cell, particularly when performing electron energy loss spectroscopy (EELS) on heavily dispersed materials, to establish the barriers which need to be overcome to achieve further technological advancements in the field.

1.2. Thesis Structure

The research in this thesis was undertaken as part of the International Centre for Advanced Materials (ICAM) at the University of Manchester, in collaboration with bp, during September 2017 to March 2022. The project was conceived to utilise relatively recent advances in *in situ* gas cell scanning transmission electron microscopy (STEM) and apply them to the study and development of heterogeneous catalysts important to Fischer-Tropsch synthesis. To put this work into context, a significant portion of this thesis is dedicated to reviewing the literature. Chapter 2 consists of an introduction to Fischer-Tropsch synthesis, on which a considerable amount of literature has been published. For brevity, this review has put focus on aspects relevant to this research project, i.e., the use of cobalt as a catalyst and titania as a support material. Chapter 3 describes the theory and practice of STEM techniques used to undertake this work and Chapter 4 is used to review the development of *in situ* STEM technologies specific to the application of gaseous environments to catalytic materials. Bibliographies will immediately follow each respective chapter.

Chapters 5 and 6 are manuscripts encompassing the results of this research project, written and presented in journal format. An introductory section at the beginning of each chapter will describe the work undertaken and define the involvement of each contributing author. Chapter 5 contains the first paper '*Effect of Manganese on the Activation of Cobalt-based Fischer-Tropsch Catalysts via In Situ Scanning Transmission Electron Microscopy*', demonstrating the reduction of Co/TiO_2 catalysts and investigating the morphological effect induced by Mn inclusion. Chapter 6 contains the second paper '*Determining the Limits of Electron Energy-Loss Spectroscopy Analysis on Heterogeneous Catalysts during In Situ Gas Cell Scanning Transmission Electron Microscopy'*, which describes the various experimental constraints of the gas cell on performing EELS analysis. Sections containing the supplementary information and bibliographies for each of the papers will immediately follow the respective chapter.

Finally, a summary of this research project and potential areas for future work is presented in Chapter 7.

Chapter 2

Fischer-Tropsch Synthesis

2.1. The Fischer-Tropsch Process

2.1.1. Reactions and Products

The chemical synthesis of Fischer-Tropsch (FT) products involves a collection of reactions which convert gaseous mixtures of CO and H_2 (syngas) under high pressure (10's of bars) and elevated temperatures (typically 200-350°C) into a distribution of hydrocarbons with carbon backbone chain lengths from 1 to over 100.[1] The main reactions include:

Alkene production: $n\,CO\,(g) + 2n\,H_2\,(g) \rightarrow C_nH_{2n} + n\,H_2O$ Eq. 2.1

Alkane production: $n\,CO\,(g) + (2n+1)H_2\,(g) \rightarrow C_nH_{2n+2} + n\,H_2O$ Eq. 2.2

Methane production: $CO + 3\,H_2 \rightarrow CH_4 + H_2O$ Eq. 2.3

Syngas feedstocks are ideally produced from natural gas, due to the relatively high hydrogen content, but can also be derived from coal, municipal solid waste or biomass using gasification processes.[2] The FT process consists of adsorption, reaction and desorption steps during flowing of the syngas mix over a catalytically active solid metal surface.[3] The waxy hydrocarbon product can then be hydrocracked to produce clean, high purity diesel and petrol transport fuels.[1] FT synthesis generates large quantities of water, one molecule for each molecule of CO converted, which can lead to sintering of the catalyst material and reduction in catalytically active surface area.[4] Methane (CH_4) is also produced during FT, which is undesirable, hence its selectivity is designed to be minimized when formulating new catalysts.[1]

2.1.2. Active FT Catalysts

Several transition metals display catalytic activity towards FT synthesis, with those which have practical industrial application being based on Fe, Ni, Ru and Co.[5] The choice of catalyst depends on a range of factors, such as the source of syngas feedstock; cost of the active element; and the range of desired end products.[1] Under realistic reaction conditions nickel dissociates CO too readily and, as a result, the increased hydrogenation activity yields a high selectivity towards methane production.[6] The rarity and associated high cost of ruthenium makes it too expensive for large scale application.[6] These constraints lead to iron and cobalt being the most practical active metals for commercial FT synthesis.

Economic sensitivities towards processing conditions also pushes industrial catalysis to occur at as low a temperature as efficiently possible. Both iron and cobalt have been used industrially for low-temperature FT (LTFT, 200-250°C) linear long-chain hydrocarbon synthesis.[7,8] However, due to the increased activity, lifetime (resistance to deactivation) and reduced reaction rate sensitivity to water, cobalt is the FT catalyst of choice for optimal performance.[6]

2.2. Cobalt FT Catalysts

There are a number of considerations when designing cobalt catalysts for FT synthesis, including the type of catalyst support; the deposition method of the catalyst material; the addition of catalyst promoter elements; and any necessary reductive treatments required prior to hydrocarbon synthesis.[6] The design of FT catalysts generally involves the deposition of cobalt onto a particulate oxide support, typically titania, silica or alumina.[3] The geometry of the catalyst/support system can be designed to optimise the amount of deposited catalyst exposed to the gaseous environment in the reactor.[9] Cobalt deposition is most commonly achieved through incipient wetness impregnation, where a cobalt nitrate salt solution is contacted with the oxide support.[10] Initial weak interaction between the precursor and support allows some control over the support surface distribution of cobalt through drying and calcination procedures.[11]

2.2.1. Particle Size/Dispersion Effects

A rational strategy to increase activity in heterogenous systems is to increase the amount of surface on which catalysis can take place. Early studies revealed the specific activity and product selectivity of cobalt catalysts during hydrogenation of CO to be highly dependent on the dispersion, as well as the type of support, metal loading quantity, and method of preparation.[12] Further work demonstrated a significant activity increase as particle size was reduced from 200 to 10 nm.[13–15] Subsequent reports determined the reason for the observed size effects to be due to a lower cobalt reducibility, either as a direct result of the particle size[12] or from the formation of cobalt carbides.[16]

Previous studies typically used oxide supports to establish the influence of cobalt dispersion. However, the formation of less reducible cobalt oxides between the catalyst and support, such as cobalt aluminate[17,18], was observed which added to the complexity of determining any intrinsic particle size effects. An inert carbon nanofibre (CNF) support was subsequently used to investigate the effect of cobalt particle size and distinguish any potential influence from the mixed oxide supports.[19–21] The results revealed a peak activity at 6 nm. However, the surface-specific activity (or turnover frequency, TOF) was shown to be independent of particle size when above 6 nm, with a dramatic drop in activity seen as size is reduced further.[21] A trend was also observed in the methane selectivity, which remained constant until the 6 nm limit, upon which a steep increase was seen.[21] A similar threshold to lower TOF was observed for cobalt particles < 6 nm supported on silica.[22]

The same catalysts were studied using steady-state isotopic transient kinetic analysis (SSITKA) to measure the surface coverage and adsorption, or "residence", time of H, CO and CH_x, OH_x intermediate products.[23] The results showed the properties were independent of cobalt particle sizes when larger than 6 nm, below which an increased residence time (**Figure 2.1a**) and decreased coverage (**Figure 2.1b**) of CH_x explained the lower reported TOF (**Figure 2.1c**).[23] This, in combination with an increased in H coverage, also suggests these effects to be the origin of the observed methane increase in the cobalt particle smaller than 6 nm (**Figure 2.1d**).[23]

2.2.2. Support Effects

The role of a support is to facilitate a high catalyst dispersion, as well as provide mechanical strength and thermal stability during reduction/activation processes. The choice of support is important as it can influence the overall functionality of the catalyst. Due to their extensive characterisation, supports for current industrial application are typically limited to particulate titania, alumina, silica or a mixture of these oxide materials, as opposed to more recently investigated novel materials, such as CNFs.[24] Upon calcination, particulate supports provide a high surface area for catalyst dispersion and highly connected porous network for reactants and products to diffuse through. However, this design also leads to catalysts located at the bottom of a reactor to be more densely packed than those at the top, resulting in a reduced ability for gas flow and a "pressure drop" occurring along the reactor bed.

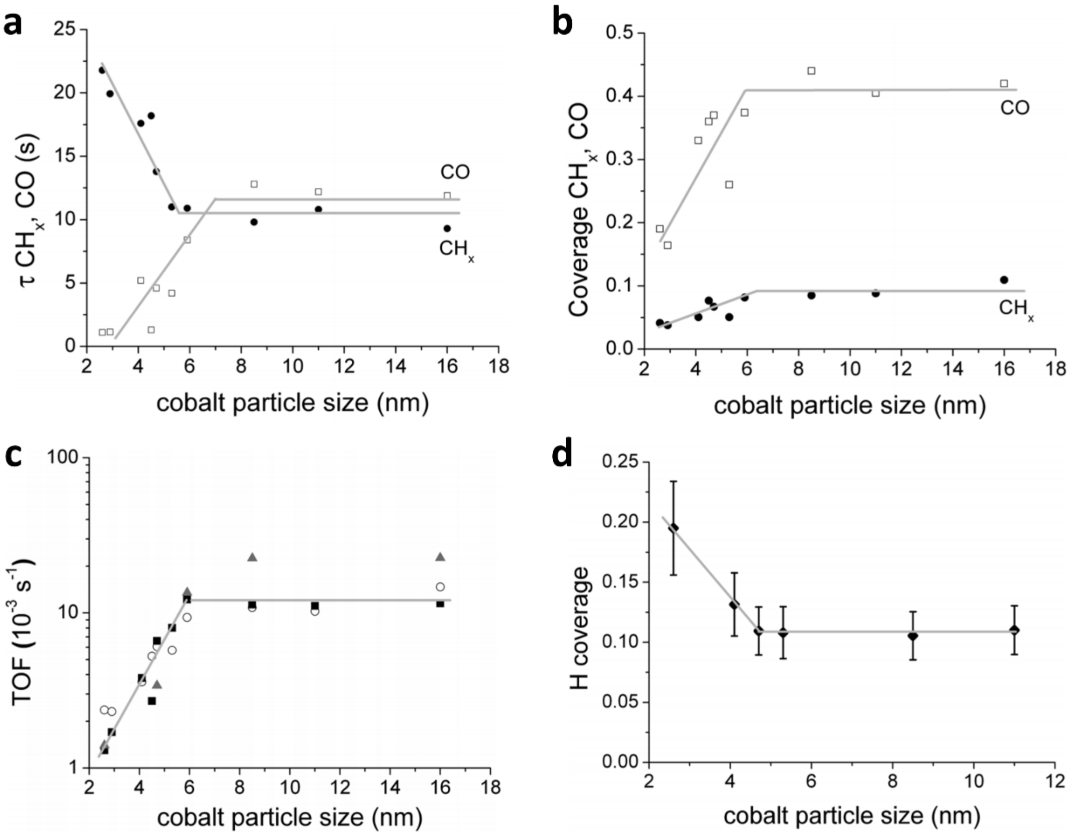

Figure 2.1: Steady-state isotopic transient kinetic analysis (SSITKA) as a function of Co particle size. (a) *Surface residence times and* ***(b)*** *surface coverage of CO and* CH_x *(210°C, 1.85 bar,* $H_2/CO = 10$*).* ***(c)*** *Turnover frequency (TOF) at* $H_2/CO = 2$*: (■) 1 bar, 220°C; (○) 1.85 bar, 210°C; (▲) 35 bar, 210°C.* ***(d)*** *Hydrogen coverage (210°C, 1.85 bar,* $H_2/CO = 10$*). Figure adapted with permission from Breejen et al.*[23] *Copyright 2009 American Chemical Society.*

Cobalt dispersion can vary greatly between titania, alumina and silica supports (Al_2O_3 > TiO_2 > SiO_2) when using the same incipient wetness impregnation technique, with a greater extent of cobalt-support interaction taking place for the supports which stabilised smaller clusters.[25] However, this interaction can lead to the formation of mixed oxides which are difficult to reduce at temperatures typically used industrially (250-300°C), leading to a decreased amount of catalytically active material.[24] This has been reported for Co FT catalysts using titania[26] and alumina[27] supports, where activity is decreased due to the formation of irreducible species, such as $CoTiO_3$. For supports which demonstrate a weak interaction, such as silica, the interaction is diminished, albeit at the cost of cobalt agglomeration during activation and thereby decreasing the catalyst dispersion and the number of active sites.[28]

Another effect, known as the strong metal-support interaction (SMSI), can occur during activation, where reduction of the support surface leads to reduced species migrating onto the catalyst surface.[29] This effect is well documented for Co/TiO_2 FT catalysts and has the potential to significantly decrease activity through blocking of catalytically active sites.[30,31]

2.2.3. Promoter Effects

The term ‘promoter’ refers to elements which are used to improve catalyst functionality, whether that be increased activity, selectivity and/or stability.[1] Promoters are often used to increase the dispersion of a catalyst on the support surface.[32,33] A high dispersion leads to an increased catalyst surface area relative to the loading content, increasing the number of sites that are active towards a particular reaction. For cobalt, the addition of Re[34], Ru[35] and Pt[36], have been shown to increase Co dispersion and subsequently improve catalytic activity. It is worth noting that, by increasing dispersion, the relative amount of catalyst in contact with the support is also increased, which can be detrimental to the activity due to the loss of catalytic material from formation of metal-support compounds.[37]

The presence of promoters can also lead to changes in hydrogen dissociation. This effect is particularly important for cobalt FT catalysts, where an increase in atomic hydrogen may diffuse, or ‘spill over’, and enhance reduction during activation, as previously demonstrated with Re, Ru.[38,39] A variation in the CO/H_2 ratio local to cobalt may also induce an increased susceptibility for the water gas shift reaction to occur, leading to changes in the activity and selectivity.[40,41]

Chemical interaction between the active catalyst and a promoter can modify the local electronic structure, leading to changes in the activity and product selectivity.[42,43] However, if the promoter is present upon the catalyst surface, either due to high loadings or surface diffusion, potential blocking of catalytically active sites can occur.[44]

2.3. Cobalt-Manganese/Titania FT Catalysts

A series of studies on Co-Mn/TiO_2 FT catalysts have provided insights into the changes in product synthesis when using Mn as a promoter.[45–50] Generally, the addition of Mn exhibited the desirable effect of increasing the amount C_{5+} hydrocarbons at the expense of lowering methane (C_1) yield. Of the increase in C_{5+} products, a significant increase in olefinic products was consistently observed, suggested to occur as a result of a lowering in the CO hydrogenation rate during FT synthesis.

The preparation method used to synthesize the Co-Mn/TiO_2 catalysts was demonstrated to play a significant role in the Mn oxidation state and overall dispersion of both catalyst and promoter.[47] Catalysts prepared via incipient wetness impregnation (IWI), where the Co and Mn precursors were impregnated in consecutive steps, which led to a combination of small Co_3O_4 particles and high dispersion of MnO_2 decorating the titania support surface after calcination. Upon reduction in H_2, migration of Mn ions led to the formation of a Ti_2MnO_4 phase, as well as residing on the Co particles, resulting in an activity drop (in comparison to the unpromoted analogue) from the blocking of active sites. In contrast, catalysts prepared via homogeneous deposition precipitation (HDP) led to $Co_{3-x}Mn_xO_4$ solid solution formation, from which the active Co metal phase and MnO remained in close proximity upon the support post-reduction. Comparisons of the HDP catalysts saw an increase in both activity and selectivity when promoted with Mn, highlighting the importance of the Co and Mn positional relationship. Similar results using slight variations on the HDP preparation method have also been reported.[51]

X-ray absorption spectroscopy (XAS)[46,49] and X-ray photoelectron spectroscopy (XPS)[48] has been employed to demonstrate the decrease in Co reducibility as a result of increased Mn addition, effectively leading to less active catalyst post H_2 reduction treatment. While Co_3O_4 in the catalyst specimen containing no Mn was confirmed to reduce to Co metal completely, the promoted catalysts showed mixtures of CoO and Co^0. This can be explained by the increased dispersion of cobalt leading to an increase in the interaction of with the titania support and formation of unreducible species.

In response to the increased activity/selectivity being linked to the close proximity of Co and Mn, and subsequent migration of Mn onto Co during reduction treatments, the strong electrostatic adsorption (SEA) method has been used to minimise the Mn migration effect.[52] The method involved deposition of $[MnO_4]^-$ anions from a $KMnO_4$ precursor onto a HDP prepared TiO_2-supported Co_3O_4 catalyst, with the aim of selectively adsorbing Mn onto the Co rather than the TiO_2 and subsequently increase the Co/Mn interaction. The results showed increased C_{5+} selectivity and decreased methane selectivity as Mn loadings increased, however an opposing trend in decreasing activity with increasing Mn was also observed, likely as a result of Mn blocking active sites on the Co metal surface.

More recently a series of IWI-prepared Co-Mn/TiO_2 FT catalysts have been reported which used a mixed precursor solution to co-impregnate the catalyst and promoter onto the support (10 wt% Co promoted with 0-10 wt% Mn).[53] These catalysts varied from those previously studied by Morales *et al*, where Co and Mn were impregnated consecutively. XRD and STEM-EDS observations revealed a similar mixed $Co_{3-x}Mn_xO_4$ solid solution to be highly dispersed on the support post-calcination. After reduction in hydrogen, the Co and Mn were observed to segregate, with increasing Mn inclusion leading to the formation of decreasing Co particle sizes. Catalyst testing was performed to establish the selectivity towards conventional C_{5+} products, which revealed to be highest in the 1.5 wt% Mn catalyst. To establish the importance of the close proximity relationship between Co and Mn, physical mixture experiments were performed between Co-only and Mn-only impregnated supports. The catalytic activity and selectivity were both analogous to that of the Co-only specimen, highlighting the importance of the catalyst/promoter interaction during FT synthesis.

Bibliography

1. Morales, F. & Weckhuysen, B. M. *Promotion Effects in Co-based Fischer–Tropsch Catalysis*. vol. 19 (Catalysis, 2006).
2. Ertl, G., Knözinger, H. & Weitkamp, J. *Handbook of Heterogeneous Catalysis*. vol. 2 (Wiley VCH, 1997).
3. Bowker, M. *The Basis and Applications of Heterogeneous Catalysis*. (Oxford University Press, 1998).
4. Paterson, J., Peacock, M., Ferguson, E., Ojeda, M. & Clarkson, J. In situ X-ray diffraction of Fischer-Tropsch catalysts - Effect of water on the reduction of cobalt oxides. *Appl. Catal. A Gen.* **546**, 103–110 (2017).
5. Vannice, M. A. The Catalytic Synthesis of Hydrocarbons from H2/CO Mixtures over the Group VIII Metals. *J. Catal.* **37**, 449–461 (1975).
6. Khodakov, A. Y., Chu, W. & Fongarland, P. Advances in the development of novel cobalt Fischer-Tropsch catalysts for synthesis of long-chain hydrocarbons and clean fuels. *Chem. Rev.* **107**, 1692–1744 (2007).
7. Jager, B. & Espinoza, R. Advances in low temperature Fischer-Tropsch synthesis. *Catal. Today* **23**, 17–28 (1995).
8. Espinoza, R. L., Steynberg, A. P., Jager, B. & Vosloo, A. C. Low temperature Fischer-Tropsch synthesis from a Sasol perspective. *Appl. Catal. A Gen.* **186**, 13–26 (1999).
9. Devyatkov, S., Kuzichkin, N. V. & Murzin, D. Y. On comprehensive understanding of catalyst shaping by extrusion. *Chim. Oggi/Chemistry Today* **33**, 57–64 (2015).
10. Lee, S. Y. & Aris, R. The distribution of active ingredients in supported catalysts prepared by impregnation. *Catal. Rev. Sci. Eng.* **27**, 207–340 (1985).
11. Schwarz, J. A., Contescu, C. & Contescu, A. Methods for Preparation of Catalytic Materials. *Chem. Rev.* **95**, 477–510 (1995).

12. Reuel, R. C. & Bartholomew, C. H. Effects of support and dispersion on the CO hydrogenation activity/selectivity properties of cobalt. *J. Catal.* **85**, 78–88 (1984).

13. Iglesia, E., Soled, S. L. & Fiato, R. A. Fischer-Tropsch synthesis on cobalt and ruthenium. Metal dispersion and support effects on reaction rate and selectivity. *J. Catal.* **137**, 212–224 (1992).

14. Iglesia, E., Soled, S. L., Fiato, R. A. & Via, G. H. Dispersion, support, and bimetallic effects in Fischer-Tropsch synthesis on cobalt catalysts. in *Natural Gas Conversion II* (eds. Curry-Hyde, H. E. & Howe, R. F. B. T.-S. in S. S. and C.) vol. 81 433–442 (Elsevier, 1994).

15. Iglesia, E. Design, synthesis, and use of cobalt-based Fischer-Tropsch synthesis catalysts. *Appl. Catal. A Gen.* **161**, 59–78 (1997).

16. Johnson, B. G., Bartholomew, C. H. & Goodman, D. W. The role of surface structure and dispersion in CO hydrogenation on cobalt. *J. Catal.* **128**, 231–247 (1991).

17. van Berge, P. J., van de Loosdrecht, J., Barradas, S. & van der Kraan, A. M. Oxidation of cobalt based Fischer–Tropsch catalysts as a deactivation mechanism. *Catal. Today* **58**, 321–334 (2000).

18. Jacobs, G. *et al.* Fischer–Tropsch synthesis: deactivation of noble metal-promoted Co/Al2O3 catalysts. *Appl. Catal. A Gen.* **233**, 215–226 (2002).

19. Bezemer, G. L., Van Laak, A., Van Dillen, A. J. & De Jong, K. P. Cobalt supported on carbon nanofibers - A promising novel Fischer-Tropsch catalyst. *Stud. Surf. Sci. Catal.* **147**, 259–264 (2004).

20. Bezemer, G. L. *et al.* Preparation of Fischer-Tropsch cobalt catalysts supported on carbon nanofibers and silica using homogeneous deposition-precipitation. *J. Catal.* **237**, 291–302 (2006).

21. Bezemer, G. L. *et al.* Cobalt particle size effects in the Fischer-Tropsch reaction studied

with carbon nanofiber supported catalysts. *J. Am. Chem. Soc.* **128**, 3956–3964 (2006).

22. Barbier, A., Tuel, A., Arcon, I., Kodre, A. & Martin, G. A. Characterization and Catalytic Behavior of Co/SiO2 Catalysts: Influence of Dispersion in the Fischer–Tropsch Reaction. *J. Catal.* **200**, 106–116 (2001).
23. den Breejen, J. P. *et al.* On the Origin of the Cobalt Particle Size Effects in Fischer−Tropsch Catalysis. *J. Am. Chem. Soc.* **131**, 7197–7203 (2009).
24. Rytter, E. & Holmen, A. On the support in cobalt Fischer–Tropsch synthesis - Emphasis on alumina and aluminates. *Catal. Today* **275**, 11–19 (2016).
25. Jacobs, G. *et al.* Fischer–Tropsch synthesis: support, loading, and promoter effects on the reducibility of cobalt catalysts. *Appl. Catal. A Gen.* **233**, 263–281 (2002).
26. Kliewer, C. E., Soled, S. L. & Kiss, G. Morphological transformations during Fischer-Tropsch synthesis on a titania-supported cobalt catalyst. *Catal. Today* **323**, 233–256 (2019).
27. Bessell, S. Support effects in cobalt-based Fischer-Tropsch catalysis. *Appl. Catal. A Gen.* **96**, 253–268 (1993).
28. Kababji, A. H., Joseph, B. & Wolan, J. T. Silica-Supported Cobalt Catalysts for Fischer–Tropsch Synthesis: Effects of Calcination Temperature and Support Surface Area on Cobalt Silicate Formation. *Catal. Letters* **130**, 72–78 (2009).
29. Tauster, S. J. Strong metal-support interactions. *Acc. Chem. Res.* **20**, 389–394 (1987).
30. Wolf, M. *et al.* Water-Induced Formation of Cobalt-Support Compounds under Simulated High Conversion Fischer–Tropsch Environment. *ACS Catal.* **9**, 4902–4918 (2019).
31. Qiu, C. *et al.* Direct observation of the evolving metal–support interaction of individual cobalt nanoparticles at the titania and silica interface. *Chem. Sci.* **11**, 13060–13070 (2020).

32. Girardon, J.-S. *et al.* Cobalt dispersion, reducibility, and surface sites in promoted silica-supported Fischer–Tropsch catalysts. *J. Catal.* **248**, 143–157 (2007).

33. Zeng, S., Du, Y., Su, H. & Zhang, Y. Promotion effect of single or mixed rare earths on cobalt-based catalysts for Fischer–Tropsch synthesis. *Catal. Commun.* **13**, 6–9 (2011).

34. Vada, S., Hoff, A., ÅdnaneS, E., Schanke, D. & Holmen, A. Fischer-Tropsch synthesis on supported cobalt catalysts promoted by platinum and rhenium. *Top. Catal.* **2**, 155–162 (1995).

35. Iglesia, E. Fischer-Tropsch synthesis on cobalt catalysts: Structural requirements and reaction pathways. in *Natural Gas Conversion IV* (eds. de Pontes, M., Espinoza, R. L., Nicolaides, C. P., Scholtz, J. H. & Scurrell, M. S. B. T.-S. in S. S. and C.) vol. 107 153–162 (Elsevier, 1997).

36. Zsoldos, Z., Hoffer, T. & Guczi, L. Structure and catalytic activity of alumina-supported platinum-cobalt bimetallic catalysts. 1. Characterization by X-ray photoelectron spectroscopy. *J. Phys. Chem.* **95**, 798–801 (1991).

37. Wolf, M. *et al.* Synthesis, characterisation and water–gas shift activity of nano-particulate mixed-metal (Al, Ti) cobalt oxides. *Dalt. Trans.* **48**, 13858–13868 (2019).

38. Jacobs, G., Chaney, J. A., Patterson, P. M., Das, T. K. & Davis, B. H. Fischer–Tropsch synthesis: study of the promotion of Re on the reduction property of Co/Al2O3 catalysts by in situ EXAFS/XANES of Co K and Re LIII edges and XPS. *Appl. Catal. A Gen.* **264**, 203–212 (2004).

39. Bruce, L. A., Hoang, M., Hughes, A. E. & Turney, T. W. Ruthenium promotion of Fischer-Tropsch synthesis over coprecipitated cobalt/ceria catalysts. *Appl. Catal. A Gen.* **100**, 51–67 (1993).

40. Keyser, M. J., Everson, R. C. & Espinoza, R. L. Fischer–Tropsch studies with cobalt–manganese oxide catalysts: Synthesis performance in a fixed bed reactor. *Appl. Catal.*

A Gen. **171**, 99–107 (1998).

41. Keyser, M. J., Everson, R. C. & Espinoza, R. L. Fischer−Tropsch Kinetic Studies with Cobalt−Manganese Oxide Catalysts. *Ind. Eng. Chem. Res.* **39**, 48–54 (2000).

42. Li, Z. *et al.* Effects of alkali metal promoters on the structure–performance relationship of CoMn catalysts for Fischer–Tropsch synthesis. *Catal. Sci. Technol.* **10**, 1816–1826 (2020).

43. Gupta, S. S., Shenai, P. M., Meeuwissen, J., Bezemer, G. L. & Shetty, S. Electronic Promotion Effects of Metal Oxides: A Case Study of MnO Impact on Fischer–Tropsch Catalysis. *J. Phys. Chem. C* **125**, 21390–21401 (2021).

44. Jacobs, G. *et al.* Group 11 (Cu, Ag, Au) promotion of 15%Co/Al2O3 Fischer–Tropsch synthesis catalysts. *Appl. Catal. A Gen.* **361**, 137–151 (2009).

45. Morales Cano, F., Gijzeman, O. L. J., de Groot, F. M. F. & Weckhuysen, B. M. Manganese promotion in cobalt-based Fischer-Tropsch catalysis. in *Natural Gas Conversion VII* (eds. Bao, X. & Xu, Y. B. T.-S. in S. S. and C.) vol. 147 271–276 (Elsevier, 2004).

46. Morales, F. *et al.* In Situ X-ray Absorption of Co/Mn/TiO2 Catalysts for Fischer−Tropsch Synthesis. *J. Phys. Chem. B* **108**, 16201–16207 (2004).

47. Morales, F., Grandjean, D., De Groot, F. M. F., Stephan, O. & Weckhuysen, B. M. Combined EXAFS and STEM-EELS study of the electronic state and location of Mn as promoter in Co-based Fischer-Tropsch catalysts. *Phys. Chem. Chem. Phys.* **7**, 568–572 (2005).

48. Morales, F. *et al.* Mn promotion effects in Co/TiO2 Fischer-Tropsch catalysts as investigated by XPS and STEM-EELS. *J. Catal.* **230**, 301–308 (2005).

49. Morales, F., Grandjean, D., Mens, A., De Groot, F. M. F. & Weckhuysen, B. M. X-ray absorption spectroscopy of Mn/Co/TiO2 Fischer-Tropsch catalysts: Relationships

between preparation method, molecular structure, and catalyst performance. *J. Phys. Chem. B* **110**, 8626–8639 (2006).

50. Morales, F., de Smit, E., de Groot, F. M. F., Visser, T. & Weckhuysen, B. M. Effects of manganese oxide promoter on the CO and H2 adsorption properties of titania-supported cobalt Fischer-Tropsch catalysts. *J. Catal.* **246**, 91–99 (2007).

51. Grandjean, D., Morales, F., Mens, A., De Groot, F. M. F. & Weckhuysen, B. M. Unraveling the structure of Mn-promoted Co/TiO2 Fischer-Tropsch catalysts by in situ X-ray absorption spectroscopy. *AIP Conf. Proc.* **882**, 666–668 (2007).

52. Feltes, T. E. *et al.* Selective adsorption of manganese onto cobalt for optimized Mn/Co/TiO2 Fischer-Tropsch catalysts. *J. Catal.* **270**, 95–102 (2010).

53. Paterson, J. *et al.* Manipulation of Fischer-Tropsch Synthesis for Production of Higher Alcohols Using Manganese Promoters. *ChemCatChem* **10**, 5154–5163 (2018).

Chapter 3

Transmission Electron Microscopy

In 1879 Lord Rayleigh proposed that the minimal resolvable distance (δ) between two points is proportional to the wavelength (λ) of the illumination radiation:

$$\delta = \frac{0.61\lambda}{\mu \sin \beta} \qquad \text{Eq. 3.1}$$

where (μ) is the refractive index of the viewing medium and (β) is the collection semi-angle of a magnifying lens.[1] The terms ($\mu \sin \beta$) are also commonly referred to as the numerical aperture of the lens. The shortest wavelength of visible light (violet) is in the ~380 nm region, which limits the ultimate resolution of optical microscopy to ≈200 nm. This scale is appropriate for studying certain regimes of a material's morphology (e.g., grains/boundaries in metals) or some biological specimens (e.g., cells and bacteria) but is inadequate for yielding information at the atomic scale.

In 1924 Louis de Broglie showed that the wavelength of the electron is inversely proportional to its energy (E):[2]

$$\lambda = \frac{1.22}{E^{1/2}} \qquad \text{Eq. 3.2}$$

These findings led Knoll and Ruska to pioneer the first transmission electron microscope (TEM) in 1932, which has since been developed as a versatile characterization tool for a wide variety of materials.[3] The primary feature of this microscope is the ability to provide a range of high spatial resolution imaging and complementary analytical techniques. By using suitably high-energy electrons (100 – 300 keV) as the illumination source, wavelengths on the order of 1 pm can provide the resolution required for atomic-scale imaging.

TEM is generally split into two techniques: conventional TEM (CTEM) and scanning TEM (STEM). In both, electrons are typically extracted from either a thermionic (LaB_6 crystal) or field-emission (fine tungsten needle) source, in an assembly generally referred to as the electron ‘gun’. Field-emission guns are preferred for the highest resolutions as they yield a greater brightness and a more monochromic beam of electrons (i.e., the emitted electrons have smaller distribution of energies).[4] However, the ability to perform atomically resolved imaging is only one aspect of the TEM. The range of different signals that can be generated and detected from the various electron/specimen interactions are what makes TEM such a powerful instrument. This chapter will discuss the interactions relevant to this project and detail how they are used in their corresponding imaging and analysis modes.

3.1. Electron-Matter Interactions

Electron interactions with matter can lead to a variety of signals being generated.[5] In the TEM these signals are detected and used to yield information on various characteristics of the specimen. With this in mind, a basic understanding of these interactions is essential to be able to correctly interpret the data acquired during TEM imaging and analysis.

The strong interaction of electrons with matter leads to a short mean free path when passing through a specimen.[6] As a result, the ability to transmit an appreciable number of electrons requires the specimen to be thin (<100 nm).[7] Transmitted electrons which have undergone interaction can be grouped into two categories: elastic scattering, in which the energy loss from this process is negligible relative to the illuminating electron beam energy, or inelastic scattering, in which an substantial amount of energy from the electron is transferred.[8] These processes will be described in more detail below.

3.1.1. Elastic Scattering

Elastic scattering arises from the incident electron interacting with the electrostatic potential distribution generated between the positively charged nucleus and negatively charged electron cloud. Electron-nucleus interaction can lead to high-angle scattering (up to 180°), whereas electron-electron interactions are generally scattered to low-angles. When considering the incident electron as a particle, the probability of elastic scattering can be expressed by an interaction cross section ($d\sigma/d\Omega$):

$$\frac{d\sigma}{d\Omega} = \frac{4\gamma^2 Z^2}{a_0^2 q^2} \qquad \text{Eq. 3.3}$$

where (γ) is a relativistic factor, which is dependent on the incident electron velocity, (Z) is the atomic number, (a_0) is the Bohr radius and (q) is the magnitude of the momentum transfer scattering vector.[9] This equation reveals the elastic scattering potential (and in turn the signal intensity) to be proportional to Z^2. However, it does not take into account screening effects of the nuclear potential from atomic electrons, which acts to reduce the relation to a $Z^{1.5\text{-}2}$ dependency.[10]

The electron particle description of scattering is useful when considering the interaction of single electrons with isolated atoms. However, electrons exhibit a wave-particle duality. When considering the electron beam as a wave and specimen atoms as scattering points, electron beam interaction may lead to coherent and/or incoherent scattering. In a crystal lattice, scattering from the periodic atomic structure will lead to constructive and deconstructive interference.

Considering the electron beam as a plane wave of unity amplitude transmitting a sufficiently thin specimen (as to only induce a small phase shift, i.e., a weak phase object) the resulting coherent intensity (I_{coh}) is given by:

$$I_{coh}(\mathbf{R}) = |\Psi(\mathbf{R}) \otimes P(\mathbf{R})|^2 \qquad \text{Eq. 3.4}$$

where ($\mathbf{R}$) is the point in the specimen from which (Ψ) is the exit wave, and $P(\mathbf{R})$ is the point spread function.[11] With respect to the TEM, coherent scattering is the basis of phase contrast and diffraction contrast, which both contribute to bright-field and dark-field imaging in both conventional TEM and scanning TEM (discussed in more detail in chapter 3.2).[12] Conversely, non-crystalline specimens will lead to incoherent scattering from an electron plane wave, from which intensity (I_{incoh}) is given as:

$$I_{incoh}(\mathbf{R}) = |P(\mathbf{R})|^2 \otimes |\Psi(\mathbf{R})|^2 \qquad \text{Eq. 3.5}$$

Incoherent scattering provides contrast contribution from mass-thickness (i.e. the increased scattering proportional to denser/thicker areas of a specimen) and is the basis for high-angle annular dark-field STEM imaging (discussed in more detail in chapter 3.3).[13]

3.1.2. Inelastic Scattering

As previously mentioned, inelastic scattering leads to a considerable energy loss of the incident electron. The energy is transferred to the sample, which will undergo an excitation and subsequent relaxation process to dissipate the energy and return to a ground level energy state. This interaction can lead to the generation of phonons, plasmons and X-rays, all of which can be used to gain further insight into the properties of a specimen.[12] As the work in this project does not concern phonon or plasmon analysis, a description of these processes will not be provided here. In contrast, the generation of X-rays through atomic ionisation is used extensively in the following studies and as such a detailed description of this process is provided in chapter 3.4.

3.2. Conventional Transmission Electron Microscopy

In conventional TEM (CTEM) a thin specimen is illuminated with a parallel beam of electrons. This is achieved via the condenser lens system (C1, C2) and the upper objective lens. Electrons incident to the specimen can be scattered or pass through unimpeded, in either case contributing to the formation of a diffraction pattern (DP) in the back focal plane (BFP) and recombining to form an image in the image plane. An intermediate lens can be used to project either the BFP or image, where subsequent projection lenses then magnify the selected plane (i.e., DP or image) onto a phosphor screen for viewing or onto a charge coupled device (CCD) or direct electron detector for digital capture.

3.2.1. Selected Area Electron Diffraction

For the thin specimens required to perform TEM, the probability of interaction between the transmitted electrons and the constituting periodic crystal structure is low. This leads to DPs that have a highly intense central spot and much less intense surrounding spots, with distances from the centre depending on the interatomic spacing. A DP contains diffraction spots from the entire region under illumination from the electron beam. This can lead to a blurring of the spots from specimen buckling and the inclusion of spots from undesirable areas. Selected area electron diffraction (SAED) involves placing an aperture in the image plane of the specimen (conjugate to the object plane) to select a specific region of interest from which the electrons contribute to the DP. This technique can improve the quality of the DP, provide more localised information, and can help prevent damage to the CCD from the high intensity of the direct beam.

3.2.2. Bright-field and Dark-field TEM Imaging

In addition to the SAED description above, an objective aperture can be inserted into the BFP and centered around either the directly transmitted central beam or one of the diffraction spots to yield a bright field (BF) or dark field (DF) image, respectively. In BF imaging only electrons which are either not scattered, or scattered to a sufficiently low angle, are selected to contribute to the image formation. The resulting image shows contrast in which dark regions appear in areas that have highly scattered the beam. Conversely, the selection of a diffraction spot in DF imaging generates contrast in which increased brightness is given by areas of the sample that satisfy the chosen diffraction spot conditions. This method of imaging is useful for mapping a particular crystal orientation in a sample.[14]

3.2.3. High-resolution TEM Imaging

High-resolution (HR) TEM is a phase contrast technique which provides the ability to image the atomic structure of a specimen.[15] This is achieved using a phase-contrast transfer function (PCTF) to describe the behaviour of the electron wavefunction exiting the sample, interacting with the imaging system and subsequently hitting the detector. The PCTF is dependent on defocus and objective lens aberrations, which can be described by:

$$\sin \chi\,(\mathbf{u}) \qquad \text{Eq. 3.6}$$

where ($\mathbf{u}$) is the spatial frequency (relating to the interatomic distances) and ($\chi(\mathbf{u})$) is the phase-distortion function, which contains the effects of spherical aberration and other geometric aberrations.[12] Since $\sin \chi\,(\mathbf{u})$ is an oscillating function, care is required when performing HRTEM analysis as artefacts and inversions of contrast can be introduced as a result of altering the imaging conditions.[16]

3.2.4. Aberration Correction

By considering the TEM electron beam emitted from the gun as a plane wave, interaction with the magnetic field from an ideal lens would focus it to an infinitely sharp point (**Figure 3.1a**). However, this is not an accurate representation of TEM as electron emission is not perfectly monochromatic and lenses contain imperfections, known as aberrations.[17] Both lead to electrons being deviated slightly in their ideal trajectory. There are two main forms of aberrations of concern in TEM: spherical and chromatic.[18]

Spherical aberrations occur due to the varying magnetic field strength of the lens. **Figure 3.1b** illustrates how rays can be more strongly focused the further they are away from the optic axis. As a result, electrons which pass through closer to the lens centre are focused to a point at a greater distance along the optic axis relative to those that pass through the outer regions of the lens. The semi angle (α) at which spherical aberrations yields the minimum probe size is known as the disc of least confusion (d_s), given by:

$$d_s = \frac{1}{2} C_s \alpha^3 \qquad \text{Eq. 3.7}$$

where (C_s) is the spherical aberration coefficient.[5] Advancements in spherical aberration correction have been achieved using additional, non-spherical electron lenses.[19] The effect is essentially an elimination of 3rd order spherical aberration, which allows a much smaller beam probe to be attained. Further improvements can be made through the reduction in other low order geometric aberrations, 5th order spherical aberrations or chromatic aberrations.[20]

Chromatic aberration describes the energy spread of electrons originating from the source (gun). The small electron energy differences lead to a varying degree of focus by the lens (**Figure 3.1c**). Much like spherical aberration, this produces a focus distance range along the optic axis and effectively increases the probe diameter. In this case, the disc of least confusion (d_c) is given by:

$$d_c = \frac{C_c \alpha \Delta E}{E_0} \qquad \text{Eq. 3.8}$$

where (C_c) is the chromatic aberration coefficient, (ΔE) is the spread of electron energies, and (E_0) is the energy of the incident electron beam.[5] Improvements in chromatic aberration effects can be made through the use of monochromators, in which a reduced energy spread can be achieved through spreading the beam (in turn spreading the energy distribution) and using aperture-like ‘slits’ to restrict the beam to a narrow energy range.[21]

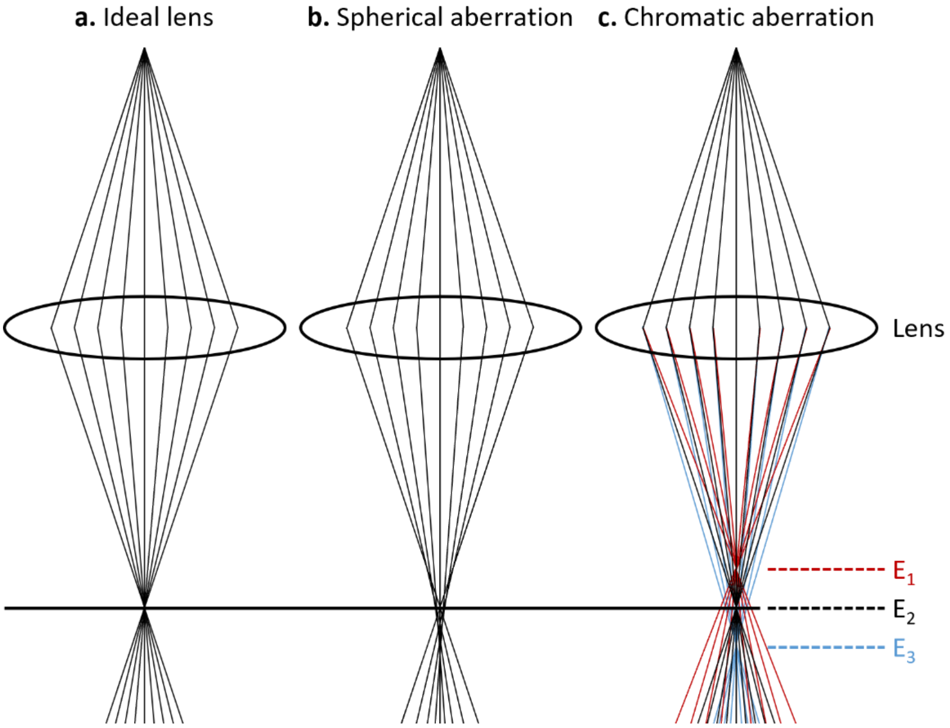

Figure 3.1: Schematic illustration of aberration effects on the electron beam. (a) *An ideal lens with no aberrations would lead to the electron beam converging to a sharp probe.* ***(b)*** *Spherical aberration arising from changes in strength of the lens.* ***(c)*** *Chromatic aberration arising from the range of energies (E) in the emitted electrons (lower energy electron are focused more strongly). Both aberration effects result in a focus range along the optic axis, leading to an increased probe size and subsequent blurring of images.*

3.3. Scanning Transmission Electron Microscopy

In contrast to the broad beam of electrons used in CTEM, scanning TEM (STEM) instead utilizes the condenser lens system to focus the electron beam to a small probe, which is then rastered across the specimen (**Figure 3.2**). Once a region of interest (ROI) has been identified the desired resolution of the image can be chosen. This is achieved by dividing the area into the chosen number of pixels, which subsequently determines the beam positions at which the probe will occupy for a predetermined dwell time. Any signals collected at this position are then recorded and stored at the corresponding pixel position in the digital image. The choice of dwell time (typically on the order of μs) and resolution is important in controlling the electron fluence (the number of electrons/area) transmitting the specimen ROI. Ideally the fluence chosen is great enough so that a necessary amount of signal can be collected by the various detectors, but not so much that damage to the specimen from the beam starts to occur.[22]

In this section the various forms of lens aberrations will be discussed. A description of the most common STEM imaging techniques, bright-field (BF) and high-angle annular dark-field (HAADF), will also be provided.

3.3.1. Bright-field STEM Imaging

BF-STEM imaging uses an electron detector mounted on the optic axis to collect the unscattered and low angle scattered electrons which have interacted with the specimen. The contrast mechanisms for BF-CTEM and BF-STEM are the same, with the major contribution to image contrast arising from phase contrast as well as minor contributions from mass-thickness and diffraction contrast. BF-STEM is highly sensitive to the electron probe defocus, aberrations, and thickness of the specimen.[16] Analysing BF-STEM images requires a detailed knowledge of the contrast mechanisms and microscope parameters, also requiring image simulation to correctly interpret the results quantitatively.[23]

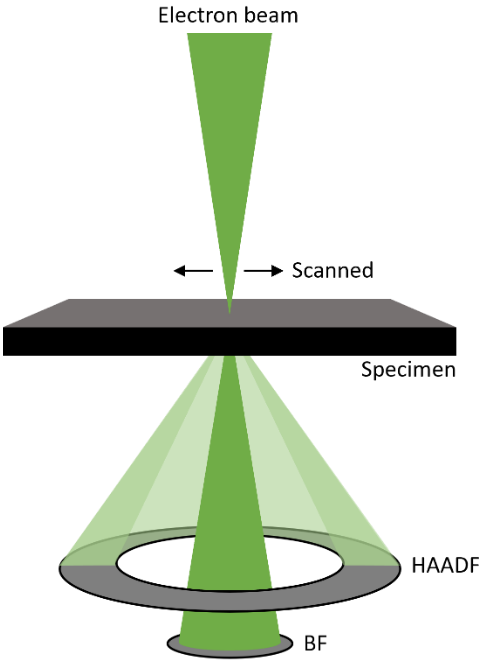

Figure 3.2: Illustration of the beam/specimen interaction and detector geometry in STEM. *The bright-field (BF) detector is located on the optic axis conjugate to the back focal plane (BFP). The high-angle annular dark-field (HAADF) detector collects an angular range of diffracted electrons. This design allows both signals to be collected simultaneously.*

3.3.2. High-angle Annular Dark-field STEM Imaging

High-angle annular dark-field (HAADF) STEM imaging utilizes an annular detector to selectively collect the electrons which have been incoherently scattered to large angles. This detector design allows the unscattered beam to pass directly to the central BF detector, allowing simultaneous collection of both signals during imaging (**Figure 3.2**).

The HAADF signal intensity can be approximated using the most basic form of the Rutherford scattering cross section (**Eq. 3.3**, not accounting for relativistic or screening effects) or more accurately by considering the electron wave properties (**Eq. 3.5**). By configuring the microscope to exclude any possible contribution from diffraction spots, the intensity (I) can be expressed as being proportional to the mean square displacement (σ) of the atom and the atomic number (Z), given by:[24]

$$I \propto \sigma^2 Z^2 \qquad \text{Eq. 3.9}$$

As such, the HAADF signal intensity is largely dependent on mass-thickness and is generally referred to as a method of Z-contrast imaging.[25,26] These methods complement the ability to characterise chemical properties from analytical methods, such as energy-dispersive X-ray spectroscopy and electron energy-loss spectroscopy, both of which will be further detailed in sections 3.4 and 3.5, respectively.

3.4. Energy Dispersive X-ray Spectroscopy

Energy dispersive X-ray spectroscopy involves the collection of X-rays generated as a result of the interaction between the incident electron beam and a specimen. Several acronyms exist for this technique, including EDS, EDX and EDXS. In this project the abbreviation EDS will be used throughout for consistency.

EDS can be used in combination with both CTEM and STEM imaging to provide chemical information in the form of an energy spectrum. In CTEM, the spectrum collected is from the entire ROI illuminated by the electron beam. When used with STEM imaging, an individual spectrum can be collected at each probe position, allowing a high spatial resolution elemental map of a specimen to be generated and the ability to quantify the concentration of each element present.[27] This is particularly valuable when investigating systems in which the elemental distribution has direct consequences on the functionality of a material, for example, the activity, selectivity and stability of catalyst systems.[28]

3.4.1. X-ray Emission

During interaction with the specimen, an incident electron can generate an X-ray from one of two different processes. The resulting X-rays are classified as ‘Characteristic’ or ‘Bremsstrahlung’ (German for ‘braking radiation’).

As described in section 3.1.2, incident electrons can be inelastically scattered when transmitting the electron cloud of a specimen. This process is illustrated in **Figure 3.3a**. If the incoming electrons have a sufficiently high voltage it can lead to an inner shell electron being ejected from the atom. The energy required to eject the electron from a core shell is known as the critical ionisation energy. The resulting ionised atom then returns to its ground state by filling the hole with an electron from one of the outer shells. This transition requires a release of energy, either in the form of an X-ray or Auger electron, the energy of which is characteristic of the element and shells involved. The probability of an inelastic interaction leading to characteristic X-ray emission is known as the fluorescence yield (ω), which scales with atomic

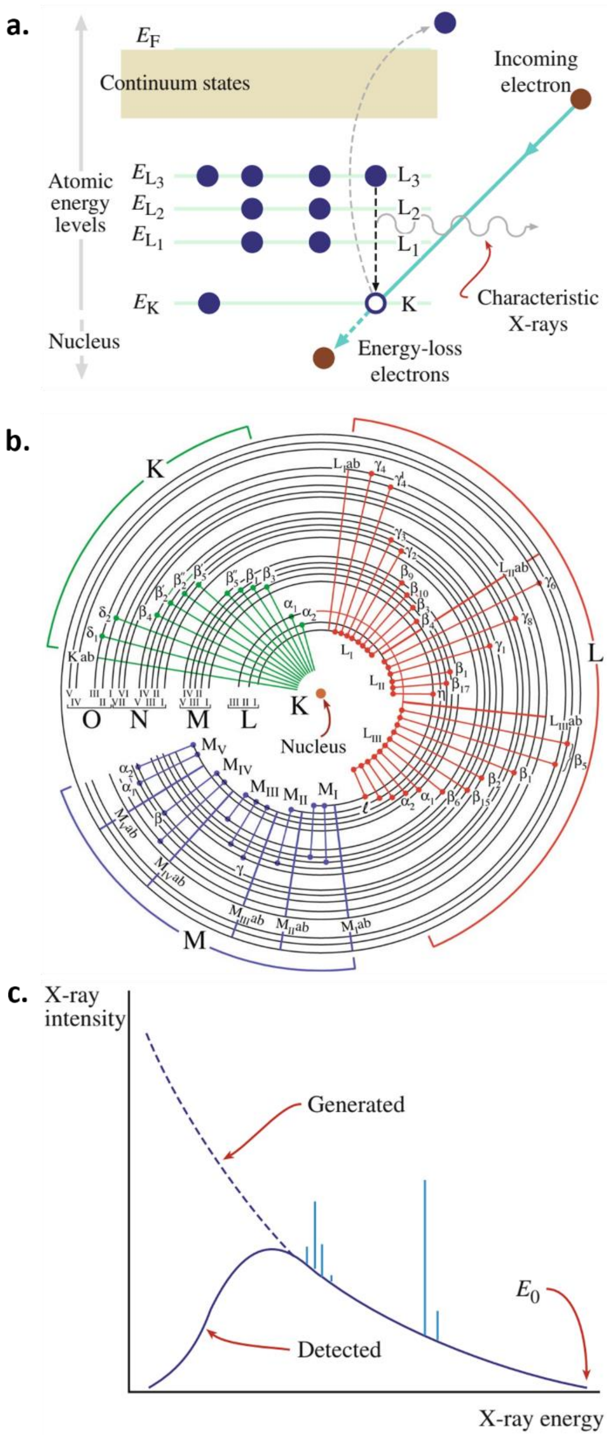

Figure 3.3: Overview of energy dispersive X-ray spectroscopy processes. (a) *Illustration of the ionization process.* ***(b)*** *The entire range of potential transitions between electron shells that lead to the generation of K, L, and M characteristic X-rays.* ***(c)*** *Simplified spectra demonstrating the superposition of characteristic X-ray peaks (lines) and the Bremsstrahlung background as a function of energy. Figure adapted with permission from Williams and Carter (2009).*[12]

number (Z).[29] All possible K, L and M shell transitions which can lead to characteristic X-ray generation can be observed in **Figure 3.3b** and allow the identification of chemical composition.

X-rays can also be generated by incident electrons which undergo a momentum change during interaction with the Coulomb field of the atomic nucleus. These bremsstrahlung X-rays have an energy dependent on the amount of electron deceleration caused. The result is a continuous background of X-ray energy ranges in the spectrum on which the characteristic peaks are superimposed (**Figure 3.3c**).

3.4.2. X-ray Detection

X-ray emission is isotropic, generated in a sphere with a solid angle of 4π steradian (srad), and is measured using a detector placed in close proximity to the specimen. Ideally, a detector would collect all the X-rays emitted from the electron beam/specimen interaction point source. However, the space in which a detector can be positioned in the TEM is constrained by the upper and lower pole pieces. As the extent of signal collection is dependent on the total collection solid angle, current advanced designs make use of multiple detectors to increase the solid angle up to ~0.9 srad.[30] As the generation occurs over a sphere of 4π srad this corresponds to the collection of ~7.2% of the entire X-ray emission.

Characteristic peaks in the spectra may also arise from sources other than the specimen. These can include the specimen grid (usually Cu or Au with a C film), the microscope pole-piece (typically Fe or Co) and the detector itself (potentially Zr, Si or Pb).[31] In situ observation also brings the possibility of spurious counts from the micro electromechanical systems (MEMS) based environmental cells (Si, C, N) or holders (Ti) required.[32] Signals from these sources can lead to complicated analysis if they overlap with peaks from the specimen.

3.4.3. Quantitative EDS

As previously mentioned, quantification of EDS provides the ability to identify the elemental composition of a specimen. Additionally, when used in combination with scanning imaging modes, STEM-EDS allows the composition distribution to be spatially mapped. In more precise instruments quantitative EDS can reach close to atomic resolution.[33] The two most common routes to perform quantitative EDS are the k-factor[34] and ζ (zeta) factor[35] methods. Both techniques first require 'background' subtraction before calculation of the X-ray peak intensities, as discussed below.

Background subtraction

As the characteristic X-ray peaks are superimposed with the bremsstrahlung background intensity, this must first be subtracted before calculation of the peak intensities. There are two common ways to perform the subtraction: using an energy 'windows' method or model-fitting.

The windows method involves defining the energy value at both edges of the characteristic peak. An average of these values is then used to subtract the integrated background signal within the windowed region. This simple method is appropriate when the background is relatively uniform (i.e., at higher energies) and when there is no peak overlap. Alternatively, the spectrum can be modelled. Background subtraction can be performed using Kramers' law[36], although a basic power law is adequate in most cases. Modified Gaussian peaks can then be fitted to the peaks and the intensities subsequently calculated. This method is particularly useful when analysing spectra with low signal-to-noise ratio (SNR) or with overlapping characteristic peaks.

Peak intensity

EDS detectors allow the direct measurement of the individual X-ray energies and subsequent computational analysis can determine the peak intensity (I_A).[10] This value is dependent on the number of incident electrons (D_e), the ionisation probability ($n_A t Q_A$), the fluorescence yield (ω_A), the relative transition probability (a_A) and the overall detection efficiency ($(\Omega/4\pi)\varepsilon_A$):

$$I_A = D_e \cdot n_A t Q_A \cdot \omega_A \cdot a_A \cdot \left(\frac{\Omega}{4\pi}\right) \varepsilon_A \qquad \text{Eq. 3.10}$$

The ionisation probability terms refer to the density (n_A) of the atomic element present (A), the specimen thickness (t) and the ionisation cross section (Q_A). The overall detection efficiency depends on the collection solid angle of the detector (Ω) and the detector efficiency (ε_A).

K-factor method

The K-factor (k) quantification method was developed by Cliff & Lorimer[34] and provides a way to quantify the relative concentration (C) between two elements (A, B) from their peak intensities (I):

$$\frac{C_A}{C_B} = k_{AB} \frac{I_A}{I_B} \qquad \text{Eq. 3.11}$$

K-factors vary depending on the combination of elements involved and microscope parameters used. Hence, K-factor values should be determined experimentally by comparing to a reference element (e.g., silicon, Si) under the same conditions as those used to collect the X-ray intensity data from the specimen using the formula:

$$k_{AB} = \frac{k_{A_{Si}}}{k_{B_{Si}}} \qquad \text{Eq. 3.12}$$

Zeta-factor method

A more recent approach to quantification has been to use thin film pure element standards, which is based upon the assumption that the measured characteristic X-ray intensity is proportional to the density (ρ) and thickness (t) of the specimen, also known as mass-thickness (ρt), where X-ray absorption effects are insignificant.[35] The relation is provided via a ζ-factor, from which concentration can be calculated as:

$$C_A = \zeta_A \frac{I_A}{\rho t D_e} \qquad \text{Eq. 3.13}$$

The main advantage of this method over the k-factor approach is that only a single reference specimen with a known thickness is required. Alternatively, if the density and concentration are known the expression above can be used to determine and map the specimen thickness.

3.5. Electron Energy Loss Spectroscopy

Similar to EDS, electron energy loss spectroscopy (EELS) is a technique which can yield information on the chemical properties of the sample. Incident electrons which are inelastically scattered will undergo a momentum change and subsequent loss in kinetic energy.[9] An electromagnetic prism is used to spatially separate these electrons, where they are collected and measured to form an energy loss spectrum. It is useful to separate the spectrum into low-loss and core-loss regions, where various inelastic interactions with the specimen can appear as distinct features, as summerised in **Figure 3.4** and discussed below.

3.5.1. Low-loss Spectra

A stand-out feature of the low-loss (<50 eV) region of the spectrum is the large peak at 0 eV. This is known as the zero-loss peak (ZLP) and results from the electrons transmitting the sample with no detectable energy loss. The ZLP is useful as it can be used as a reference to align and correct for any drift in the spectra. Furthermore, as the extent of inelastic scattering is dependent on the specimen thickness, the ZLP intensity (I_{ZLP}) can be used to calculate the relative thickness of the specimen in relation to the electron mean free path, denoted as (t/λ).[37] This is known as the log-ratio method:

$$\frac{t}{\lambda} = -\ln\frac{I_{total}}{I_{ZLP}} \qquad \text{Eq. 3.14}$$

where (I_{total}) is the total intensity of the specimen calculated by summing the ZLP intensity and inelastic scattering intensity contributions. Absolute thickness values can also be calculated using the Kramers-Kronig method, in which a theoretical mean free path value is calculated based on the assumption it is proportional to the specimen density.[38]

A much less intense, broad peak is also often seen in the 1-100 eV range. This is known as the plasmon peak and arises from inelastic scattering by high orbital shell electrons. The effect is an induced excitation of the specimen in the form of electron oscillations.[39]

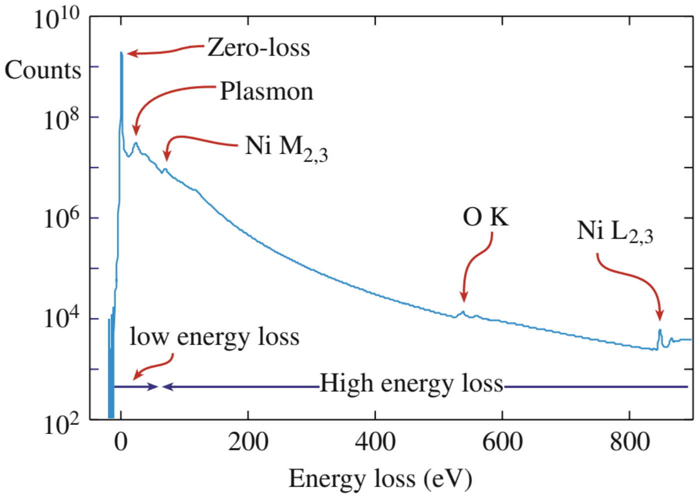

Figure 3.4: Key features of an example EELS spectra. *Intensity is plotted logarithmically to highlight both low-loss and core-loss simultaneously. The zero-loss peak arises from the collection of elastically scattered electrons. The plasmon peak occurs from inelastic scattering by high orbital shell electrons. The remaining peaks are characteristic core-loss edges from which the intensities and structure can yield chemical information of the specimen. Figure adapted with permission from Williams and Carter (2009).*[12]

3.5.2. Core-loss Spectra

The high-loss, or core-loss, region of the spectrum (>50 eV) contains peaks, or ionisation ‘edges’, which corresponds to electrons which have been inelastically scattered by a core electron of a specimen atom. Analogous to the X-rays generated during EDS, these electrons undergo a characteristic energy loss which is dependent on the element and orbital shells involved.[9] Fine structure in the onset of the edges are also characteristic of the element and localised chemical properties.[40] Unlike X-rays in EDS, the electrons in EELS do not suffer from adsorption effects or rely on an element-dependent fluorescent yield.[41] This makes EELS particularly effective at analysing light elements.

Bibliography

1. Rayleigh, L. Investigations in optics, with special reference to the spectroscope. *Philos. Mag. J. Sci.* **8**, 261–274 (1879).
2. de Broglie, L. Recherches sur la théorie des Quanta. *Ann. Phys.* **10**, 22–128 (1925).
3. Knoll, M. & Ruska, E. Das Elektronenmikroskop. *Zeitschrift für Phys.* **78**, 318–339 (1932).
4. van der Mast, K. D. Field emission, developments and possibilities. *J. Microsc.* **130**, 309–324 (1983).
5. Goodhew, P. J., Humphreys, J. & Beanland, R. *Electron Microscopy and Analysis*. (CRC Press, 2000).
6. Sondheimer, E. H. The mean free path of electrons in metals. *Adv. Phys.* **50**, 499–537 (2001).
7. Ayache, J., Beaunier, L., Boumendil, J., Ehret, G. & Laub, D. *Sample Preparation Handbook for Transmission Electron Microscopy*. vol. 2 (Springer Science & Business Media, 2010).
8. Wang, Z. *Elastic and Inelastic Scattering in Electron Diffraction and Imaging*. (Springer Science & Business Media, 2013).
9. Egerton, R. F. *Electron Energy-loss Spectroscopy in the Electron Microscope*. (Springer Science & Business Media, 2011).
10. Reimer, L. & Kohl, H. *Transmission Electron Microscopy Physics of Image Formation*. (Springer, 2008).
11. Nellist, P. D. & Pennycook, S. J. The principles and interpretation of annular dark-field Z-contrast imaging. in *Advances in Imaging and Electron Physics* vol. 113 147–203 (2000).
12. Williams, D. B. & Carter, C. B. *Transmission Electron Microscopy*. (Springer Science

& Business Media, 2009).

13. Nellist, P. D. Theory and Simulations of STEM Imaging. in *Aberration-Corrected Analytical Transmission Electron Microscopy* (ed. Brydson, R.) 89–110 (John Wiley & Sons, Ltd, 2011).

14. Kimura, K., Hata, S., Matsumura, S. & Horiuchi, T. Dark-field transmission electron microscopy for a tilt series of ordering alloys: toward electron tomography. *J. Electron Microsc. (Tokyo).* **54**, 373–377 (2005).

15. Cowley, J. M. & Fields, P. M. Dynamical theory for electron scattering from crystal defects and disorder. *Acta Crystallogr. Sect. A* **35**, 28–37 (1979).

16. Egerton, R. F. *Physical Principles of Electron Microscopy*. (Springer, 2005).

17. Brydson, R. *Aberration-corrected Analytical Transmission Electron Microscopy*. vol. 3 (John Wiley & Sons, 2011).

18. Haider, M., Hartel, P., Müller, H., Uhlemann, S. & Zach, J. Current and future aberration correctors for the improvement of resolution in electron microscopy. *Philos. Trans. R. Soc. A Math. Phys. Eng. Sci.* **367**, 3665–3682 (2009).

19. Krivanek, O. L., Dellby, N. & Lupini, A. R. Towards sub-Å electron beams. *Ultramicroscopy* **78**, 1–11 (1999).

20. Krivanek, O. L., Lovejoy, T. C., Dellby, N. & Carpenter, R. W. Monochromated STEM with a 30 meV-wide, atom-sized electron probe. *Microscopy* **62**, 3–21 (2013).

21. Krivanek, O. L. *et al.* High-energy-resolution monochromator for aberration-corrected scanning transmission electron microscopy/electron energy-loss spectroscopy. *Philos. Trans. R. Soc. A Math. Phys. Eng. Sci.* **367**, 3683–3697 (2009).

22. Egerton, R. F. Control of radiation damage in the TEM. *Ultramicroscopy* **127**, 100–108 (2013).

23. Kirkland, E. J. *Advanced Computing in Electron Microscopy*. (Springer Science &

Business Media, 2010).

24. Van Dyck, D. Persistent misconceptions about incoherence in electron microscopy. *Ultramicroscopy* **111**, 894–900 (2011).

25. Crewe, A. V. & Walls, J. A scanning microscope with 5 Å resolution. *J. Mol. Biol.* **48**, 375–393 (1970).

26. Pennycook, S. J. Z-contrast STEM for materials science. *Ultramicroscopy* **30**, 58–69 (1989).

27. Cosgriff, E. C., Oxley, M. P., Allen, L. J. & Pennycook, S. J. The spatial resolution of imaging using core-loss spectroscopy in the scanning transmission electron microscope. *Ultramicroscopy* **102**, 317–326 (2005).

28. Szegner, J., Yeung, K. L. & Varma, A. Effect of catalyst distribution in a membrane reactor: experiments and model. *AIChE J.* **43**, 2059–2072 (1997).

29. Auger, P. Sur l'effet photoélectrique composé. *J. Phys. Radium* **6**, 205–208 (1925).

30. Schlossmacher, P., Klenov, D. O., Freitag, B. & von Harrach, H. S. Enhanced detection sensitivity with a new windowless XEDS system for AEM based on silicon drift detector technology. *Micros. Today* **18**, 14–20 (2010).

31. Li, Y. H., Chen, Z. & Loretto, M. H. Spurious contributions from scattered electrons in thin-film X-ray microanalysis. *J. Microsc.* **170**, 259–264 (1993).

32. Zaluzec, N. J., Burke, M. G., Haigh, S. J. & Kulzick, M. A. X-ray energy-dispersive spectrometry during in situ liquid cell studies using an analytical electron microscope. *Microsc. Microanal.* **20**, 323–329 (2014).

33. Kothleitner, G. *et al.* Quantitative elemental mapping at atomic resolution using X-ray spectroscopy. *Phys. Rev. Lett.* **112**, 1–5 (2014).

34. Cliff, G. & Lorimer, G. W. The quantitative analysis of thin specimens. *J. Microsc.* **103**, 203–207 (1975).

35. Watanabe, M. & Williams, D. B. The quantitative analysis of thin specimens: a review of progress from the Cliff-Lorimer to the new ζ-factor methods. *J. Microsc.* **221**, 89–109 (2006).

36. Kramers, H. A. On the theory of X-ray absorption and of the continuous X-ray spectrum. *Philos. Mag. J. Sci.* **46**, 836–871 (1923).

37. Malis, T., Cheng, S. C. & Egerton, R. F. EELS log-ratio technique for specimen-thickness measurement in the TEM. *J. Electron Microsc. Tech.* **8**, 193–200 (1988).

38. Iakoubovskii, K., Mitsuishi, K., Nakayama, Y. & Furuya, K. Thickness measurements with electron energy loss spectroscopy. *Microsc. Res. Tech.* **71**, 626–631 (2008).

39. Egerton, R. F. & Malac, M. EELS in the TEM. *J. Electron Spectros. Relat. Phenomena* **143**, 43–50 (2005).

40. Brydson, R., Sauer, H., Engel, W. & Zeitler, E. EELS as a fingerprint of the chemical co-ordination of light elements. *Microsc. Microanal. Microstruct.* **2**, 159–169 (1991).

41. Leapman, R. D. & Hunt, J. A. Comparison of detection limits for EELS and EDXS. *Microsc. Microanal. Microstruct.* **2**, 231–244 (1991).

Chapter 4

In situ Gas Cell Transmission Electron Microscopy

The strategic development of highly active, selective, and stable heterogeneous catalysts is essential in the goal towards global economic and environmental sustainability. Particularly vital is their progress in energy applications[1], pollution control[2] and chemical synthesis from waste biomass[3]. A comprehensive knowledge of reaction mechanisms is crucial in the design of new catalysts and understanding the structure-activity relationship during reaction conditions can provide insight into their physicochemical properties.[4] To achieve this, the atomic-scale characterisation of catalyst structure and morphology can help guide improvements in the synthesis process.[5]

Transmission electron microscopy provides the ability for spatially resolved requirements, allowing structural and chemical information to be acquired simultaneously. However, the benefits gained by using electrons in microscopy comes with a caveat; the high vacuum conditions necessary to (1) protect the electron gun, and (2) avoid electron scattering from gaseous species in the column, which leads to a loss in image quality.[6] This requirement limits the environmental conditions available for study by traditional TEM to static, vacuum observation devoid of any potentially reactive gas environments. To address this problem, microscope advancements have branched into two varieties: differentially pumped systems and windowed environmental cell systems. In this chapter both systems are discussed, with emphasis on the development of the windowed cell systems employed for this project. A series of example *in situ* gas cell applications towards the study of heterogeneous catalysis systems is also discussed.

4.1. Gas Phase TEM Instrumentation

4.1.1. Differentially Pumped Systems

To overcome the gas-inclusion limitations, one approach has been through modification of the TEM column to accommodate apertures and pumps, in microscopes which have come to be known as "open-type" environmental TEMs, or ETEMs.[7,8] The apertures allow unhindered transmission of the electron beam and confine gas to the objective lens area around the sample, with any overflow being evacuated by the pumps.[9] Modern ETEMs now contain a series of apertures and isolated volumes, in what is referred to as a differentially pumped system, allowing a higher pressure to be used than that of single aperture alternatives.[10]

The limitations of ETEMs are largely due to the reduced mean-free path of the electrons when transmitting through the gas environment, a distance typically in the range of 4-7 mm depending on the ETEM design.[11] The increased electron scattering with gas type and concentration leads to a trade-off between pressure and spatial resolution.[12] Furthermore, trace amount of gases have the potential to inflict permanent damage to the electron source, limiting the current maximum useable pressure to ~60 mbar.[13] For H_2 and N_2 gas atmospheres, it has been shown that a resolution of 0.1 nm can be maintained at pressures of up to 10 mbar.[14] This pressure is relatively low when compared to the operational conditions typical of heterogeneous catalysts, which tend to function at pressures of 10's of bars to provide the most efficient reaction conditions.[15] The time required to adjust the environmental temperature and then stabilize thermal drift are also seen as drawbacks of ETEMs, as is the potential for gas to react with the heater holder cup, exposing the specimen to different gases than that of the original mixture.

4.1.2. Windowed Cell Systems

The second approach for observation of materials under environmental conditions is to confine the gas within a small "closed-type" environmental cell. This method involves a specialised TEM holder to allow construction of the cell containing the gaseous atmosphere, which can be static or flowed at a controllable rate.[16] An immediate advantage of this approach is the usability in any standard TEM, as opposed the costly purchase of a dedicated ETEM.

The windowed cell design incorporates electron-transparent membranes to allow the beam to transmit and interact with the specimen whilst simultaneously containing the gas from entering the TEM column. In comparison to the differential pumping system this allows a reduction in the distance the electron beam must pass through the gas and subsequently an increase in useable pressure. Achievable pressures are typically up to 1.0 bar for commercial systems, however other systems have been developed to reach higher pressure.[17] The cell can also be functionalised with heating elements and electrical contacts to provide temperature control up to 1000°C. However, the presence of a window membrane material increases the extent of electron scattering and so are produced as thin as possible while still maintaining structural integrity at elevated gas pressures. Original constructions of this system were developed around configurations of traditional specimen grids.[18,19] More recently, the development of micro-electromechanical systems (MEMS) has been employed in order to develop more robust gas cells designs.[12,20–25]

4.2. MEMS-based Gas Cells

4.2.1. Initial Development

Principal windowed cell designs used electron transparent amorphous carbon film to contain low pressures of gas.[21] More recently, cell designs incorporating micro-electromechanical systems (MEMS) technology were manufactured to produce a "nanoreactor" for containing gaseous environments within the TEM.[22,23] An overview of the nanoreactor is provided in **Figure 4.1**. The device involved gluing together two silicon substrate chips, each including 1 mm^2, 1.2 µm thick SiN_x membrane window. The use of amorphous SiN_x was to avoid diffraction contrast effects and the relatively thick geometry enabled the cell to maintain a 1.0 bar pressure differential between the cell and TEM column. Electron transparency was increased by thinning small areas of the membrane to 10 nm, reducing scattering sufficiently for high resolution imaging. The incorporation of gas inlet/outlet openings and integrated spacers provided a 4 µm channel through which gas could flow. Controllable temperature in the cell was provided by embedding a spiralled thin-film Pt wire within the windows, allowing resistive heating of up to 500°C. A custom specimen holder was also designed to provide the electrical and gas connections to the cell.

HRTEM imaging during the formation of Cu nanocrystals on ZnO support, a common catalyst for methanol synthesis, was employed to evaluate the performance of this system.[22] To achieve this, a resolution of at least 0.2 nm is required, which had been previously demonstrated in a differentially pumped ETEM system at gas pressure of ~1 mbar.[26] The CuO catalyst was transformed into catalytically active Cu nanoparticles by stepped heating to 500°C in H_2 at 1.2 bar pressure.[22] Atomic lattice fringes were observed with spacings of 0.21 and 0.18 nm, corresponding to the {111} and {200} planes of Cu, respectively. This was relatively close to the resolution limit of the microscope (0.14 nm), indicating minimal image degradation caused by the environmental cell.

An *in situ* heating holder for ETEM has been developed, which aimed to address the performance problems associated with other designs, such as slow heating/cooling rates and

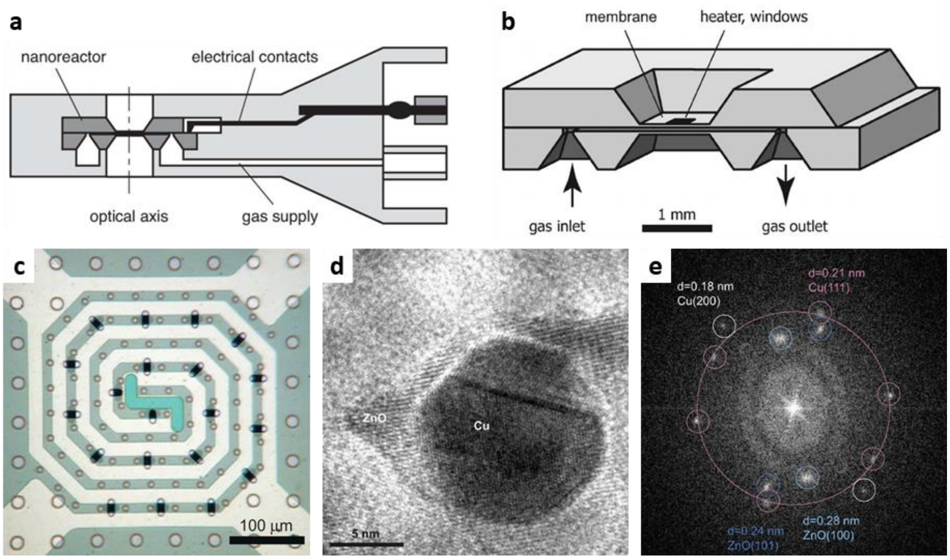

Figure 4.1: Overview of the in situ nanoreactor design from Creemer et al*. Schematic cross-section illustration of* ***(a)*** *the holder tip construction and* ***(b)*** *the two-chip nanoreactor cell.* ***(c)*** *Optical image of the* SiN_x *membrane, with the bright spiral indicating the Pt heater location. The ovals between the spiral arms are the thinned electron transparent regions. The evenly distributed circles are the membrane spacers.* ***(d)*** *HRTEM image of the Cu/ZnO catalyst in 1.2 bar* H_2 *at 500°C used to test resolution capabilities under reaction conditions and* ***(e)*** *the corresponding Fourier transform. Image adapted with permission from Creemer et al. (2010).*[23] *Copyright 2011 IEEE.*

considerable image drift.[24] To achieve this a ‘high-conductivity ceramic’ membrane was employed as both the heating element and sample support. This novel heating arrangement demonstrated heating and cooling rates at 10^6 °C/s due to the low thermal mass of the membrane and sample drift significantly reduced by the regular geometry of the supporting Si chip.[24]

Innovations were made to adapt the heater design into a closed cell system which could also flow gas.[27] A new specimen holder was designed to incorporate the heater as the top component of a two-chip device. This chip included a 30 nm thick amorphous SiN window deposited over holes etched in the ceramic membrane heater, with a bottom, smaller chip supporting a slightly thicker (≤50 nm) membrane. **Figure 4.2a-c** demonstrates the series of steps required to assemble the gas cell system. The vacuum seal between the Si chips is achieved using rubber O-rings and integrated spacers provide a 5 μm opening for the gas to flow through. A precisely machined titanium lid is screwed down against the chips to ensure a good seal against the O-rings and electrical contact with the integrated wiring. A schematic of the assembled cell geometry at the membrane window is illustrated in **Figure 4.2d**.

Trials were carried out using a range of catalysts (either dry-loaded or drop casting them onto the supporting chip via an ethanol or hexane suspension method) to minimize detrimental contamination effects.[27] It was found that by employing pre-assembly plasma cleaning of the chips and post-assembly beam showers within the microscope contamination was kept at a minimum, especially at temperatures greater than 250°C. HAADF and BF STEM imaging of Rh nanoparticles on a $CaTiO_3$ support achieved atomic resolution during exposure to 1.0 bar of air at 350°C (**Figure 4.2e,f**).

Other environmental cell designs combined more traditional holder constructions with MEMS components. An environmental cell containing a spiral shaped fine tungsten wire heating element and micropressure gauge (MPG) was reported, with gas inlet and outlet tubing also incorporated in the cell-holder design, shown in **Figure 4.3**.[12] This design had built on previous work, where specimen holders had been configured to be used in a similar manner with differentially pumped ETEMs.[28–30] In this approach, specimens were loaded directly onto

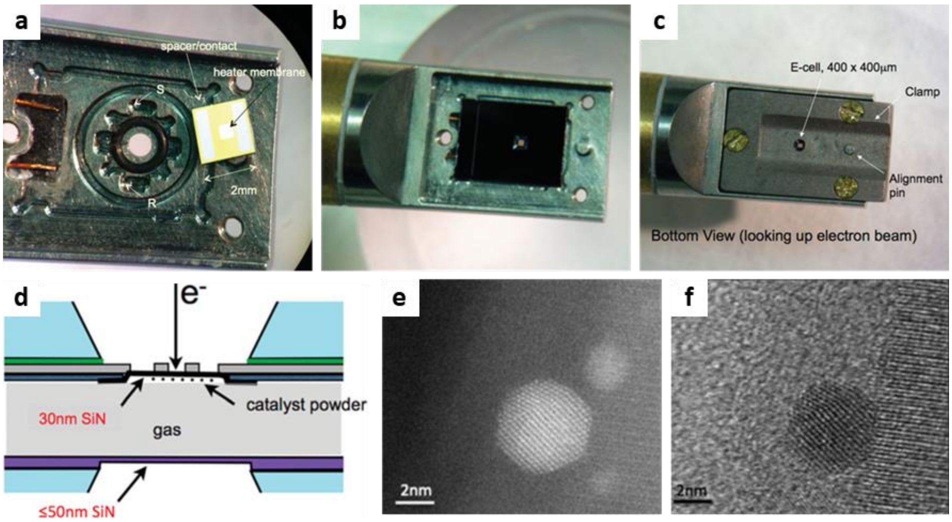

Figure 4.2: Overview of the closed cell design with membrane heating from Allard et al. (a) *Initial loading of the smaller O-ring and lower chip into the holder tip. Channels for the gas supply (S) and return (R) are machined within the tip.* ***(b)*** *Positioning of the upper heating chip (which sits on a larger O-ring) with contacts connecting to the holder's integrated electrical leads.* ***(c)*** *View of the fully assembled gas cell with clamping lid screwed into place to form a tight seal between the chips and O-rings.* ***(d)*** *Schematic diagram illustrating the windowed area of the assembled cell.* ***(e)*** *HAADF and* ***(f)*** *BF images of a Rh nanoparticle supported on* $CaTiO_3$ *at 350°C in 1.0 bar air, demonstrating atomic resolution capabilities during reaction conditions. Image adapted with permission from Allard et al. (2012).*[27]

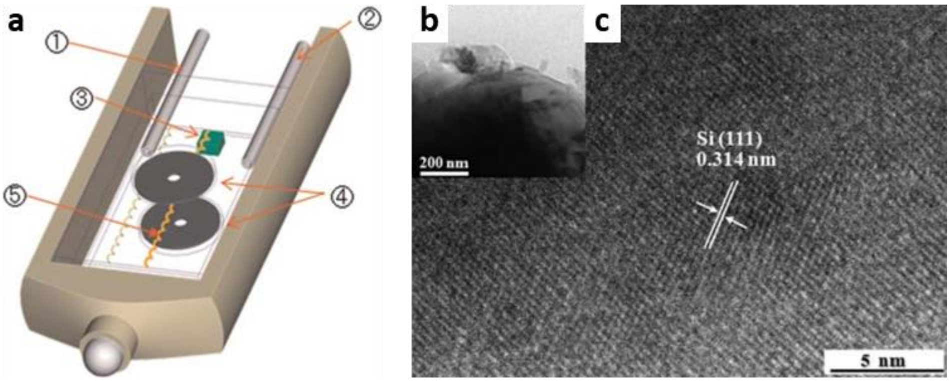

Figure 4.3: Overview of the windowed environmental cell design from Yaguchi et al. (a) *Illustration of the various cell components (1. Outlet and 2. Inlet gas tubes; 3. Micropressure gauge; 4. Electron transparent windows; 5. Fine tungsten wire heating element).* ***(b)*** *Low-mag and* ***(c)*** *HRTEM images of a single crystal silicon particle during exposure to 600°C in 0.1 bar of air. Image adapted with permission from Yaguchi et al. (2011).*[12]

the heating element, which could provide temperatures of up to 1500°C. The element was located between two 15 nm thick Si_3N_4 windows, each supported by 0.2 mm thick Si disc. The MEMS-fabricated MPG was designed to be placed inside the cell to accurately measure the pressure. The screw closure design of this system was advantageous over that of the nanoreactor design in that a glueless approach led to a reported reduction in contamination effects. A single crystal Si particle was used to assess the imaging capabilities of the cell at 600°C in air at 10^4 Pa (0.1 bar). Atomic resolution of Si{111} lattice fringes with spacing of 0.314 nm were observed. A drawback of this system was the 1.0 mm (minimum) space between the membranes used to contain the gas. This led to a large path length for electrons to pass through and, as such, reduced resolution in comparison to other in situ cells being developed at the time. Atomic imaging was achieved, but only at gas pressures more comparable to that of ETEM (100 mbar).

4.2.2. Pressure Limitations

As discussed, the emergence of MEMS-based cells provided an improvement in operating pressure from the millibar ranges of ETEM to 1.0 bar for current commercial gas cell systems. However, there remains a pressure gap between the achievable pressures and those used industrially for high pressure reactions such as ammonia synthesis, which typically require 100-300 bar pressures.[31] The study of such systems requires a *quasi in situ* workflow, which aims to decouple the catalytic reaction and TEM analysis.[32] This approach involves TEM observation of the catalyst pre- and post-reaction (in vacuum), between which the sample is transferred in a controlled environment to a high pressure reactor with accompanying mass spectrometer (MS) for product conversion measurement. Due to the dissociated collection of TEM and MS measurements during this process, caution must be exercised when attempting to establish structure-activity relationships from any subsequent analysis.

In efforts to increase the feasible pressures in gas cells further, a refinement of the nanoreactor design was made to reach 4.0 bar.[17] This was achieved by slightly increasing the thickness of the SiN_x window imaging regions from 10 to 15 nm and rounding the corners at which the membrane attaches to the silicon chip to reduce stress. Hydrogenation of Pd particles at 4.0 bar/240°C was used to demonstrate the cell capabilities, highlighting the observed reduction of lattice parameters in the diffraction patterns.[17] In a separately reported test of the same system a pressure of 4.5 bar and temperature of 400°C was also reported.[33]

Further nanoreactor design refinements used pillars to connect the membranes and prevent bulging, which resulted in an attainable pressure of 14 bar while maintaining high temperature operation (<800°C).[34] The drawback of this device is the inaccessibility of the cell interior, with the sample requiring a challenging deposition process involving loading through a microfluidics inlet.

It should be noted in both attempts to increase the pressure range of the nanoreactor design to date neither has been used to report on further work beyond their initial demonstrations. While both concepts have great potential for future catalysis studies, commercialised systems remain the popular choice.

4.2.3. Spatial and Temporal Resolution

The introduction of gas in the TEM leads to increased scattering of the electron beam, resulting in intensity loss at the various detectors. This effect can lead to a considerable decrease in the signal-to-noise ratio (SNR), making subsequent analysis challenging.[35] A report using ETEM to measure the decrease in CCD intensity as a function of pressure for H_2, He, N_2, O_2 and Ar, demonstrated scattering to be dependent on both gas pressure and atomic number.[36] An advantage of windowed gas cells is the reduced path length electrons have to pass through the gas. However, the SiN_x membranes require a minimum thickness to maintain structural integrity and reliably provide a high differential pressure between the cell interior and the microscope column. A subsequent effect of this pressure difference is bulging of the membranes. Thus, scattering from the membranes (material and thickness dependant), varying gas path length (pressure dependant) and gas type are all factors which contribute to the ultimate resolution in gas cell (S)TEM. A theoretical treatment for calculating resolution in windowed liquid cells has been reported, which can also be extended to gas cells.[37]

Temporal resolution is also an important consideration. Ideally, *in situ* TEM would allow observation of the product formation at active sites during reaction conditions. However, the lifetimes of structural transitions[38] and reaction events[39] have time durations in the range of picoseconds. Commercial charge-coupled devices (CCDs) and direct electron detectors (DEDs) are currently limited to the milli-/microsecond range, as such these observations are out of reach with current detection technologies. Technical development of ultrafast TEM[40] may one day provide these temporal abilities, although due to the metastable nature of catalytic surfaces, the challenge will be validating any structural changes to be inherent of a conversion event as opposed to that from electron irradiation.

4.2.4. Analytical Capabilities

While the initial progress of environmental cells enabled routine imaging acquisition during *in situ* study, complementary analytical information via X-ray energy dispersive spectroscopy (EDS) and electron energy loss spectroscopy (EELS) has been more challenging.

As discussed in Section 2.4.2., X-ray emission during TEM occurs isotropically, with the extent of signal detected dependent on the collection angle, which itself is limited by the geometry of the microscope pole pieces. **Figure 4.4a** illustrates the additional constraint introduced by the geometry of the gas cell/holder, with the low penumbra in this configuration effectively blocking the X-ray line-of-sight from the specimen to the EDS detector.[41] To address this problem, design modifications were made to the cell and holder of a commercially available Protochips Poseidon™ 200 Liquid Flow stage.[41] **Figure 4.4b,c** illustrates the modifications in cross section, highlighting the removal of material from the sidewalls of the cell (green), clamping mechanism (grey) and holder body (orange). To compare the changes, spectra were collected using both the unmodified and modified systems encapsulating Au nanoparticles (**Figure 4.4d,e**). Results from the unmodified holder at 0° tilt provides only characteristic X-ray signal from Fe and Co, which is attributed to secondary scattering from the objective lens pole piece. The effect of tilting the holder 20° to increase specimen line-of-sight to the detector only resulted in a barely discernible Si signal from the membrane window

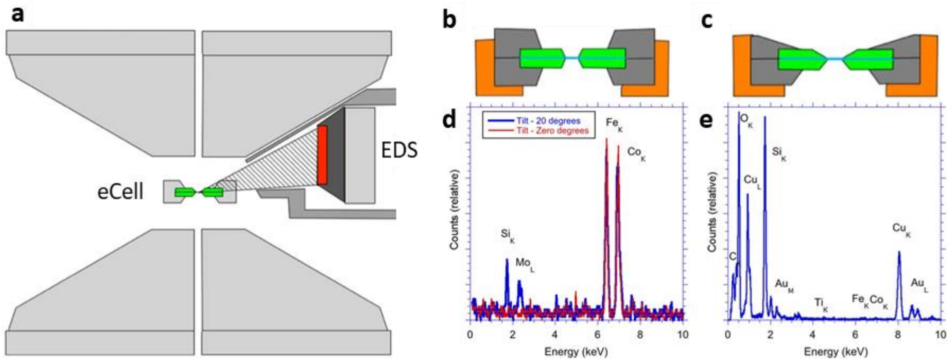

Figure 4.4: Increased EDS signal detection from a modified environmental cell design. (a) *Schematic cross section of a typical eCell/EDS detector system showing the effect of detector shadowing from the penumbra of the holder.* ***(b,c)*** *Cross section diagram of the holder geometry before (b) and after (c) modifications.* ***(d,e)*** *Spectra from a cell encapsulating Au NPs before (d) and after (e) modifications. Note the increased range of characteristic X-ray peaks resulting from the removal of holder/cell material shadowing the detector. Image adapted with permission from Zaluzec et al. (2014).*[41]

and a small Mo peak, the origin of which was not reported. In contrast, spectra from the modified holder demonstrated a marked increase in signal acquisition, detecting the low energy peaks from C, N, and O, as well as from the Au NP specimen. Several other system peaks were also identified (Si, Ti, Fe, Co, and Cu).

Comparable changes were made to the Protochips Atmosphere™ gas cell design and used to characterise the behaviour of a TiO_2-supported PdCu bimetallic catalyst during *in situ* reduction (1.0 bar H_2).[42] Elemental mapping from the EDS results provided readily discernible compositional features, such as the formation of core-shell structures and Janus particles, which were not readily apparent through HAADF imaging alone.

EELS analysis can provide localised information on the elemental composition and oxidation state in the (S)TEM study of heterogeneous catalysts.[43] Understanding how these properties change during exposure to varying reaction conditions is crucial in the development of new catalysts and makes the use of EELS during *in situ* observation highly desirable. However, EELS is limited by the effective sample thickness, where the increasing occurrence of several energy-loss interactions (i.e., plural scattering) of the individual incident electrons leads to a significant reduction of the SNR in the resulting spectra.[44] This effect acts to diminish the peak intensity of specimen edges, in extreme cases becoming indistinguishable from that of the low SNR noise. This detrimental effect has resulted in a notable underuse of this technique in reporting literature when windowed cells are employed.

4.3. Gas Cell Application to Heterogeneous Catalysis

Gas cell TEM has been employed to investigate various aspects of several catalytic reactions, including catalysts important to CO oxidation[45–49], CO_2 reduction[50], the water gas shift reaction[51] and Fischer-Tropsch synthesis[52,53]. The investigation of novel catalytic materials has also been a focus of studies, including three-way[54], core-shell[55], and high-entropy alloy[56,57] catalysts. To provide context into the application of gas cell TEM towards heterogenous catalysis study in more detail, a series of example studies will be discussed in this section.

4.3.1. CO Oxidation

Catalytic oxidation of toxic CO to relatively harmless CO_2 is an important reaction for processing petrochemical gas streams.[58] An oscillation of product formation has been demonstrated for this system and is attributed to dynamic reconstruction of the catalyst surface.[26,59] This behaviour was recently demonstrated to occur on Pt nanoparticles (NPs) exposed to 1.0 bar $CO/O_2/He$ (3%:42%:55%) at 390°C.[45] **Figure 4.5** shows the CO, CO_2 and O_2 pressures within the reactor via mass spectrometry (MS) and the response in particle morphology imaged using TEM. The oscillating pressures of CO and CO_2 are anti-phase to each other, highlighting periods where CO is actively being oxidised to CO_2. This behaviour was maintained at fixed temperatures up to 460°C. The variation in CO/CO_2 pressure leads to a varying gas composition surrounding the Pt NP, causing the fluctuating change in morphology. The cyclic transformation was validated using a shape factor corresponding an elliptical fit of the imaged nanoparticles to their relative difference in area. Particles were found to change from a spherical to a more facetted shape as CO conversion increased.

Several more *in situ* gas cell studies have since been performed on Pt NPs. Correlating STEM with Wulff construction modelling demonstrated the reversible roughening of {100} facets into stepped high Miller index facets induced by CO adsorption.[46] Further observations of the morphological and structural dynamics were used to suggest the previously reported

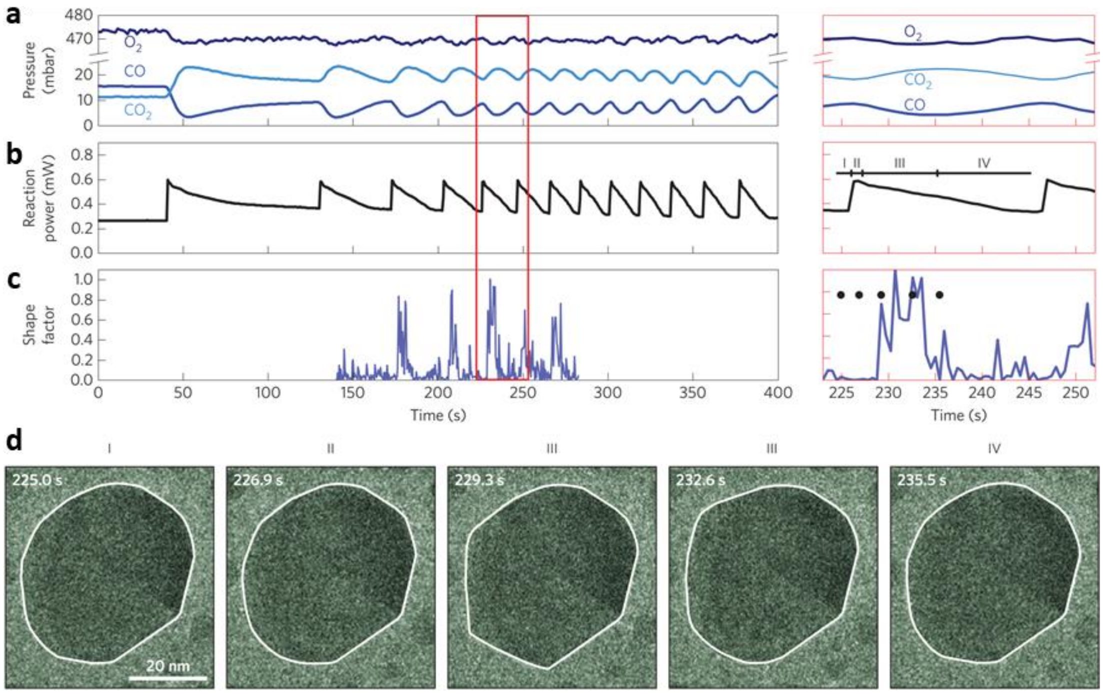

Figure 4.5: In situ CO oxidation oscillation correlation with Pt nanoparticle morphology. ***(a)*** *Mass spectrometry data of CO, O$_2$ and CO$_2$ pressures within the cell.* ***(b)*** *Variations in power to the reactor heater to compensate for increased heat from the exothermic oxidation reaction and maintain constant temperature.* ***(c)*** *Time resolved shape factor for the Pt nanoparticles, with zero representing a perfectly spherical particle and increasing with growth of the facetted profile* ***(d)*** *Series of TEM images exhibiting one cycle of the reversible morphological change. Image reproduced with permission from Vendelbo et al. (2014).*[45]

oscillatory behaviour in the MS originated from the cyclic formation of roughened surfaces rather than the faceting itself, which in turn is dependent on the surface coverage of CO.[49] Extending studies to bimetallic specimens, A study of the response of Pt-Ni NPs to CO exposure with STEM-EDS highlighted varying degrees of metal segregation depending on their initial structure and morphology.[47]

Another important catalyst for CO oxidation are Cu NPs due to their metastable oxide species providing ready transport of surface lattice oxygen during reduction.[60] Cu NPs during oxidation-reduction reaction conditions have been observed using HAADF-STEM imaging.[61] The NPs were first reduced in H_2 (500°C) and then exposed to O_2 (300°C). Imaging revealed a transformation akin to the nanoscale Kirkendall effect, with the differential diffusion rates of O and Cu resulting in the growth of a surface oxide layer and subsequent creation of a central void. This effect has also been demonstrated using Co NPs during a similar reaction.[62]

It should be noted that studying unsupported catalyst NPs is useful in understanding oxidation-reduction mechanisms and the resultant phases important to their reactions. The lack of support generally leads to increased sintering/coalescence effects and morphological changes which are not influenced by a metal-support interaction, a factor which can dramatically alter the product distribution.[63] Industrial catalyst systems require long-term stability to be economically viable, making supports critical to the catalyst design process. In this regard, demonstrating the morphological change of unsupported NPs is limited in its application to industrially relevant reaction conditions. However, using a windowed gas cell requires deposition of the NPs on the window membrane, which effectively then becomes the catalysts support. For commercial *in situ* systems, the membrane material is typically silicon nitride. Hence, when making *in situ* comparisons to *ex situ* analysis of NP catalyst specimens, the potential effects of a silicon nitride support should be explored.

4.3.2. Water Gas Shift

The water gas-shift reaction (WGS: $CO + H_2O \leftrightarrow CO_2 + H_2$) is an important consideration in the production of hydrogen via oxide supported metal NP catalysts. The generally accepted mechanism for this process is the dissociation of H_2O on oxygen vacancies of the support and subsequent reaction of oxygen with CO at the metal-support interface.[64,65] DFT studies exploring the electronic interaction of Pt supported on CeO_2 proposed an electronic metal-support interaction (EMSI) to describe the calculated charge redistributions at their interface.[66] This effect was demonstrated for a TiO_2-support Ni catalyst, after reduction (H_2/450°C) and subsequent cooling (25°C) using TEM.[51,67] Correlative EDS and EELS identified a partial encapsulation of the Ni NPs by a TiO_{2-x} overlayer, which has the potential to increase the number of oxygen vacancies close to the metal-support interface and in turn play a role in the WGS reaction kinetics. However, as these studies were only performed after the specimen had been reduced and cooled within the TEM, they should be considered quasi in situ. Studying the water gas shift reaction on using in situ gas cell TEM is currently under-reported in the literature and hence there are opportunities for novel catalyst research in this area.

4.3.3. Fischer-Tropsch

As previously detailed in chapter 1, Co-based catalysts are the preferred choice for industrial Fisher-Tropsch (FT) application, due to their superior functionality.[68] However, recurring supply shortages and high cost makes cobalt a less than ideal material.[69] As a result, substantial research has been undertaken to minimise the cobalt content in FT catalysts. One route to achieve this is to replace the cobalt core material with a more cost-effective alternative to form a core-shell structure.[70] The resulting geometry, composition and surface structure changes imposed by this approach are all likely to have significant influence on the catalytic behaviour.

Studies on Co NP catalysts with $NiFe_2O_4$ and $ZnFe_2O_4$ cores highlight the importance in the selection of novel core materials and their in-situ TEM characterisation.[71] Initial *ex situ* investigations revealed a Co shell of varying thickness (~3 nm). However, during in-situ H_2 activation, Co in both catalysts was observed to congregate and form small islands on the support surface (230°C and 250°C, respectively).

An *in situ* HRTEM study exploring the effects of varying CO content in the FT feedstock demonstrated carbon deposition on Co NPs when switching from FT reaction conditions of $CO:H_2:N_2$ (1:2:3) to $CO:N_2$ (1:1) at 1.0 bar/500°C (**Figure 4.6**).[52] The observed carbon layering was determined to originate from the dissociation of adsorbed CO, where the oxygen then reacts with CO to form CO_2 and the carbon adatom remains on the surface (i.e., the Boudouard reaction). The carbon deposition also appeared to strain the particle crystal structure, with several twin boundaries observed.

The stable dispersion of supported Co particles during industrial operation is a critical consideration when designing a highly active, selective, and economically viable FT catalyst. The morphological changes of Co-Pt supported on both Al_2O_3 and SiO_2 during H_2 activation and syngas exposure ($H_2/CO = 2$) at 1.0 bar has been reported using HAADF-STEM, highlighting regions of porous Co which undergo fragmentation and subsequent particulate formation during activation at 340°C.[53] The reduced particle size of the Co supported on SiO_2 in comparison to Al_2O_3 was suggested to arise from a weaker metal-support interaction, allowing mass transport of Co to occur more freely. An increase in particle size was measured for both catalysts during syngas exposure. The higher temperature of 430°C could explain the increase in particle size due to Ostwald ripening and/or coalescence processes, which may also be influenced by the volatile complexes of CO and metal during syngas exposure.[72]

4.3.4. Core-shell Catalysts

The reduced amount of costly precious metal and increased activity relative to pure Pt catalysts makes their core-shell alternatives a desirable choice.[73] It has been shown previously that the formation of NPs with an ordered intermetallic Pt_3Co core phase shows higher activity for the oxygen reduction reaction (ORR) than disordered-core alloy NPs[74], with the activity maximised at an annealing temperature ~650°C.[75] *In situ* gas cell studies have been reported, investigating the core-shell formation of Pt_3Co during annealing in 1.0 bar oxygen.[55] To induce the ordered state the NPs were subjected to 720°C for 30 mins, where temperature was then

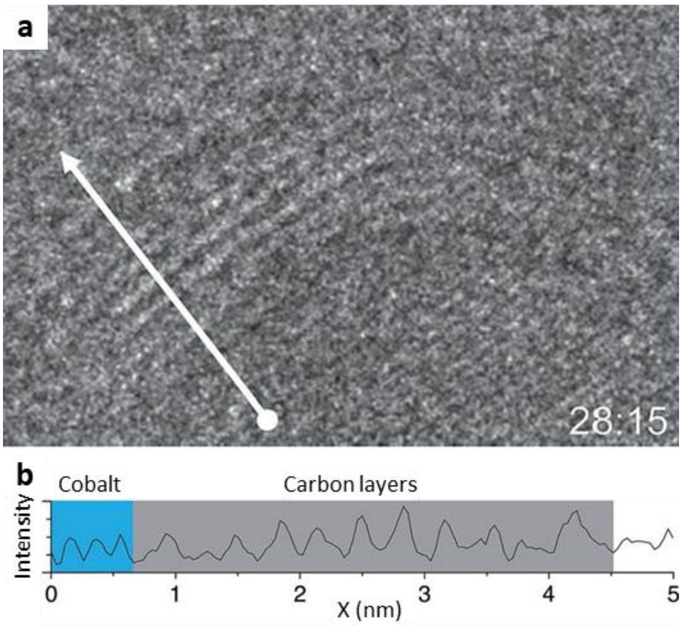

Figure 4.6: In situ carbon layer growth on Co particles during CO-rich gas exposure. *Conditions were switched from syngas to CO:N_2 (1:1) at 1.0 bar/500°C.* ***(a)*** *HRTEM image of carbon layering on Co surface.* ***(b)*** *Intensity profile from white line in (a), line length = 5 nm. Image adapted with permission from Bremmer et al. (2016).*[52]

reduced to 300°C and observations made. **Figure 4.7** shows a time-series of HAADF images demonstrating the evolution of a NP along the [001] zone axis, with time (*t*) commencing when the 300°C was reached. The results show the growth in number of (100) Pt surface layers from 2 (at *t*=0s) to 4 (at *t*=128s), with atomic Pt determined to have migrated from other Pt_3Co clusters.

4.3.5. Three-way Catalysts

The concept of three-way catalysts (TWC) for automotive exhaust-gas treatment have been developed using perovskites doped with precious metals.[76] The catalysts work on the principle that during cyclic reduction-oxidation conditions the precipitation-dissolution of metal NPs occurs, resulting in a regenerative, highly dispersed state. Using HAADF-STEM to image a Rh catalyst supported on $CaTiO_3$ (CTO), dissolution and precipitation effects have been demonstrated during reduction (5%H_2/Ar) and oxidation (pure O_2) cycling conditions at 1.0 bar/600°C **Figure 4.8**.[54] Atomic-scale imaging of a CTO particle along the $[001]_{pseudocubic}$ orientation under reduction conditions (12 mins at 500°C) revealed atomic columns with higher intensity than others. These were determined to be locations at which single atoms of Rh were present on the surface. Separate work using multislice image simulation on an analogous Pt/CTO catalyst revealed the preference for the Pt to occupy Ti sites within the support particles, suggesting the occurrence may also be true for Rh.[77]

In recent studies, gas cell HAADF-STEM and EDS were used to study the sintering of Rh on ZrO_2-based supports in vacuum and in nitrogen.[78] Sintering of Rh was shown to be more readily achievable in N_2 than in vacuum, with smaller particulate formation observed on ZrO_2 doped with yttrium (Y-ZrO_2) in comparison to the pure support. This finding was accounted for with DFT, which suggested a stronger metal-support interaction for Rh to Y-ZrO_2 leading to a retardation in the sintering effect.

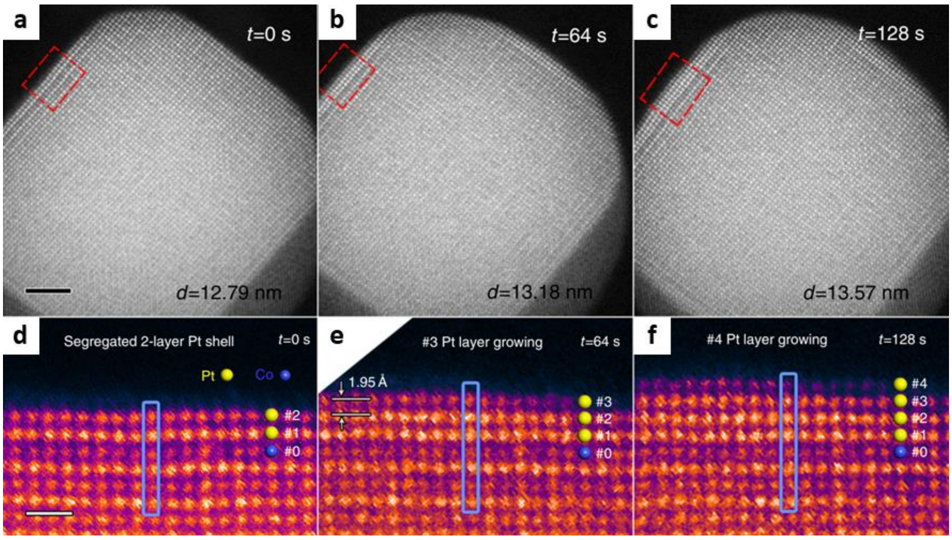

Figure 4.7: In situ Pt (100) surface layer growth during oxygen annealing. (a-c) *HAADF imaging during annealing in 1.0 bar oxygen, acquired at 0, 64, and 128s after reaching 300°C. Scale bar 2 nm.* ***(d-f)*** *False-coloured mapping of the (100) surface corresponding to the red boxes in (a-c). Pt and Co layers are indicated using the yellow and blue spheres, respectively, highlighting layer-by-layer Pt growth. Scale bar, 5 Å. Image adapted with permission from Dai et al. (2017).*[55]

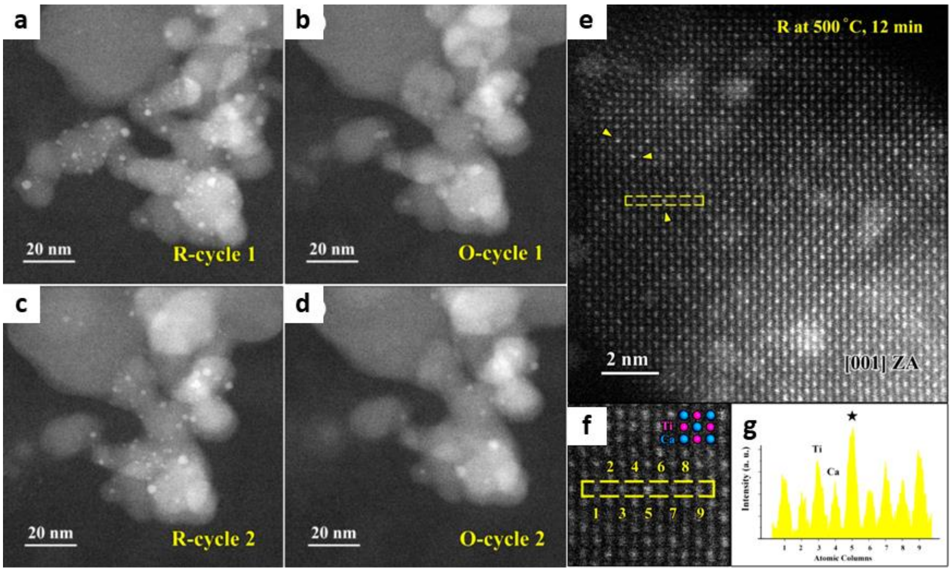

Figure 4.8: In situ gas cell HAADF-STEM imaging of Rh/CTO catalyst. (a-d) *Reduction-oxidation cycling in 1 atm. of 5%*H_2*/Ar (R) or pure* O_2 *(O), respectively, at 600°C demonstrating the occurrence of particulate formation and subsequent dissolution.* ***(e)*** *Atomic resolution imaging of the CTO support under reduction conditions reveals atomic columns of higher intensity in relation to their nearest neighbours, highlighted by yellow arrows.* ***(f)*** *Enlarged region from (e) identifying the location of Ca (blue) and Ti (pink), established through* ***(g)*** *intensity profiling of the atomic columns. Image adapted with permission from Dai et al. (2017).*[54] *Copyright 2017 American Chemical Society.*

4.3.6. High Entropy Alloys

Recent advancements in synthesising single-phase NPs with five or more elements have attracted increasing attention towards the potential for high entropy alloys (HEA).[79] High mechanical strength[80], thermal stability[81], and corrosion resistance[82] makes them suitable for a wide range of applications, including catalysis, where their hydrogenation[83] and water splitting[84] properties have already been investigated. Several applications involve exposure to oxidising/reducing environments. The chemical/structural stability of FeCoNiCuPt HEA NPs and their response to oxidation[56] and reduction[57] conditions have recently been reported using STEM-EDS. At room temperature all elements were observed to be mixed homogeneously throughout the particles, with a thin (~3 nm) surface oxide. Oxidation was achieved by introducing air into the cell and increasing the temperature to 400°C. The periodic collection of EDS maps revealed a Kirkendall effect, with the outward diffusion of metals simultaneous to the growth in the oxide layer (**Figure 4.9**).[56] A subsequent switch to H_2 saw the oxidation layer expand further.[57] An explanation to this is the reduction of the metal in the oxide layer leads to additional outward diffusion of metals from the core.

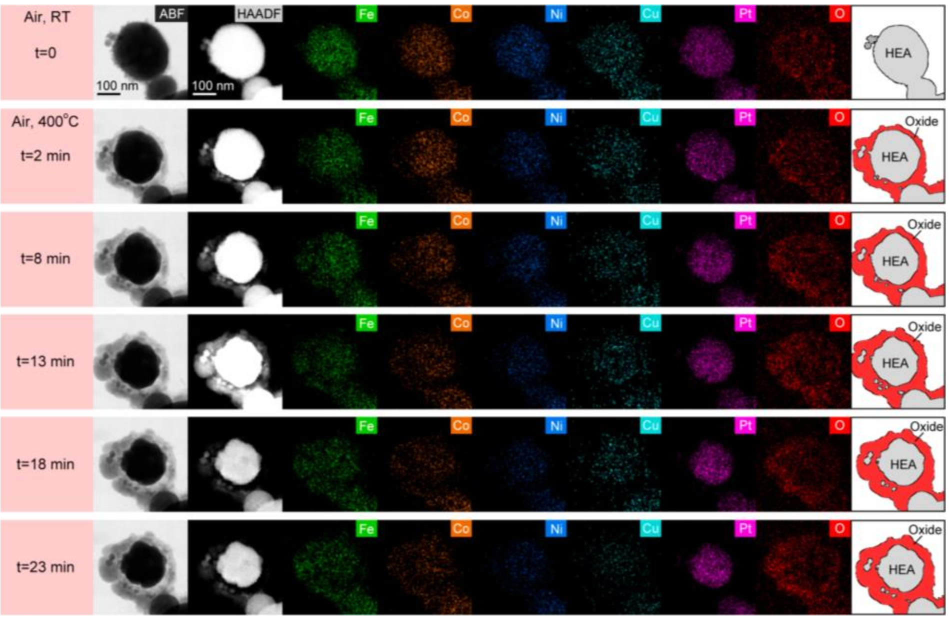

Figure 4.9: In situ STEM-EDS acquisition of HEA NPs during exposure to air at 400°C. *The far-left column indicates acquisition time after oxidation conditions were applied. Second and third columns are ABF and HAADF imaging, respectively. Subsequent six columns are EDS maps of Fe, Co, Ni, Cu, Pt, and O, respectively. Far-right column illustrates the extent of oxide layering on the HEA core, obtained from ABF images. Image adapted with permission from Song et al. (2020).*[56] *Copyright 2020 American Chemical Society.*

4.4. Outlook of Gas Cell TEM

In this chapter the development of gas cell TEM has been discussed and the application towards heterogeneous catalysis has been explored. Commercialisation of MEMS-based cells and their holders for delivery of gas and heating during observation has made *in situ* catalyst research readily accessible to electron microscopy facilities with only standard TEM equipment. The result has led to an significant growth in the study of environmentally induced transformations in solid catalysts, which will surely continue to impact their rational design in the future. However, while great advancements have been made, there remains challenges for *in situ* gas cell TEM to overcome, both specific to heterogenous catalysis and generally towards other materials systems.

One such challenge is the necessity to detect the gaseous products from the reactions during observation, so called "operando" TEM. Chemical, structural, and morphological dynamics are highly dependent on reaction parameters and so correlative analysis of the reaction products is preferential when determining any correlation between catalyst structure and activity. Another route to measure product conversion is via mass spectroscopy. The extension of the gas manifold system to include a residual gas analyser has been recently commercialised, with initial results promising.[85] The importance of correlative analysis can also be extended to techniques beyond the TEM. The small sample volumes required for TEM studies make it a very localised characterisation technique. Other comparable analytical techniques, such as X-ray diffraction (XRD), X-ray photoelectron spectroscopy (XPS), X-ray absorption spectroscopy (XAS)[86], Raman spectroscopy and Infra-red (IR) spectroscopy for example, are therefore essential for developing a robust interpretation of heterogeneous catalyst systems.[87]

Other challenges may be approached through technical development of the gas cell itself. The reduction in spatial resolution brought on by current membranes (based on SiN_x) could be improved through the use of novel 2D materials, such as graphene, which has recently been applied to the construction of liquid cells.[88] A subsequent reduction in plural scattering would also increase SNR and benefit the collection of EELS spectra, a powerful characterisation tool hampered by current cell design. Continually evolving detector technologies, such as direct electron detection, will also continue to improve SNR and acquisition times as we attempt to move towards the temporal resolution of catalytic reaction times.

Bibliography

1. Zhang, Q., Uchaker, E., Candelaria, S. L. & Cao, G. Nanomaterials for energy conversion and storage. *Chem. Soc. Rev.* **42**, 3127–3171 (2013).

2. Iwamoto, M. Air pollution abatement through heterogeneous catalysis. in *12th International Congress on Catalysis* (eds. Corma, A., Melo, F. V, Mendioroz, S. & Fierro, J. L.) vol. 130 23–47 (Elsevier, 2000).

3. Gallezot, P. Direct routes from biomass to end-products. *Catal. Today* **167**, 31–36 (2011).

4. Somorjai, G. A. & Li, Y. *Introduction to surface chemistry and catalysis*. (John Wiley & Sons, 2010).

5. Tao, F. & Crozier, P. A. Atomic-Scale Observations of Catalyst Structures under Reaction Conditions and during Catalysis. *Chem. Rev.* **116**, 3487–3539 (2016).

6. Williams, D. B. & Carter, C. B. *Transmission Electron Microscopy*. (Springer Science & Business Media, 2009).

7. Hashimoto, H., Naiki, T., Eto, T. & Fujiwara, K. High Temperature Gas Reaction Specimen Chamber for an Electron Microscope. *Jpn. J. Appl. Phys.* **7**, 946–952 (1968).

8. Baker, R. T. K. & Harris, P. S. Controlled atmosphere electron microscopy. *J. Phys. E.* **5**, 793–797 (1972).

9. Boyes, E. D. & Gai, P. L. Environmental high resolution electron microscopy and applications to chemical science. *Ultramicroscopy* **67**, 219–232 (1997).

10. Jinschek, J. R. Advances in the environmental transmission electron microscope (ETEM) for nanoscale in situ studies of gas–solid interactions. *Chem. Commun.* **50**, 2696–2706 (2014).

11. Sharma, R. Design and applications of environmental cell transmission electron microscope for in situ observations of gas-solid reactions. *Microsc. Microanal.* **7**, 494–

506 (2001).

12. Yaguchi, T. *et al.* Development of a high temperature-atmospheric pressure environmental cell for high-resolution TEM. *J. Electron Microsc. (Tokyo).* **60**, 217–225 (2011).

13. Sharma, R. An environmental transmission electron microscope for in situ synthesis and characterization of nanomaterials. *J. Mater. Res.* **20**, 1695–1707 (2005).

14. Jinschek, J. R. & Helveg, S. Image resolution and sensitivity in an environmental transmission electron microscope. *Micron* **43**, 1156–1168 (2012).

15. Khodakov, A. Y., Chu, W. & Fongarland, P. Advances in the development of novel cobalt Fischer-Tropsch catalysts for synthesis of long-chain hydrocarbons and clean fuels. *Chem. Rev.* **107**, 1692–1744 (2007).

16. Hansen, T. W. & Wagner, J. B. Controlled atmosphere transmission electron microscopy. *Switz. Springer Int. Publ.* 213–235 (2016).

17. Alan, T. *et al.* Micro-fabricated channel with ultra-thin yet ultra-strong windows enables electron microscopy under 4-bar pressure. *Appl. Phys. Lett.* **100**, 81903 (2012).

18. Heide, H. G. Electron Microscopic Observation of Specimens under Controlled Gas Pressure. *J. Cell Biol.* **13**, 147–152 (1962).

19. Fujita, H., Komatsu, M. & Ishikawa, I. A universal environmental cell for a 3MV-class electron microscope and its applications to metallurgical subjects. *Jpn. J. Appl. Phys.* **15**, 2221–2228 (1976).

20. Konishi, H., Ishikawa, A., Jiang, Y.-B., Buseck, P. & Xu, H. Sealed Environmental Cell Microscopy. *Microsc. Microanal.* **9**, 902–903 (2003).

21. Giorgio, S. *et al.* Environmental electron microscopy (ETEM) for catalysts with a closed E-cell with carbon windows. *Ultramicroscopy* **106**, 503–507 (2006).

22. Creemer, J. F. *et al.* Atomic-scale electron microscopy at ambient pressure.

Ultramicroscopy **108**, 993–998 (2008).

23. Creemer, J. F. *et al.* A MEMS reactor for atomic-scale microscopy of nanomaterials under industrially relevant conditions. *J. Microelectromechanical Syst.* **19**, 254–264 (2010).

24. Allard, L. F. *et al.* A new MEMS-based system for ultra-high-resolution imaging at elevated temperatures. *Microsc. Res. Tech.* **72**, 208–215 (2009).

25. Allard, L. F. *et al.* Novel MEMS-based gas-cell/heating specimen holder provides advanced imaging capabilities for in situ reaction studies. *Microsc. Microanal.* **18**, 656–666 (2012).

26. Hansen, P. L. *et al.* Atom-Resolved Imaging of Dynamic Shape Changes in Supported Copper Nanocrystals Atom-Resolved Imaging of Dynamic Shape Changes in Supported Copper Nanocrystals. *Science (80-.).* **295**, 2053–2055 (2002).

27. Allard, L. F. *et al.* Novel MEMS-based gas-cell/heating specimen holder provides advanced imaging capabilities for in situ reaction studies. *Microsc. Microanal.* **18**, 656–666 (2012).

28. Kamino, T. & Saka, H. A newly developed high resolution hot stage and its application to materials characterization. *Microsc. Microanal. Microstruct.* **4**, 127–135 (1993).

29. Kamino, T. *et al.* Development of a gas injection/specimen heating holder for use with transmission electron microscope. *J. Electron Microsc. (Tokyo).* **54**, 497–503 (2005).

30. Kamino, T., Yaguchi, T., Sato, T. & Hashimoto, T. Development of a technique for high resolution electron microscopic observation of nano-materials at elevated temperatures. *J. Electron Microsc. (Tokyo).* **54**, 505–508 (2005).

31. Liu, H. Ammonia synthesis catalyst 100 years: Practice, enlightenment and challenge. *Chinese J. Catal.* **35**, 1619–1640 (2014).

32. Masliuk, L., Swoboda, M., Algara-Siller, G., Schlögl, R. & Lunkenbein, T. A quasi in

situ TEM grid reactor for decoupling catalytic gas phase reactions and analysis. *Ultramicroscopy* **195**, 121–128 (2018).

33. Yokosawa, T., Alan, T., Pandraud, G., Dam, B. & Zandbergen, H. In-situ TEM on (de)hydrogenation of Pd at 0.5–4.5bar hydrogen pressure and 20–400°C. *Ultramicroscopy* **112**, 47–52 (2012).

34. Creemer, J. F. *et al.* An all-in-one nanoreactor for high-resolution microscopy on nanomaterials at high pressures. in *2011 IEEE 24th International Conference on Micro Electro Mechanical Systems* 1103–1106 (2011).

35. Zhu, Y. & Browning, N. D. The Role of Gas in Determining Image Quality and Resolution During In Situ Scanning Transmission Electron Microscopy Experiments. *ChemCatChem* **9**, 3478–3485 (2017).

36. Hansen, T. W. & Wagner, J. B. Environmental Transmission Electron Microscopy in an Aberration-Corrected Environment. *Microsc. Microanal.* **18**, 684–690 (2012).

37. de Jonge, N. Theory of the spatial resolution of (scanning) transmission electron microscopy in liquid water or ice layers. *Ultramicroscopy* **187**, 113–125 (2018).

38. Hu, J., Vanacore, G. M., Yang, Z., Miao, X. & Zewail, A. H. Transient Structures and Possible Limits of Data Recording in Phase-Change Materials. *ACS Nano* **9**, 6728–6737 (2015).

39. Schlögl, R. Heterogeneous Catalysis. *Angew. Chemie Int. Ed.* **54**, 3465–3520 (2015).

40. Feist, A. *et al.* Ultrafast transmission electron microscopy using a laser-driven field emitter: Femtosecond resolution with a high coherence electron beam. *Ultramicroscopy* **176**, 63–73 (2017).

41. Zaluzec, N. J., Burke, M. G., Haigh, S. J. & Kulzick, M. A. X-ray energy-dispersive spectrometry during in situ liquid cell studies using an analytical electron microscope. *Microsc. Microanal.* **20**, 323–329 (2014).

42. Prestat, E. *et al.* In Situ Industrial Bimetallic Catalyst Characterization using Scanning Transmission Electron Microscopy and X-ray Absorption Spectroscopy at One Atmosphere and Elevated Temperature. *ChemPhysChem* **18**, 2151–2156 (2017).

43. Crozier, P. A. Nanocharacterization of Heterogeneous Catalysts by Ex Situ and In Situ STEM. in *Scanning Transmission Electron Microscopy: Imaging and Analysis* (eds. Pennycook, S. J. & Nellist, P. D.) 537–582 (Springer New York, 2011).

44. Unocic, K. *et al.* Practical Aspects of Performing Quantitive EELS Measurements of Gas Compositions in Closed-Cell Gas Reaction S / TEM. *Microsc. Microanal.* **27**, 796–798 (2021).

45. Vendelbo, S. B. *et al.* Visualization of oscillatory behaviour of Pt nanoparticles catalysing CO oxidation. *Nat. Mater.* **13**, 884–890 (2014).

46. Avanesian, T. *et al.* Quantitative and Atomic-Scale View of CO-Induced Pt Nanoparticle Surface Reconstruction at Saturation Coverage via DFT Calculations Coupled with in Situ TEM and IR. *J. Am. Chem. Soc.* **139**, 4551–4558 (2017).

47. Tan, S. F. *et al.* Real-Time Imaging of Nanoscale Redox Reactions over Bimetallic Nanoparticles. *Adv. Funct. Mater.* **29**, 1903242 (2019).

48. Altantzis, T. *et al.* Three-Dimensional Quantification of the Facet Evolution of Pt Nanoparticles in a Variable Gaseous Environment. *Nano Lett.* **19**, 477–481 (2019).

49. Plodinec, M., Nerl, H. C., Girgsdies, F., Schlögl, R. & Lunkenbein, T. Insights into Chemical Dynamics and Their Impact on the Reactivity of Pt Nanoparticles during CO Oxidation by Operando TEM. *ACS Catal.* **10**, 3183–3193 (2020).

50. Resasco, J., Dai, S., Graham, G., Pan, X. & Christopher, P. Combining In-Situ Transmission Electron Microscopy and Infrared Spectroscopy for Understanding Dynamic and Atomic-Scale Features of Supported Metal Catalysts. *J. Phys. Chem. C* **122**, 25143–25157 (2018).

51. Xu, M. *et al.* Insights into Interfacial Synergistic Catalysis over Ni@TiO2–x Catalyst toward Water–Gas Shift Reaction. *J. Am. Chem. Soc.* **140**, 11241–11251 (2018).

52. Bremmer, G. M. *et al.* In situ TEM observation of the Boudouard reaction: multi-layered graphene formation from CO on cobalt nanoparticles at atmospheric pressure. *Faraday Discuss.* **197**, 337–351 (2017).

53. Dembélé, K. *et al.* Operando Electron Microscopy Study of Cobalt-based Fischer-Tropsch Nanocatalysts. *ChemCatChem* **13**, 1920–1930 (2021).

54. Dai, S., Zhang, S., Katz, M. B., Graham, G. W. & Pan, X. In Situ Observation of Rh-CaTiO3 Catalysts during Reduction and Oxidation Treatments by Transmission Electron Microscopy. *ACS Catal.* **7**, 1579–1582 (2017).

55. Dai, S. *et al.* In situ atomic-scale observation of oxygen-driven core-shell formation in Pt3Co nanoparticles. *Nat. Commun.* **8**, 204 (2017).

56. Song, B. *et al.* In Situ Oxidation Studies of High-Entropy Alloy Nanoparticles. *ACS Nano* **14**, 15131–15143 (2020).

57. Song, B. *et al.* Revealing high-temperature reduction dynamics of high-entropy alloy nanoparticles via in situ transmission electron microscopy. *Nano Lett.* **21**, 1742–1748 (2021).

58. Freund, H.-J., Meijer, G., Scheffler, M., Schlögl, R. & Wolf, M. CO Oxidation as a Prototypical Reaction for Heterogeneous Processes. *Angew. Chemie Int. Ed.* **50**, 10064–10094 (2011).

59. Newton, M. A., Belver-Coldeira, C., Martínez-Arias, A. & Fernández-García, M. Dynamic in situ observation of rapid size and shape change of supported Pd nanoparticles during CO/NO cycling. *Nat. Mater.* **6**, 528–532 (2007).

60. Huang, T.-J. & Tsai, D.-H. CO Oxidation Behavior of Copper and Copper Oxides. *Catal. Letters* **87**, 173–178 (2003).

61. Sharna, S. *et al.* In situ STEM study on the morphological evolution of copper-based nanoparticles during high-temperature redox reactions. *Nanoscale* **13**, 9747–9756 (2021).

62. Xin, H. L., Niu, K., Alsem, D. H. & Zheng, H. In situ TEM study of catalytic nanoparticle reactions in atmospheric pressure gas environment. *Microsc. Microanal.* **19**, 1558–1568 (2013).

63. Borg, Ø. *et al.* Fischer–Tropsch synthesis: Cobalt particle size and support effects on intrinsic activity and product distribution. *J. Catal.* **259**, 161–164 (2008).

64. Fu, Q., Saltsburg, H. & Flytzani-Stephanopoulos, M. Active Nonmetallic Au and Pt Species on Ceria-Based Water-Gas Shift Catalysts. *Science (80-.).* **301**, 935–938 (2003).

65. Rodriguez, A. J. *et al.* Activity of CeOx and TiOx Nanoparticles Grown on Au(111) in the Water-Gas Shift Reaction. *Science (80-.).* **318**, 1757–1760 (2007).

66. Campbell, C. T. Electronic perturbations. *Nat. Chem.* **4**, 597–598 (2012).

67. Xu, M. *et al.* TiO2–x-Modified Ni Nanocatalyst with Tunable Metal–Support Interaction for Water–Gas Shift Reaction. *ACS Catal.* **7**, 7600–7609 (2017).

68. van Steen, E., Claeys, M., Möller, K. P. & Nabaho, D. Comparing a cobalt-based catalyst with iron-based catalysts for the Fischer-Tropsch XTL-process operating at high conversion. *Appl. Catal. A Gen.* **549**, 51–59 (2018).

69. Campbell, G. A. The cobalt market revisited. *Miner. Econ.* **33**, 21–28 (2020).

70. Ghosh Chaudhuri, R. & Paria, S. Core/Shell Nanoparticles: Classes, Properties, Synthesis Mechanisms, Characterization, and Applications. *Chem. Rev.* **112**, 2373–2433 (2012).

71. Govender, A. *et al.* Morphological and compositional changes of MFe2O4@Co3O4 (M = Ni, Zn) core-shell nanoparticles after mild reduction. *Mater. Charact.* **155**,

109806 (2019).

72. Moodley, D. *et al.* Sintering of cobalt during FTS: Insights from industrial and model systems. *Catal. Today* **342**, 59–70 (2020).

73. Chen, C. *et al.* Highly Crystalline Multimetallic Nanoframes with Three-Dimensional Electrocatalytic Surfaces. *Science (80-.).* **343**, 1339–1343 (2014).

74. Wang, D. *et al.* Structurally ordered intermetallic platinum–cobalt core–shell nanoparticles with enhanced activity and stability as oxygen reduction electrocatalysts. *Nat. Mater.* **12**, 81–87 (2013).

75. Xiong, L. & Manthiram, A. Influence of atomic ordering on the electrocatalytic activity of Pt–Co alloys in alkaline electrolyte and proton exchange membrane fuel cells. *J. Mater. Chem.* **14**, 1454–1460 (2004).

76. Nishihata, Y. *et al.* Self-regeneration of a Pd-perovskite catalyst for automotive emissions control. *Nature* **418**, 164–167 (2002).

77. Zhang, S. *et al.* New Atomic-Scale Insight into Self-Regeneration of Pt-CaTiO3 Catalysts: Incipient Redox-Induced Structures Revealed by a Small-Angle Tilting STEM Technique. *J. Phys. Chem. C* **121**, 17348–17353 (2017).

78. Nakayama, H., Nagata, M., Abe, H. & Shimizu, Y. In Situ TEM Study of Rh Particle Sintering for Three-Way Catalysts in High Temperatures. *Catalysts* **11**, 19 (2021).

79. Yonggang, Y. *et al.* Carbothermal shock synthesis of high-entropy-alloy nanoparticles. *Science (80-.).* **359**, 1489–1494 (2018).

80. Chen, J. *et al.* Effect of Zr content on microstructure and mechanical properties of AlCoCrFeNi high entropy alloy. *Mater. Des.* **94**, 39–44 (2016).

81. Senkov, O. N. *et al.* Microstructure and elevated temperature properties of a refractory TaNbHfZrTi alloy. *J. Mater. Sci.* **47**, 4062–4074 (2012).

82. Kumar, N. *et al.* Understanding effect of 3.5 wt.% NaCl on the corrosion of

Al0.1CoCrFeNi high-entropy alloy. *J. Nucl. Mater.* **495**, 154–163 (2017).

83. Karlsson, D. *et al.* Structure and Hydrogenation Properties of a HfNbTiVZr High-Entropy Alloy. *Inorg. Chem.* **57**, 2103–2110 (2018).

84. Zhang, G. *et al.* High entropy alloy as a highly active and stable electrocatalyst for hydrogen evolution reaction. *Electrochim. Acta* **279**, 19–23 (2018).

85. Unocic, K. A. *et al.* Introducing and Controlling Water Vapor in Closed-Cell In Situ Electron Microscopy Gas Reactions. *Microsc. Microanal.* **26**, 229–239 (2020).

86. Bare, S. R., Yang, N., Kelly, S. D., Mickelson, G. E. & Modica, F. S. Design and operation of a high pressure reaction cell for in situ X-ray absorption spectroscopy. *Catal. Today* **126**, 18–26 (2007).

87. Topsøe, H. Developments in operando studies and in situ characterization of heterogeneous catalysts. *J. Catal.* **216**, 155–164 (2003).

88. Kelly, D. J. *et al.* Nanometer Resolution Elemental Mapping in Graphene-Based TEM Liquid Cells. *Nano Lett.* **18**, 1168–1174 (2018).

Chapter 5

Effect of Manganese on the Activation of Cobalt-based Fischer-Tropsch Catalysts via *In Situ* Gas Cell Scanning Transmission Electron Microscopy

The work in this chapter details the characterisation of cobalt-based, titania-supported Fischer-Tropsch (FT) catalysts with increasing manganese content. The addition of Mn to Co FT catalysts has shown to shift product synthesis towards oxygenate and olefin selectivity.[1] Previous reports on similar catalysts have reported on increased cobalt dispersions post-calcination as a function of increasing manganese inclusion, leading to a relative decrease in particle size upon reduction.[2] The catalysts used in this study involved co-impregnation of a mixed Co/Mn precursor solution, which led to significantly increased dispersion compared to the unpromoted counterpart. *In situ* gas cell scanning transmission electron microscopy (STEM) in combination with energy dispersive X-ray spectroscopy (EDS) has demonstrated the dynamic morphological changes the catalyst undergoes during an industrially relevant H_2 reduction treatment. The increased Co dispersion induced by Mn during impregnation leads to much smaller Co particle formation on reduction relative to the catalysts with no Mn present, with evidence suggesting an increased stability towards sintering/coalescence effects.

This manuscript was drafted by M. Lindley, with contributions from P. Stishenko, and edits from S. J. Haigh and A. J. Logsdail. Catalyst synthesis was performed industrially and provided by J. Paterson. STEM-EDS/EELS sample preparation, experimental acquisition, data analysis/processing and particle size analysis was performed by M. Lindley. DFT calculations were performed by P. Stishenko, J. W. M. Crawley and A. J. Logsdail. Catalytic reaction testing, TPR and XAS was acquired industrially and provided by J. Paterson, with addition processing performed by M. Lindley. All authors contributed to discussions regarding experimental objectives. This manuscript has not yet been submitted.

Effect of Manganese on the Activation of Cobalt-based Fischer-Tropsch Catalysts via *In Situ* Gas Cell Scanning Transmission Electron Microscopy

Matthew Lindley[1], Pavel Stishenko[2], James W. M. Crawley[2], James Paterson[3], Chris Hardacre[4], Andrew J. Logsdail[2], Sarah J. Haigh[1]

[1] Department of Materials, University of Manchester, Oxford Road, Manchester, M13 9PL, United Kingdom

[2] Cardiff Catalysis Institute, School of Chemistry, Cardiff University, Park Place, Cardiff, CF10 3AT, Wales, United Kingdom

[3] BP, Saltend Chemicals Park, Hull, HU12 8DS, United Kingdom

[4] Department of Chemical Engineering and Analytical Science, University of Manchester, Oxford Road, Manchester, M13 9PL, United Kingdom

Abstract

While Fischer-Tropsch (FT) synthesis offers a clean route to conversion of syngas (CO/H_2) into hydrocarbon fuels, modifications of traditional Co/TiO_2 based FT catalysts with Mn exhibit a selectivity shift towards commercially desirable long-chain alcohols and olefins. A close proximity association between the Co and Mn has been established to account for the change in catalyst functionality, however, little work has been reported to demonstrate how this relationship changes during typical industrial processes. In this work, *in situ* gas cell scanning transmission electron microscopy (STEM) has been used in combination with energy-dispersive X-ray spectroscopy (EDS) to investigate the morphological change of $CoMn/TiO_2$ catalysts during a H_2 activation process, used industrially to reduce the Co oxide to the catalytically active metallic state.

Introduction

Fischer-Tropsch (FT) synthesis is a heterogeneous catalytic process that converts syngas (CO/H_2) into high quality liquid hydrocarbons and is an attractive route to produce clean fuels and value-added chemicals from non-fossil fuel derived feedstocks.[3] Recent interest in FT has been driven by increasingly efficient catalyst design and the development of new gas to liquid (GTL) technologies. The traditional method for FT synthesis is to flow syngas over a metallic catalyst within a fixed-bed reactor. The synthesis process can take place on several transition metals[4], but the desire for high activity, selectivity, and stability makes cobalt-based catalysts the practical choice for the production of high molecular weight paraffins.[3] Co particle size is a key factor in FT performance, and a diameter of 8-10 nm is the optimum; with larger particles, the reduction in active surface area relative to total Co loading leads to reduced activity, whilst for smaller particles there are a larger number of edge sites, which favour chain termination and the formation of methane.[5,6] Industrial FT processes rely on supported nanoparticle systems synthesised via wet impregnation.[7] The support is typically a metal oxide such as titania, silica or alumina in the form of a nanoparticle powder, providing the catalytic material with mechanical integrity for the extruded pellets within the reactor, as well as encouraging good dispersion and hindering metal particle agglomeration.[8]

The addition of elements such as Mn, Re, or Zr can improve dispersion of the Co FT catalysts[9], enhancing Co reducibility and catalytic activity[9,10], as well as decreasing the reaction selectivity to undesirable methane.[11] Recent studies on Co/TiO_2 catalysts demonstrated that addition of Mn can modify the FT reaction selectivity towards long-chain oxygenates and liquid petroleum gas (LPG, C_2-C_4).[12,13] The selectivity shift is suggested to result from an MnO-induced increase of cobalt carbide, which inhibits CO dissociation and instead favours CO insertion.[13] Physical mixtures of Co-only and Mn-only catalysts have not shown similar catalytic behaviour, indicating that Mn-Co interactions are key to the differences in FT functionality[1]; however, the detail of such interactions has remained elusive, with the oxygen sensitivity of the Co nanoparticles making any investigation of the evolution of the Mn-Co distribution *ex situ* very challenging. X-ray photoelectron spectroscopy and X-ray absorption spectroscopy studies of the as produced, calcined material show that the presence of Mn significantly increases the Co distribution in wet impregnated samples, with bulk structural data suggesting the formation of a mixed metal oxide spinel.[14,15] A pre-treatment is then required to reduce the metal oxide and form the cobalt metal (Co^0) catalyst[7], which is the active site for FT synthesis. However, high resolution characterisation of the reduced catalytic material remains lacking in the literature.

Atomic-level structural and chemical characterisation of nanoparticle catalysts can be achieved via scanning transmission electron microscopy (STEM). Conventional STEM imaging requires a high vacuum environment, however, this is detrimental for investigations of heterogeneous catalysts where adsorbate-induced surface reconstructions can lead to dynamic structural changes depending on the environmental conditions.[16,17] For nanoparticle catalysts, changes in morphology in response to varying gas species and concentration can also occur.[18] *In situ* STEM investigations can now be performed at elevated pressures (typically up to 1 bar) and temperatures (up to 1000°C) using *in situ* gas cell holders.[19,20] These conditions are realised by the use of ultra-thin, electron-transparent silicon nitride membranes that separate the reactive gas environment from the STEM vacuum, with a local heating element allowing temperature control. Here, we apply these approaches to perform element-sensitive *in situ* STEM imaging, combined with catalytic reaction testing, to investigate the evolution of wet impregnation synthesised $CoMn/TiO_2$ catalysts during the pre-treatment reduction step for a range of elevated temperatures (150-350°C). Our results are complemented by density functional theory (DFT) simulations, and demonstrate the dispersive behaviour induced by Mn.

Investigating Catalyst Dispersion via Energy Dispersive X-ray Spectroscopy

The atomic number dependency (*Z*-contrast) observed in high-angle annular dark field (HAADF) STEM imaging has led to widespread use of the technique for studying the size and morphology of supported catalytic nanoparticles, where the high atomic number of the metal catalyst is in contrast to the lighter support (e.g. silica[21] or alumina[22]). For supports comprised of heavier elements, the contrast with metal catalysts can be diminished, and the similarity of the atomic numbers for Co (Z=27), Mn (Z=25) and Ti (Z=22) in the CoMn/TiO_2 system makes distinguishing the metal nanoparticles from the TiO_2 support particularly challenging for HAADF STEM. Similarly, separately identifying the Co and Mn dispersion is impossible without additional direct analytical methods. In this report, simultaneous elemental and chemical information during STEM is pursued to provide spatially resolved Co and Mn distributions via energy dispersive X-ray spectroscopy (EDS) and an averaged oxidation state of the Co and Mn via electron energy loss spectroscopy (EELS).

HAADF STEM images and corresponding EDS elemental maps are compared in **Figure 5.1** for the 10 wt% Co/TiO_2 catalyst, both without (**Figure 5.1a)** and with (**Figure 5.1b**) 5 wt% Mn, prior to any reduction. The Mn wt% loading was informed by the high selectivity towards long-chain alcohol for these samples, as revealed by catalytic testing and supporting TPR/XAS data, which revealed a slightly lower temperature for catalyst reduction, albeit at a cost of a smaller fraction of reduced Co metal (see SI section 2). The HAADF STEM images in **Figure 5.1** show aggregated clusters of the TiO_2 support, with individual TiO_2 particle diameters of 10-30 nm. As expected, the HAADF STEM images do not indicate the Co or Mn distributions, which are only readily visible via the STEM EDS Co or Mn elemental maps (shown in blue and red, respectively). The EDS maps highlight the dramatic differences in the Co distributions for the freshly calcined catalysts as a result of Mn inclusion. For the unpromoted specimen (**Figure 5.1a**), the Co forms irregular-shaped porous structures, typically 20-100 nm in diameter, which are much larger than the individual titania particles; in contrast, the Co is more uniformly dispersed across the support surface in the Mn promoted specimen (**Figure 5.1b**). The STEM EDS maps also exhibit the co-location of Co and Mn, seen previously for similarly prepared mixed-solution wet impregnated catalysts.[13,23]

An *ex situ* heat treatment was applied to the Co/TiO_2 and CoMn/TiO_2 catalysts to investigate how the morphology changes in an industrially relevant reduction process (1 bar H_2/300°C). *Ex situ* reduction of the unpromoted Co/TiO_2 catalyst for 3 hrs results in Co

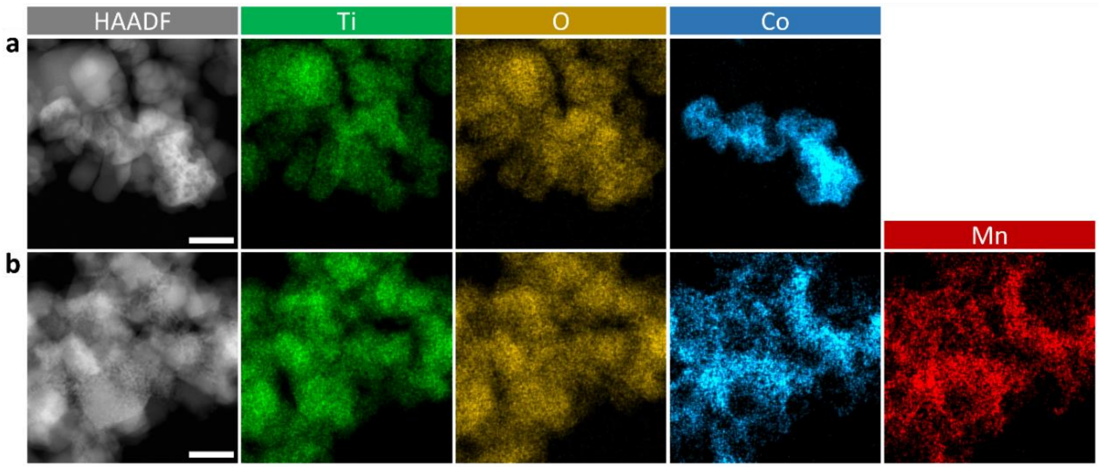

Figure 5.1: HAADF-STEM and STEM-EDS elemental mapping of the TiO_2 supported Co/Mn distribution after calcination (prior to reduction). ***(a)*** *10 wt% Co/TiO_2 catalyst (without Mn).* ***(b)*** *10 wt% Co-5wt% Mn/TiO_2 catalyst. STEM-EDS maps are presented in green, yellow, blue, and red for Ti, O, Co, and Mn. Scale bars: 30nm.*

clusters that still contain remnants of the porous features seen in the fresh calcined sample (**SI Figure 5.11b**), whereas reduction for 12 hrs leads to complete densification and formation of Co particles with approximately spherical geometry and a mean diameter of ~17 nm (**SI Figure 5.11c**). A more detailed comparison of the Co and O STEM EDS maps in **SI Figure 5.11c** reveals that the reduced Co particles display a core-shell structure; the outer shell is associated with an oxygen rich layer and has a thickness of ~3 nm. A vacuum holder was used to minimise air exposure for the catalysts when transferring from the *ex situ* reduction heat treatment to the STEM vacuum, but the observation of an outer shell with differing composition to the core suggests that air exposure occurred noneltheless. The observed outer shell modifies the particle diameter and creates challenges for accurate size analysis, motivating the need for *in situ* STEM elemental analysis to help understand the evolution of the Co nanoparticles during the reduction-step of the catalyst synthesis.

For the CoMn/TiO_2 catalyst, the reduction treatment (12 hrs) results in the uniform distribution of Co converting to Co nanoparticles that are smaller than those in the absence of Mn, with a mean diameter of ~11 nm (**SI Figure 5.10b,d**,). However, it is noted that the edges of the nanoparticles are poorly defined for the promoted catalyst, which makes absolute size analysis challenging. Interestingly, the reduction treatment does not result in significant change to the Mn distribution that correlate with the Co nanoparticle distribution, with the Mn remaining uniformly distributed on the TiO_2 support. The stable distribution of Mn, when compared to the formation of dense Co particles, demonstrates that the Co and Mn segregate during the reduction treatment.

Determining Oxidation States via Electron Energy Loss Spectroscopy

Complementary to STEM-EDS, STEM-EELS was used to determine the change in oxidation state for Co and Mn in samples pre- and post- the *ex situ* reduction treatment. The relative intensities of the Co and Mn L_2 and L_3 STEM-EELS edges for both the catalyst precursor (i.e., pre-reduction) and fresh (i.e., post-reduction) catalysts were compared to Co and Mn oxide/metallic standards. Pre-reduction, the Co/TiO_2 catalyst has a good match to

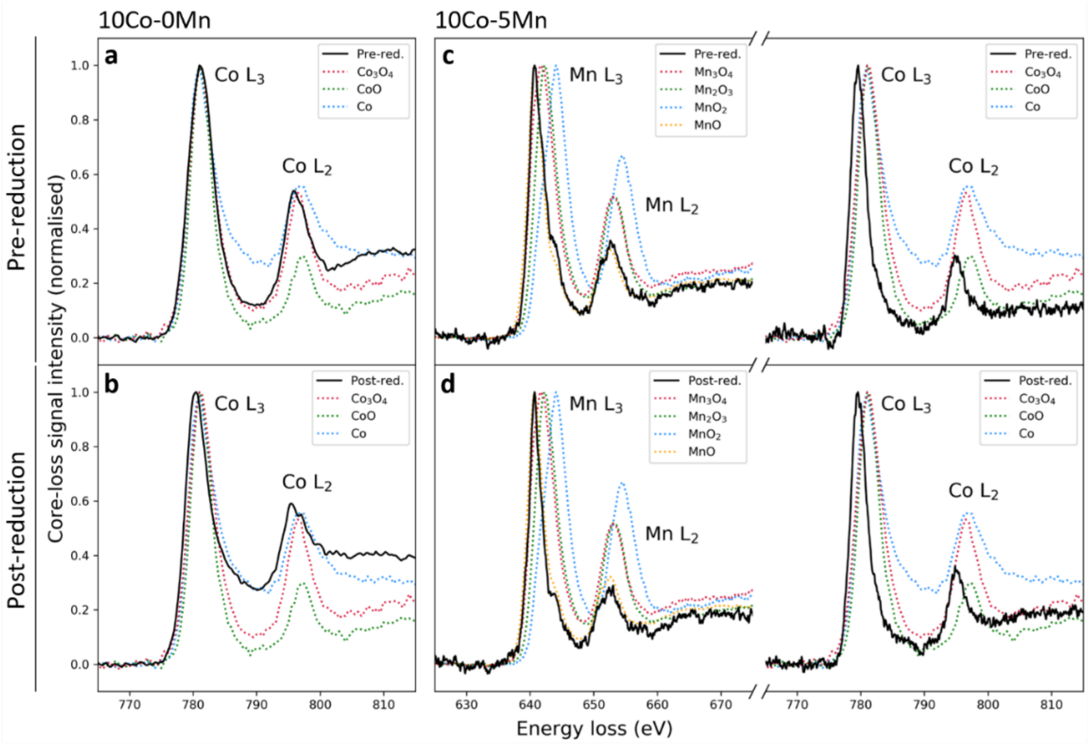

Figure 5.2: STEM-EELS analysis of the Co/Mn oxidation states. (a,b) *10 wt% Co/TiO$_2$ and* ***(c,d)*** *10 wt% Co-5 wt% Mn/TiO$_2$ catalysts pre- and post- ex situ reduction heat treatment, respectively, in H$_2$ (1 bar, 12hrs at 300°C). Summed STEM-EELS spectra from the catalysts (black) are compared to the measured spectra for the Co and Mn standards (dotted lines, legend provided on each spectrum).*

Co_3O_4 (**Figure 5.2a**), and the reduced sample has a best fit to metallic Co (**Figure 5.2b**). The observation of Co^0 is consistent with *in situ* X-ray absorption near edge fine structure (XANES) measurements, which show the content of metallic Co to be 98.3% after exposure to H_2 at 300°C for 12 hrs (**SI, Figure 5.9a and Table 1**).

For the CoMn/TiO_2 catalyst, the Co peaks from the fresh sample align closely to the CoO reference rather than Co_3O_4 (**Figure 5.2c**). For the Co/TiO_2 catalyst, a spinel structure, with general formula of AB_2O_4, is postulated with Co residing in both the tetrahedral (A) and octahedral (B) positions in the unit cell (i.e., $CoCo_2O_4$); here, the presence of CoO supports a postulate that Mn is introduced into the structure during catalyst preparation, which results in the formation of a mixed oxide spinel (i.e., $Co_{2-x}Mn_xO_4$). When the CoMn/TiO_2 catalyst is reduced, the Co peaks remain unchanged and continue to align with the CoO reference (**Figure 5.2d**). Due to the small particle size and high distribution of Co after the reduction treatment, it is possible that oxidation occurs during atmospheric exposure when transferring to the microscope (i.e., there is a lower bulk Co metal to surface Co oxide ratio, and hence CoO dominates the spectra). The spectral peaks for Mn remain closely matched to the reference for MnO both pre- and post-reduction, which is a result that could not be determined from prior observations using X-ray diffraction (XRD) due to the high Mn dispersion.[1]

Observing Morphology Changes during *In Situ* Reduction Treatment

In situ HAADF-STEM and STEM-EDS analysis was used to observe and compare the catalysts during a reduction treatment similar to that used *ex situ*, with the results presented in **Figure 5.3**. STEM-EDS elemental mapping was performed at 150-350°C, with the mapping at room temperature infeasible due to the build-up of contamination at this temperature, which interferes with imaging (**SI Figure 5.12**). For the Co/TiO_2 catalyst, HAADF-STEM images show a reduction of volume and porosity for the Co material on heating at 150°C (**SI Figure 5.13** for HAADF-STEM imaging at room temperature). Previous *in situ* XRD measurements report cobalt oxide crystallites with a diameter on the order of 10 nm for the pre-reduced material.[24] Sintering is observed at 250°C and 350°C (**Figure 5.3a**) with the Co forming

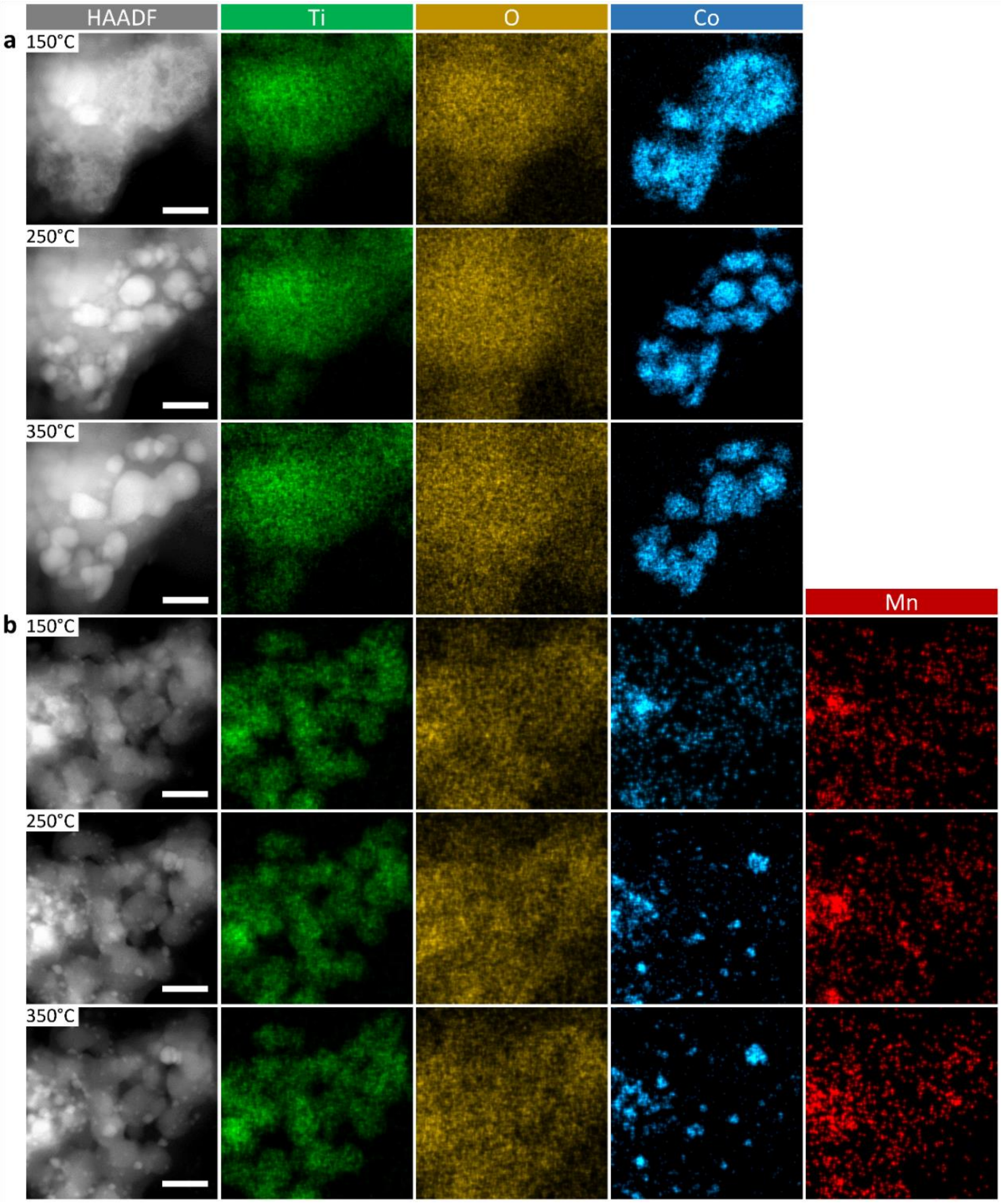

Figure 5.3: In situ HAADF-STEM and STEM-EDS elemental mapping as a function of temperature during reduction in H_2. ***(a)*** *10 wt% Co/TiO_2 catalyst (without Mn) and* ***(b)*** *10 wt% Co-5 wt% Mn/TiO_2 catalyst. HAADF STEM images at room temperature are presented for comparison in* ***SI Figure 5.13****. Colours are as described in Figure 1. Scale bars: 30nm.*

distinct particles with a mean diameter of 10.9±1.2 nm. Closer inspection reveals coalescence of the already formed Co particles, as well as the formation of new smaller particles (**SI Figure 5.13a**) that have possibly formed from residual Co that decorates the titania surface. The consequence is a bimodal distribution of particle sizes being observed, with a relative increase in standard deviation, σ, relative to that at 250°C (**SI Figure 5.14a**).

Comparison of the sintering behaviour for the CoMn/TiO_2 catalyst under identical conditions reveals evolution from a highly dispersed oxide morphology to formation of Co particulates during the *in situ* reduction treatment (**Figure 5.3b**). The HAADF-STEM images display minimal change between room temperature (**SI Figure S7b**) and 150°C (**Figure 5.3b**); however, distinct particles have formed by 250°C, with diameters of 3.4±1.6 nm. The remaining Co continues to sinter at 350°C, which leads to an increase in the number of distinct Co particles and a slight increase in the average particle size observed to 3.9±1.1 nm (**SI Figure 5.14b**). Interestingly, σ is the same at both 250°C and 350°C, which suggests that the Co particles in this catalyst are more resistant to sintering at high temperatures than that where Mn is not present, leading to an improved stability during the activation process.

Modelling Co/Mn Interaction using Density Functional Theory

To further understand the influence of the Mn on the distribution of Co across the TiO_2 support, DFT calculations were performed to determine the strength of the Co and Mn atomic interactions with the TiO_2 support. Calculations were performed considering metal atom coordination on the TiO_2 anatase (101) surface, chosen due to its high stability[25] and the prevalence of the anatase TiO_2 phase in Degussa P25 support, as used in our CoMn/TiO_2 catalysts.[26] To understand the surface interaction of Co and Mn, an extensive range of adsorption complexes were considered, with specific favourability observed towards the adsorption positions at various hollow and bridge sites between surface oxygen.

The adsorption complexes that result from our comprehensive geometry survey are shown for Co and Mn in **Figure 5.4**, along with relative energies. Atomic charges and preferred spin configurations are shown in **SI Table 2**. For both Co and Mn, we observe

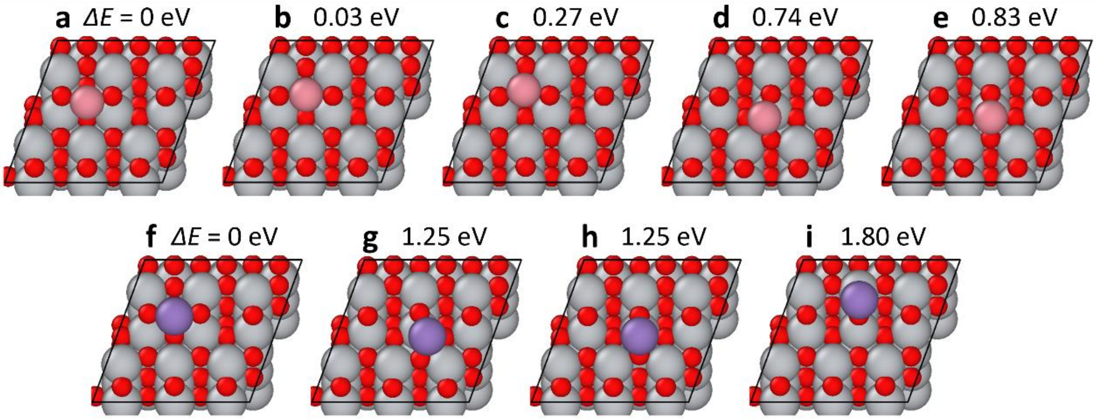

Figure 5.4*. *Most stable configurations for Co and Mn adatoms. *The lowest energy configurations for **(a-e)** Co atom and **(f-i)** Mn atom adsorbed on the TiO_2 anatase (101) surface. Full structural details are provided in **SI Table 2**. Colours for Co, Ti, and O are pink, grey, and red, respectively. Relative energies (ΔE) are given compared to the most stable configurations for Co (a) and Mn (f).*

a positive atomic charge, which indicates the favourability of oxidation states above zero. For the Co adatom, the five most stable adsorption positions have an energy range of 0.83 eV, with the preferred adsorption being with coordination to four oxygens, with metal-oxygen bond lengths ranging from 1.81-3.06 Å. The Co adsorption complexes in **Figure 5.4a** and **5.4b** are notably close in geometry and energy, yet clearly distinguishable by oxygen bonds lengths and distortion of the anatase lattice. In contrast, for the Mn adsorption complexes the four most stable structures have a large energy range over 1.80 eV; the difference between the most stable adsorption site in **Figure 5.4f** and the next most stable configuration in **Figure 5.4g** is 1.25 eV. The greater range of energies is indicative that the Mn atoms would be anchored more strongly to the anatase (101) surface than the Co, and less likely to sinter at elevated temperatures. For the most stable Mn adatom configuration, the four nearest oxygen atoms are at distances of 1.87-4.12 Å, which is similar to the most stable Co configuration.

For diatomic adsorption complexes, a similar approach was employed considering two-atom configurations but with adsorption considered favourable on available oxygen species at the TiO_2 surface, guided by observations for the monoatomic adsorption (see SI experimental method for details). The general chemical formula of the diatomic clusters is Co_xMn_{2-x}, where x ranges from 0 to 2; to determine the relative energies of the considered configurations, a convex hull has been constructed for x vs mixing energy, E_{mix}, which is defined as:

$$E_{\mathrm{mix}} = E_{\mathrm{tot}} - E_{\mathrm{Co}}\frac{x}{2} - \mathrm{E}_{\mathrm{Mn}}\frac{2-x}{2}$$

Here, E_{tot} is the total energy of the diatomic configuration, and E_{Co} and E_{Mn} correspond to the lowest energy configurations of the pure Co and Mn diatomic clusters, respectively. **Figure 5.5a** plots this mixing energy, with the mixed heteronuclear diatomic cluster demonstrating energetic preference over the homonuclear diatomic clusters. The most stable obtained pairwise configurations (with the lowest potential energy) are shown in **Figure 5.5b-d** showing that Co-Co and Co-Mn interactions are formed for these species, whilst Mn-Mn is most stable when distanced. In combination, one can postulate therefore that the distributed

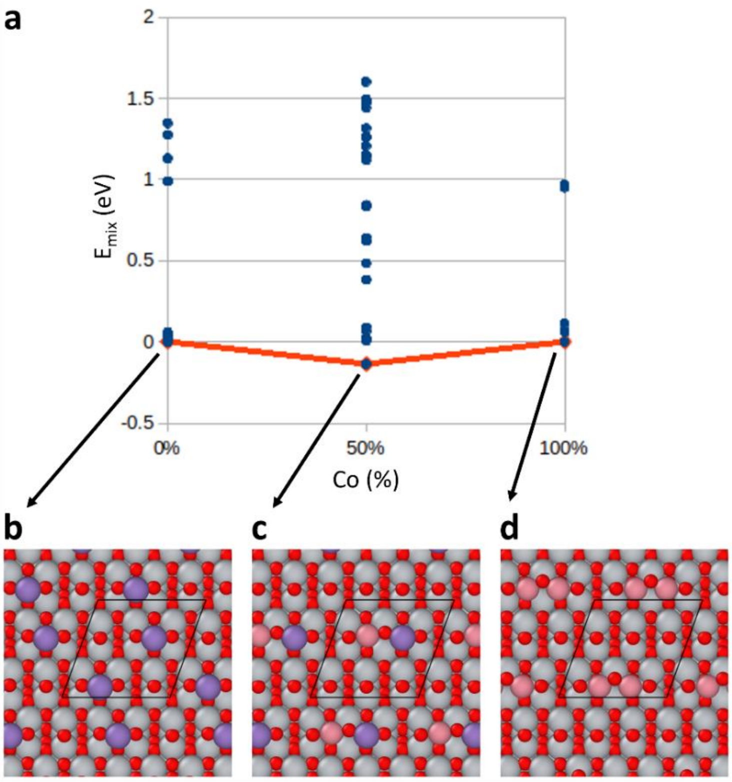

Figure 5.5*. Most stable configurations for diatomic Co and Mn clusters. (a)** *Plot of the mixing energy, E_{mix} against diatomic composition for Co_xMn_{2-x} clusters. E_{mix} of the most stable mixed CoMn cluster is –0.14 eV, i.e., more stable than the homonuclear diatomic clusters. Insets demonstrate the most stable configuration for* ***(b) *Mn_2,* ***(c)*** *CoMn, and* ***(d)*** *Co_2 on the anatase (101) TiO_2 surface. Colour scheme is as given in Figure 5.4.*

Mn surface atoms may act as anchors for Co atoms, without themselves favouring homogeneous surface clusters at small sizes.

Conclusions

In this work, HAADF-STEM with simultaneous STEM-EDS/EELS was used to investigate the morphology changes of a 10 wt% Co catalyst on TiO_2 support, both in the presence and absence of 5 wt% Mn, during an industrially relevant H_2 reduction treatment. Both catalysts were prepared via mixed solution wet impregnation, and *ex situ* observations of the freshly calcined catalysts reveal significant increase in the Co dispersion due to the presence of Mn. An *ex situ* reduction treatment of the catalysts leads to metallic Co particle formation, with the addition of Mn leading to a dramatic decrease in particle size and distribution range relative to the catalyst with no Mn present. To fully observe the activation process an *in situ* H_2 reduction treatment was applied using gas cell TEM, which provided qualitatively similar results to that of the *ex situ* treatment.

To provide fundamental insight into the behaviour of the Co and Mn species in the experimental synthesis and *in situ* characterisation, DFT calculations were performed with a focus on determining the favourability of Co and Mn mixing. DFT simulations show that both Co and Mn atoms favour binding with oxygen atoms at the (101) surface of anatase TiO_2, and greatest stability is when adsorbed in the hollow site with 3 or 4 oxygen atoms in the first coordination radius. For a Co adatom there are several less favourable, yet energetically accessible, sites. In contrast, for the Mn adatoms, the next energy minimum is 1.25 eV above the ground state, making surface migration of the Mn less likely than for Co. Both Co and Mn adatoms are positively charged, with population analysis showing that charge transfer is larger for Mn. For diatomic clusters, formation of Co-Co and Co-Mn pairs is energetically preferable, with the mixed diatomic cluster most stable, whilst Mn-Mn is unfavourable compared to the separated single atoms. In combination with the experimental results, it can be concluded that, for initial clustering, the Mn promoter may act as a surface anchoring point from which Co clusters can form, which leads to the experimental observation of smaller, more disperse clusters in the CoMn/TiO_2 system.

Experimental Section

A series of 5 catalysts were prepared from mixed solutions of cobalt nitrate hexahydrate and manganese acetate tetrahydrate precursors dissolved in water at 40°C. The solutions were incipient wetness co-impregnated onto a supporting titania (P25) powder to yield 10 wt% Co + (*n*) wt.% Mn/TiO_2 catalysts, where $n = 1, 2, 3, 5$ and 7.5. The resulting mixtures were extruded into pellets and calcined in air with a stepped heating profile (5 hrs at 60°C, 5 hrs at 120°C and 2 hrs at 300°C, with a heating rate of 10°C/min). Scanning transmission electron microscopy (STEM) with energy dispersive X-ray spectroscopy (EDS) and electron energy loss spectroscopy (EELS) was performed using a probe aberration-corrected FEI Titan G2 80-200 ChemiSTEM operated at 200 kV. *In situ* STEM analysis was performed using a Protochips Atmosphere gas cell system with H_2 at pressures up to 1 bar and temperatures of 150-350°C. Statistical and spectroscopic analysis was performed using Python packages (Numpy, Scipy and Hyperspy[27]). Full details of STEM experimental measurements, density functional theory (DFT), temperature programmed reduction (TPR) and complementary X-ray absorption spectroscopy (XAS) methods is available in SI Section 1.

Supporting Information

Effect of Manganese on the Activation of Cobalt-based Fischer-Tropsch Catalysts via In Situ Gas Cell Scanning Transmission Electron Microscopy

Matthew Lindley[1], Pavel Stishenko[2], James W. M. Crawley[2], James Paterson[3], Chris Hardacre[4], Andrew J. Logsdail[2], Sarah J. Haigh[1]

[1] Department of Materials, University of Manchester, Oxford Road, Manchester, M13 9PL, United Kingdom

[2] Cardiff Catalysis Institute, School of Chemistry, Cardiff University, Park Place, Cardiff, CF10 3AT, Wales, United Kingdom

[3] BP, Saltend Chemicals Park, Hull, HU12 8DS, United Kingdom

[4] Department of Chemical Engineering and Analytical Science, University of Manchester, Oxford Road, Manchester, M13 9PL, United Kingdom

Section 1: Experimental Methods

Temperature programmed reduction (TPR) analysis was conducted using a Quantachrome ChemBET Pulsar chemisorption analyzer. 100 mg of fresh calcined catalyst was loaded into the instrument and dried under flowing argon, heating from room temperature at a rate of 5°C min^{-1} to 110°C and dwelling for 15 min. The sample was then allowed to cool to room temperature before the reduction treatment, where gas flow was changed to 100% H_2 (60 mL min^{-1}) and temperature increased to 600°C (5°C min^{-1}). Once at temperature the sample was left to dwell for 30 mins to equilibrate and allow for full reduction of the cobalt oxide. H_2 content in the gas outlet was measured throughout the reduction procedure using an integrated thermal conductivity detector.

Preparing samples for microscopy involved grinding the calcined catalyst pellets were to a fine powder and dispersion in a methanol suspension for dropcasting onto the relevant TEM support. For *ex situ* analysis, the samples were deposited onto a lacey carbon copper grid and baked in vacuum at 100°C for 3 hours to aid in desorption of carbonaceous species, which may lead to contamination build up during electron beam exposure. For *in situ* analysis, the Protochips Atmosphere™ gas cell system was employed. The cell assembly incorporates two Si MEMS-fabricated chips, each containing a thin central membrane (300x300 µm), with the top membrane featuring six electron transparent SiN_x membrane windows (10 µm diameter, 30 nm thick). The top chip provides pre-calibrated heating to the sample via electrical contacts and is temperature controlled using proprietary software. The bottom chip membrane is 50 nm and contains 5 µm spacers which sit against the top chip to provide a separation through which gas can flow at up to 1 bar pressure.

Scanning transmission electron microscopy (STEM) and complementary analytical techniques were performed using an aberration-corrected FEI Titan G2 80-200 ChemiSTEM, located at the University of Manchester, operating at 200 keV and a beam current of 90 pA. This microscope is equipped with an FEI Super-X Quad Silicon Drift Detector with a collection angle of ≈0.7 sr, from which energy dispersive X-ray spectroscopy (EDS) data was acquired using the Bruker Esprit software package and post-processed using Esprit and

Python-based modules. High-angle annular dark field (HAADF) imaging was acquired using FEI TIA and Gatan DigitalMicrograph software. Electron energy loss spectroscopy was acquired using a GIF Quantum ER System (Gatan Inc.) with 0.1-0.5 eV/channel dispersion and dwell times of 0.1-0.2s to attain the core-loss acquisitions. Post-processing of EELS was performed using Python packages (Numpy, Scipy and Hyperspy).

Using the *in-situ* gas cell system to provide similar reduction conditions to that of the ex-situ treatment, temperature increments of 25, 150, 250 and 350°C were applied to the catalyst samples during exposure to 1 bar H_2. A dwell time of ~30 minutes at each temperature increase was implemented to allow the system to equilibrate before observation and at each stage, where the same region of interest was then subjected to a series of HAADF and EDS data acquisitions. To avoid potential low-temperature electron beam induced contamination effects, observed during previous experiments of under these conditions, electron-dose heavy EDS collection was omitted at this stage.

At relatively low temperatures (<200°C) contamination is a significant problem in analysing these materials using *in situ* STEM EDS/EELS. Deposition of carbonaceous material across the region of interest (ROI) during the electron beam scan leads to a mixture of low signal collected from the sample and increased signal from the contamination, which can overshadow the peaks of interest in the resulting spectrum. Figure S5 illustrates this occurrence at 150°C, in which a 'clouding' of the ROI leads to noisy spectrum data. Despite many attempts to prevent this occurrence, using techniques such as plasma cleaning and beam showering, this is a significant issue for low temperature gas cell analysis.

Catalyst modelling was performed using Density Functional Theory (DFT) as implemented in the FHI-aims software package.[28] The unpaired ground state electronic configuration of Co and Mn elements required the application of collinear spin calculations, with spin restrictions enforced where discussed. Relativistic effects were included via the zero order regular approximation (ZORA).[29] Due to an excellent ability to reproduce the bulk and surface properties of TiO2, and design around accurate surface adsorption chemistry, the mBEEF exchange-correlation density functional was used.[30] The standard *light* basis sets

(2010 version), as distributed with FHI-aims, were used to represent the electronic wavefunction. Convergence of the self-consistent field (SCF) cycle, unless stated otherwise, was deemed complete when the total energy changed by less than 10^{-6} eV between iterations.

For the surface geometries of anatase (101) TiO_2, it was necessary to create a supercell with surface dimensions of 3x2 unit cells, and depth of 2 unit cells (i.e., 4 Ti layers). A converged **k**-grid of 3x3x1 was applied for all calculations therein, with no sampling in the z-direction due to the finite nature of the slab model. For subsequent geometry optimisations, the bottom unit cell layer of the slab model was fixed, and a dipole correction included to prevent spurious electrostatic effects from applying a one-sided model. Geometry optimisations were deemed complete when the maximum force on any atom was below a threshold of 0.01 eV/Å.

To understand the interaction of Co and Mn atoms with the anatase (101) surface, we have identified adsorption complexes constituted by these adatoms. As bonding to O species is preferred for metal atom adsorption, a set of adsorption complexes was generated by placing metal adatoms on top, on bridges, and in hollows between surface oxygen atoms. There are three unique surface oxygen atoms on the anatase (101) surface unit cell (**Figure 5.6**). 12 unique sites were selected (3 atop, 6 bridges, 3 hollows). Therefore, 24 initial configurations were built (12 sites for each metal). To build initial configurations of two-atom clusters only atop sites were used to avoid trapping in local energy minima. All pairwise configurations with distance between adsorbate atoms up to 6 Å were enumerated. Then, after first geometry optimization stage, all homotopic combinations of each optimized cluster were added to the pool of clusters. For example, for each Co-Co cluster we added Co-Mn, Mn-Co, and Mn-Mn clusters with the same atomic coordinates. Subsequently, the geometry optimization was performed on the extended pool of clusters. The SuSMoST package was employed for enumeration of single-atom adsorption sites as well as two-atom clusters, considering only symmetry inequivalent configurations to save computational resources.[31]

To avoid adatoms becoming trapped at saddle points during optimisation, minor random displacements were introduced using the ASE (Atomic Simulation Environment) rattle functionality. Due to challenges with convergence of the SCF cycles, and to minimise computational cost, a multi-step approach was then taken to geometry optimisation: initially coarse relaxation and DFT settings. Firstly, an optimisation was performed with the PBE exchange-correlation density functional, using a spin-paired configuration and coarse convergence criteria of changes in density below 5 x 10^{-4} e for the SCF cycle, and forces below 0.05 eV/ Å for geometry optimisation; this allowed identification of the possible stable positions of the metal adatoms, from which structures were further optimised with higher accuracy, spin-unpaired approach as highlighted above. Free atom's unpaired spin configurations were used as initial for each structure: 3 for Co, and 5 for Mn.

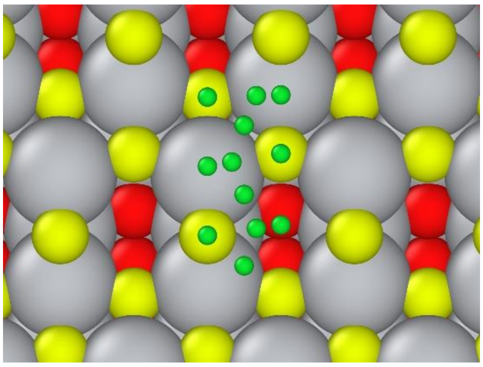

Figure 5.6. Unique sites tested for adsorption complexes. *Surface oxygen atoms (yellow) on anatase (101) surface. Small green spheres showing adsorption sites for metal ions. Other oxygen atoms are presented in red, and titanium atoms are grey.*

Section 2: Results and Discussion

Figure 5.7 shows the results of catalyst testing. The activity (CO conversion) and methane selectivity of the catalysts remains relatively constant across the range of Mn loadings tested (**Figure 5.7a**). However, an increase in C_2-C_4 products is observed between 1-2% Mn, which then remains steady at higher loadings. This selectivity shift is at the expense of the more traditionally target C_{5+} products. **Figure 5.7b** shows that, of the C_{5+} products which remain, the affinity towards long chain alcohols is significantly enhanced with increased Mn loading up until 5% Mn. However, a downturn in this yield was observed at 7.5% Mn, suggesting the alcohol yield peak is present between 3-7.5% Mn.

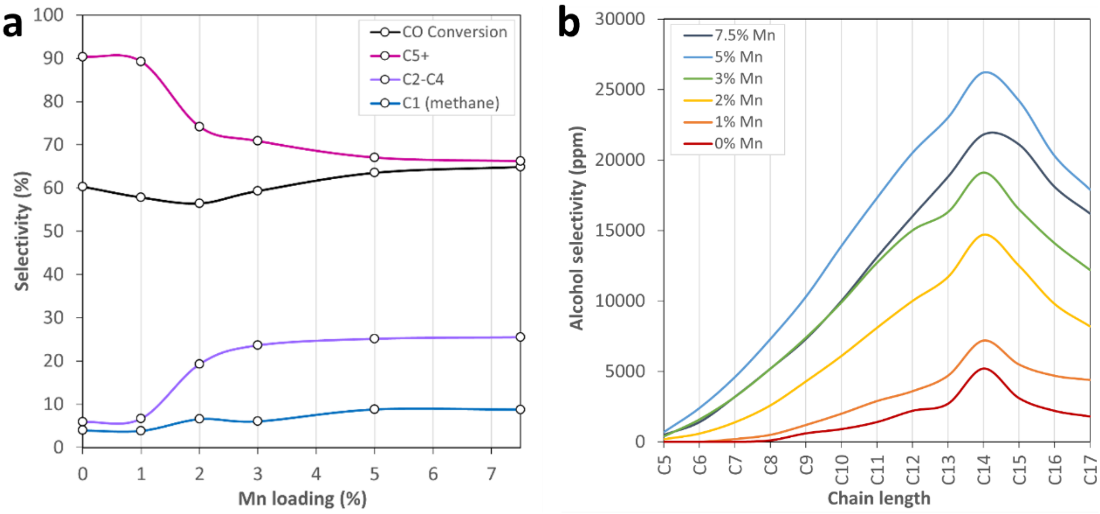

Figure 5.7: Catalytic reaction testing of 10 wt% Co/TiO_2 catalyst with increasing Mn loading. ***(a)*** *Increasing Mn induces a selectivity shift towards short chain products (C_2-C_4).* ***(b)*** *The yield in C_{5+} alcohol products is significantly improved with the addition of Mn, particularly in the 5% Mn loading catalyst.*

Temperature Programmed Reduction (TPR) was used to investigate the bulk reduction behaviour of 10 wt% Co/TiO_2 catalyst with increasing loadings of Mn. A two-stage reduction observed in the calcined 10 wt% Co catalysts was observed for all Mn loadings (**Figure 5.8**). The two main profile peaks R_1 and R_2 are associated with the reduction of Co_3O_4 to CoO and CoO to Co^0 (metal), respectively. A decrease in peak temperatures for these transitions were observed by increasing the Mn content from 0 to 5 wt%, from 390 to 270°C respectively, suggesting an increase in the reducibility of the catalysts with increasing Mn. However, further increase in Mn concentration to 7.5 wt.% saw the effect reverse and peak temperatures increase, in the case of the 10 wt.% Mn catalyst significantly higher than that Co catalyst with no Mn loading. A shoulder peak in R_2 was also seen around 300°C in the 0 wt.% Mn, which is often attributed to the reduction of cobalt titanate species.[32,33] This peak appears to attenuate with increasing Mn loading, suggesting a decrease in the amount of Co-TiO_2 strong metal-support interaction (SMSI) effects. However, this is speculative as the shifting of the more intense CoO to Co^0 peak to lower temperatures is partially obscuring this peak. A 5 wt.% Mn catalyst containing no Co was also subjected to the same TPR conditions from which no peaks were observed, revealing all transitions concerned arise from cobalt reduction.

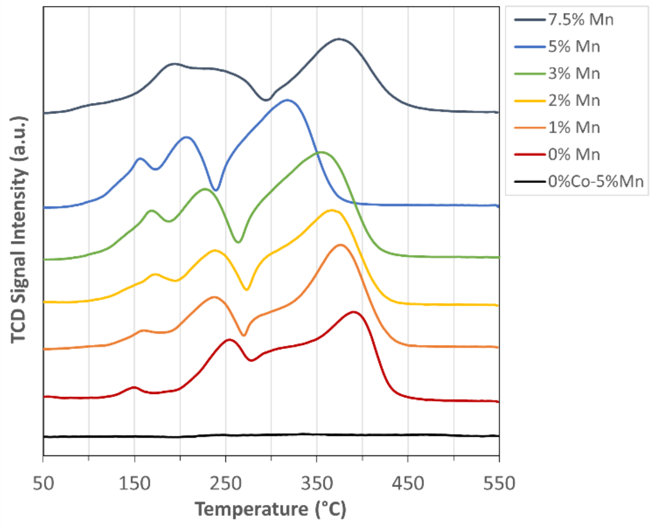

Figure 5.8: TPR profiles of a 10 wt% Co/TiO_2 catalyst with increasing Mn loading *reveals a typical two-stage reduction from Co_3O_4 to CoO and eventually to Co metal. The temperature of Co reducibility is gradually decreased on Mn loading up to 5 wt%, with higher loadings then significantly increasing the peak transition temperatures.*

In situ X-ray absorption spectroscopy (XAS) has been used to investigate the oxidation state of the catalysts post-reduction in H_2 at 300°C for 8-hr. **Figure 5.9a** shows the X-ray absorption near edge structure (XANES) spectra of the Co edge for each Mn-loading, which have been normalised to a metallic Co foil standard. For all samples a clear correlation can be seen to that of the Co metal reference, indicating the catalysts have been reduced to their active state under these conditions. Quantitative estimation of the oxidation state using linear combination fitting (LCF) reveals the Co^0 content of the samples ranging from 94-98% (**Table 1**). For the remaining cobalt oxide, it is possible that the dwell time at 300°C was insufficient to reduce all of the cobalt in the sample or that SMSI effects are hampering the reduction of the fraction of Co which is in direct contact with the TiO_2 support.

A similar conclusion can be drawn from the extended X-ray absorption fine structure (EXAFS) spectra, where all the catalyst spectrum profiles are closely aligned with that of the metallic Co foil reference (**Figure 5.9b**). The additional peaks in the supported catalysts seen at radial distance between 1 and 1.5 Å represents scattering from the Co-O bond, which are relatively small in the Co foil spectrum. The peak amplitude is highest in the Co/TiO_2 specimen, and a trend of decreasing intensity with increased Mn loading is observed. These results indicate a small amount of cobalt oxide phase still exists in the catalysts after the reduction treatment, which decreases with increased Mn loading. This is in contrast with the trend calculated from the XANES results. From the trends observed it is likely the fraction of Co that remains oxidised at 300°C could be reduced to Co metal with a prolonged treatment. The increase in Mn promotion also leads to a slight attenuation in the most intense peak at ~2.2 Å, associated with scattering from the Co-Co bond. This relative decrease is likely a result of the formation of smaller Co nanoparticles upon reduction, which serves to increase the surface area-to-bulk ratio and in turn the fraction of Co with coordinatively unsaturated sites.

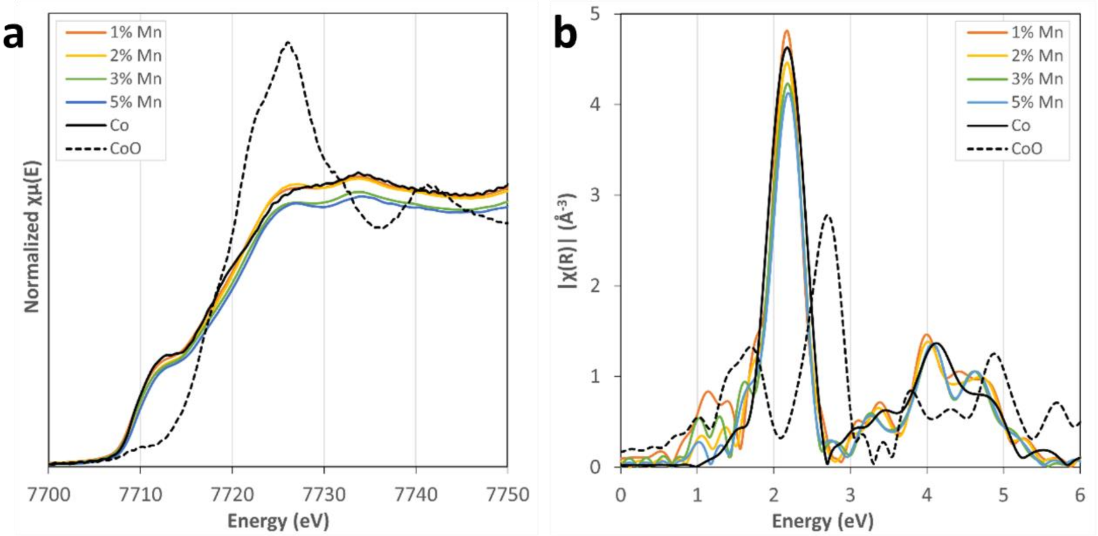

Figure 5.9: In situ XAS of the Co edge in the Mn loaded catalysts after reduction in H_2 at 300°C. *The catalyst spectrum profiles are closely correlated to that of the reference metallic Co foil standard in both* ***(a)*** *XANES and* ***(b)*** *EXAFS. However, the decrease in intensity of peaks between 1 and 1.5 Å in the EXAFS profiles suggests an increase in the fraction of Co reduced with increasing Mn (up to 5 wt% Mn).*

Sample	**Co^0 wt.%**	**Co^{2+} wt.%**	**R-factor**
10%Co/TiO_2	98.3	1.7	0.0010
10%Co-1%Mn/TiO_2	97.7	2.3	0.0004
10%Co-2%Mn/TiO_2	94.3	5.7	0.0003
10%Co-3%Mn/TiO_2	95.6	4.4	0.0009
10%Co-5%Mn/TiO_2	96.8	3.2	0.0010

Table 1: *Quantitative oxidation state composition determined using linear combination fitting (LCF) calculates most of the cobalt to be in the metallic phase.*

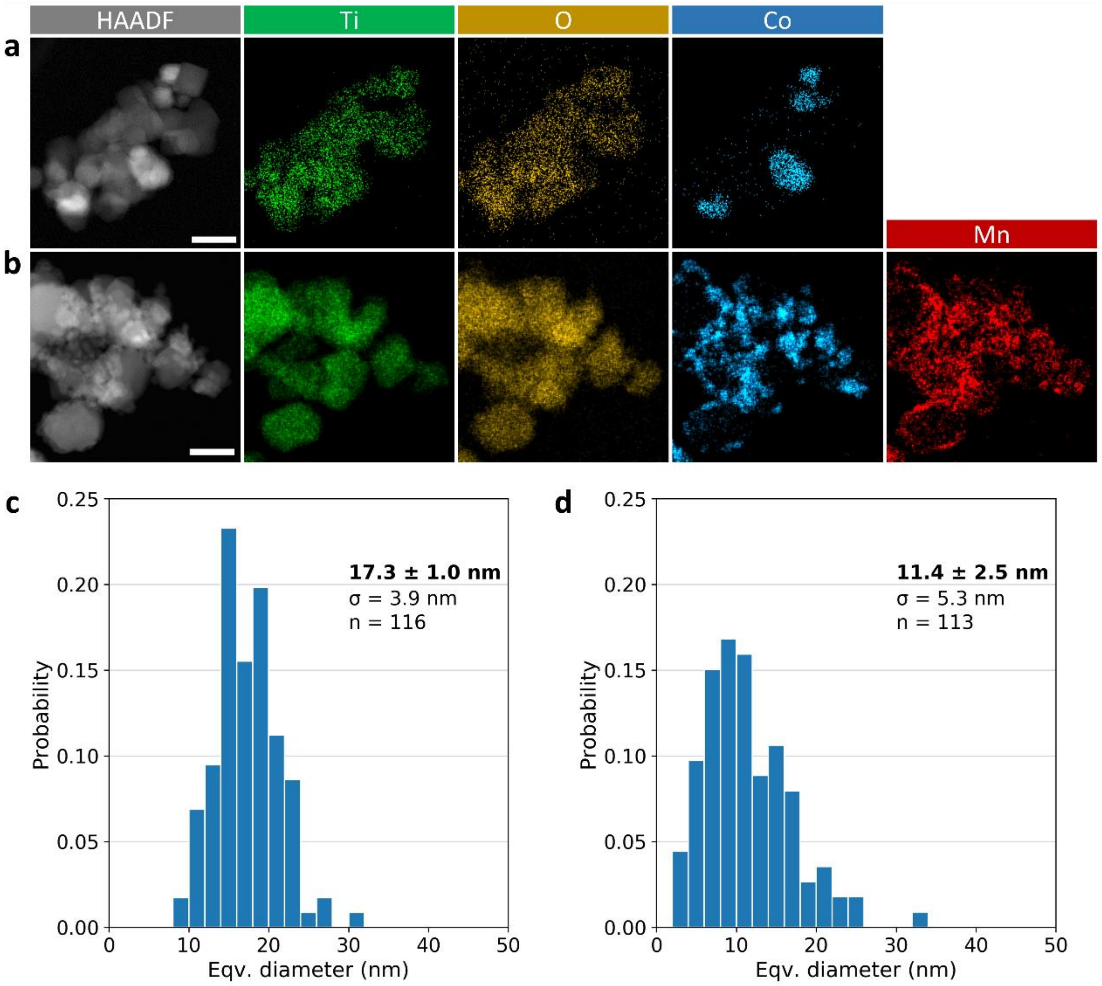

Figure 5.10: HAADF-STEM imaging and STEM-EDS elemental mapping of the TiO_2 supported Co/Mn distribution after ex situ reduction. *Images/maps and particle size analysis for* ***(a,c)*** *10 wt% Co/TiO_2 catalyst (without Mn) and* ***(b,d)*** *10 wt% Co-5wt% Mn/TiO_2 catalyst. Scale bars: 30nm.*

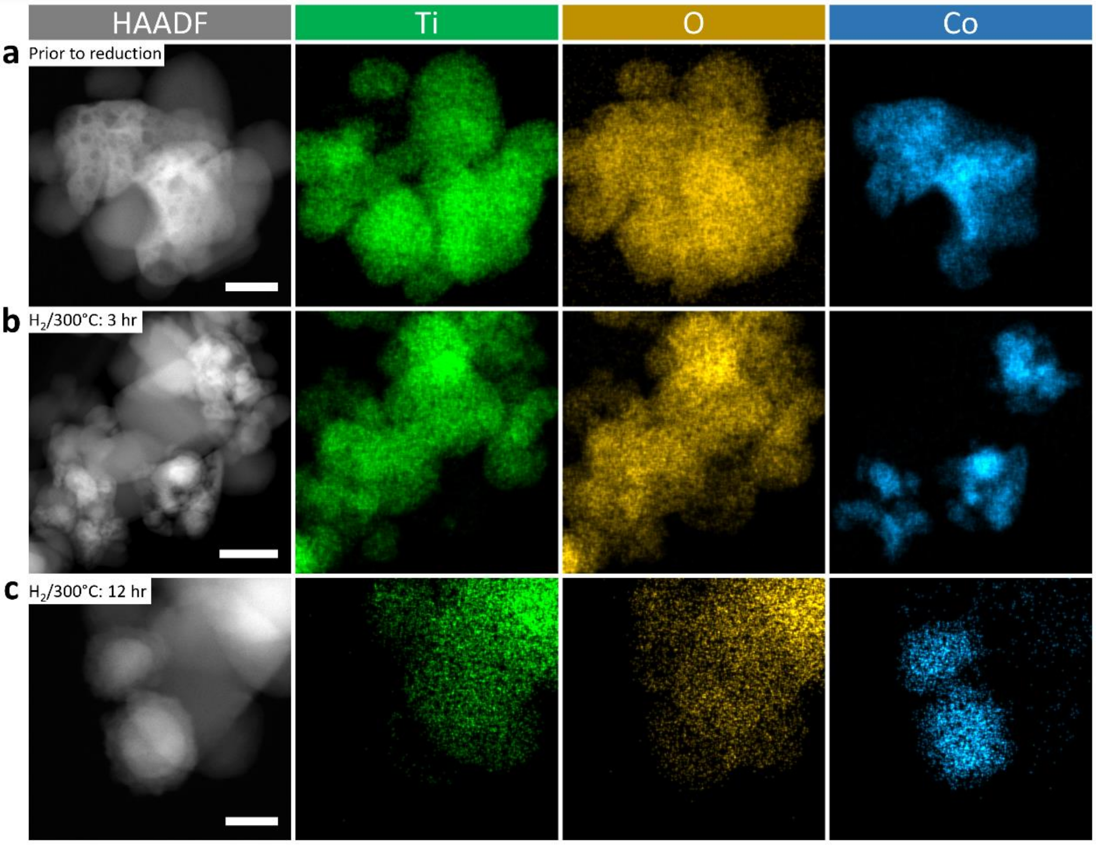

Figure 5.11: HAADF-STEM imaging and STEM-EDS elemental mapping of the 10 wt% Co/TiO$_2$ catalyst. (a) *Irregular shape and presence of Co porosity in the fresh catalyst (prior to reduction). Scale bar: 20 nm.* ***(b)*** *Subjected to a 3-hr reduction in H$_2$. Scale bar: 30 nm.* ***(c)*** *Subjected to a 12-hr H$_2$ reduction reveals densification of the Co particle an presence of an oxidised surface formed when exposed to air (during transfer to microscope). Scale bar: 10 nm.*

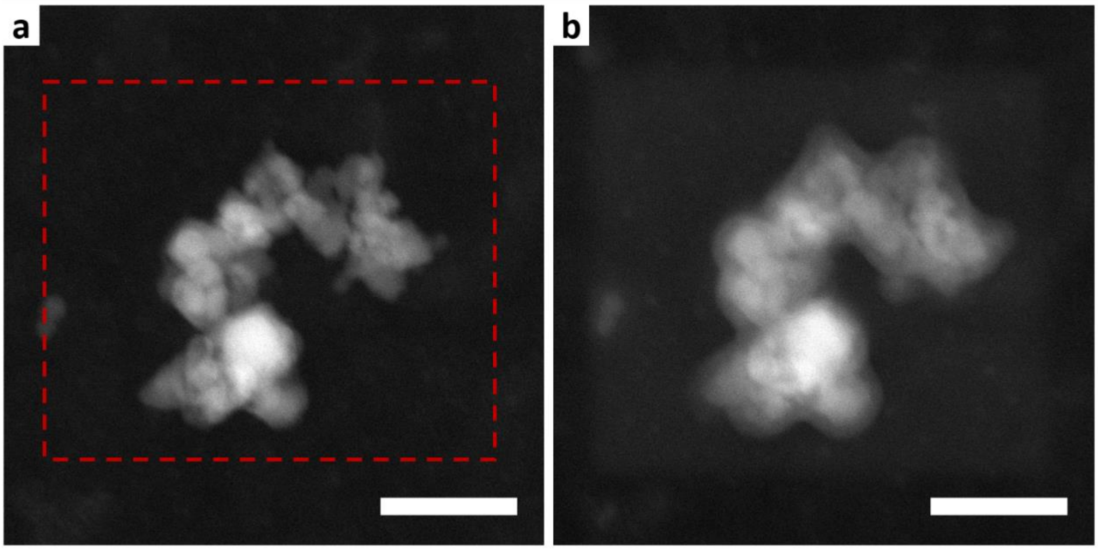

***Figure 5.12: Example of contamination build up in the in situ gas cell at room temperature**. During prolonged exposure to the electron beam i.e., during EDS acquisition a build-up of carbonaceous deposition hinders imaging. A demonstration of this is provided in **(a)** the clearly defined sample highlighted by the EDS ROI (red box) and **(b)** the subsequent 'clouding' of the sample making further analysis difficult. Scale bars: 100 nm.*

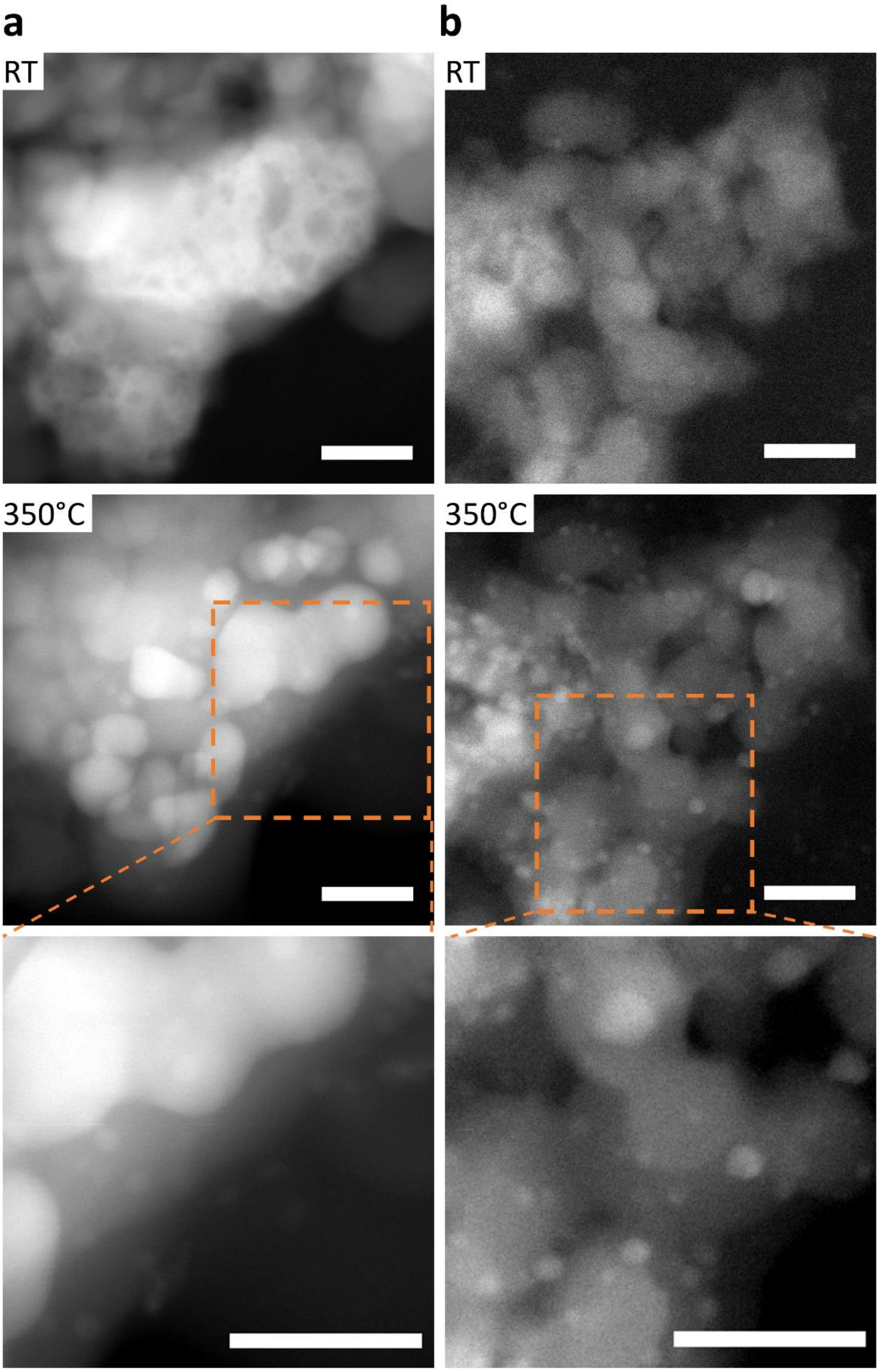

Figure 5.13: In situ HAADF-STEM imaging in H_2. (a) *10 wt% Co/TiO_2 catalyst (without Mn), highlighting the readily distinguishable Co clustering and porous structure at room temperature (RT). Increasing temperature to 350°C leads to particle sintering/coalescence (see Figures 5.3 and 5.14 for intermediate temperatures) and the formation of new much smaller paticles.* ***(b)*** *10 wt% Co-5 wt% Mn/TiO_2 catalyst with the highly distributed Co and Mn undiscernible from the support particles at RT. Particle formation observed during temperature increase (Figure 5.14) show significantly smaller range of particle sizes. Scale bars: 30 nm*

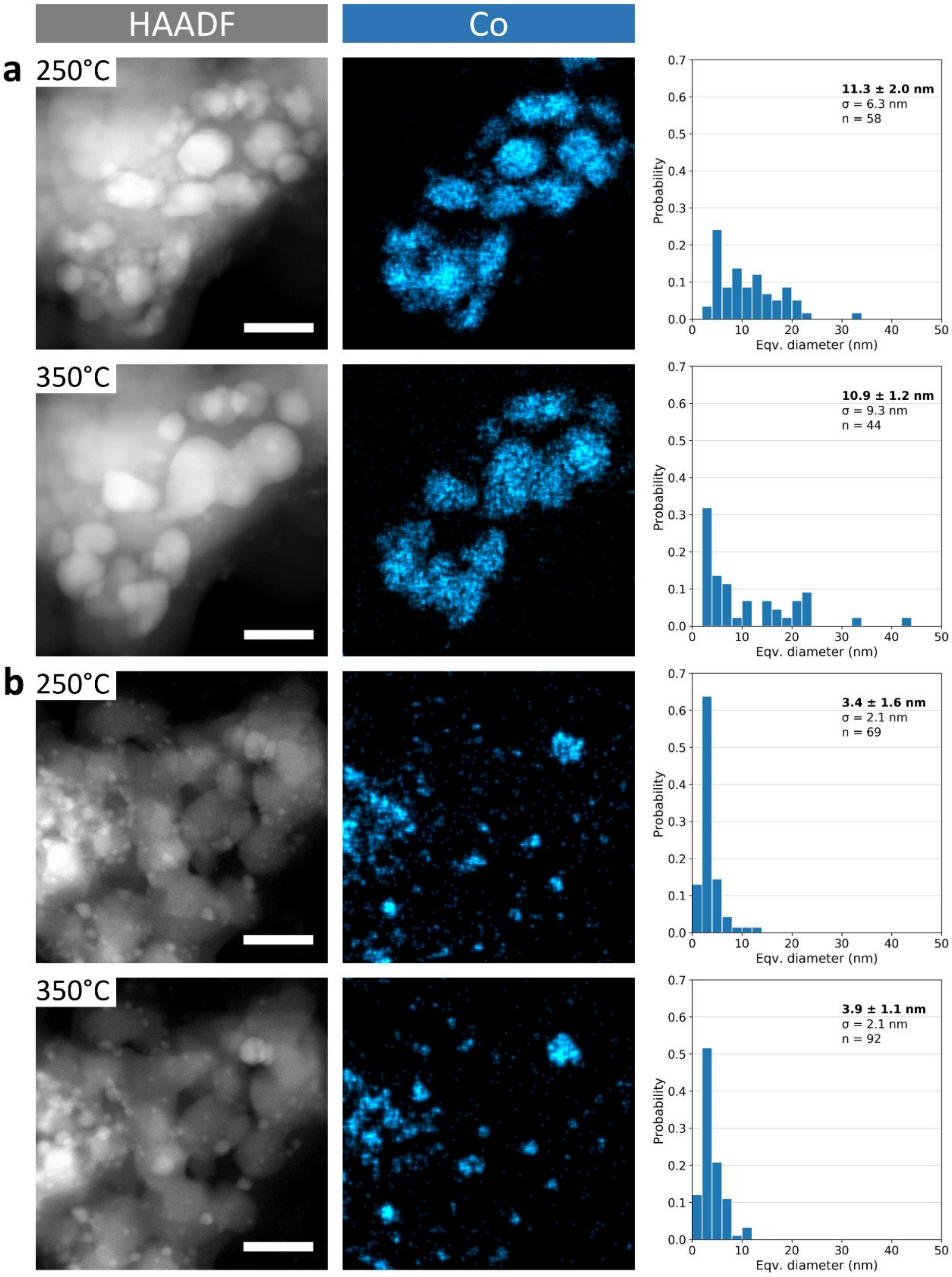

***Figure 5.14: In situ HAADF-STEM imaging and STEM-EDS elemental mapping used to perform Co particle size analysis**. Analysis of Co particle size evolution during in situ STEM elemental analysis for **(a)** the 10 wt.% Co/TiO_2 catalyst (without Mn) and **(b)** 10 wt.% Co-5wt.% Mn/TiO_2 catalyst. In each case the HAADF STEM image is presented (left) with the histogram of nanoparticle size distribution (right). Scale bars: 30 nm.*

		E, eV	Total spin	Mulliken adatom spin	Mulliken adatom charge	Hirschfeld adatom charge	Distances to the nearest oxygen atoms, A			
Co	a)	0.00	2	2.0	0.8	0.5	1.89	1.89	2.03	2.77
	b)	0.03	2	2.1	1.0	0.5	1.95	1.95	2.03	2.06
	c)	0.27	2	2.1	0.9	0.6	1.88	1.94	2.03	2.67
	d)	0.74	2	2.0	0.9	0.6	1.83	1.88	2.23	3.06
	e)	0.83	2	2.1	0.8	0.6	1.81	1.88	2.79	2.79
Mn	a)	0.00	5	4.8	1.1	0.9	1.91	1.91	2.13	2.41
	b)	1.25	4	4.5	1.0	0.8	1.87	1.95	2.22	3.12
	c)	1.25	6	5.9	0.7	0.6	2.01	2.27	3.42	3.42
	d)	1.80	5	5.6	0.5	0.5	1.98	3.28	3.31	4.12

Table 2. *Characteristics of Co and Mn adatoms on anatase (101): relative energy, total spin, atomic spin and charge of metal adatom, distances to four nearest oxygen atoms.*

Bibliography

1. Paterson, J. *et al.* Manipulation of Fischer-Tropsch Synthesis for Production of Higher Alcohols Using Manganese Promoters Higher Alcohols using Manganese Promoters. (2018).

2. Morales Cano, F., Gijzeman, O. L. J., de Groot, F. M. F. & Weckhuysen, B. M. Manganese promotion in cobalt-based Fischer-Tropsch catalysis. in *Natural Gas Conversion VII* (eds. Bao, X. & Xu, Y. B. T.-S. in S. S. and C.) vol. 147 271–276 (Elsevier, 2004).

3. Morales, F. & Weckhuysen, B. M. *Promotion Effects in Co-based Fischer–Tropsch Catalysis*. vol. 19 (Catalysis, 2006).

4. Vannice, M. A. The Catalytic Synthesis of Hydrocarbons from H2/CO Mixtures over the Group VIII Metals. *J. Catal.* **37**, 449–461 (1975).

5. Bezemer, G. L. *et al.* Cobalt Particle Size Effects in the Fischer - Tropsch Reaction Studied with Carbon Nanofiber Supported Catalysts. 11568–11569 (2006).

6. den Breejen, J. P. *et al.* On the Origin of the Cobalt Particle Size Effects in Fischer−Tropsch Catalysis. *J. Am. Chem. Soc.* **131**, 7197–7203 (2009).

7. Khodakov, A. Y., Chu, W. & Fongarland, P. Advances in the development of novel cobalt Fischer-Tropsch catalysts for synthesis of long-chain hydrocarbons and clean fuels. *Chem. Rev.* **107**, 1692–1744 (2007).

8. Rytter, E. & Holmen, A. On the support in cobalt Fischer–Tropsch synthesis - Emphasis on alumina and aluminates. *Catal. Today* **275**, 11–19 (2016).

9. Martínez, A., López, C., Márquez, F. & Díaz, I. Fischer–Tropsch synthesis of hydrocarbons over mesoporous Co/SBA-15 catalysts: the influence of metal loading, cobalt precursor, and promoters. *J. Catal.* **220**, 486–499 (2003).

10. Moradi, G. R., Basir, M. M., Taeb, A. & Kiennemann, A. Promotion of Co/SiO2

Fischer–Tropsch catalysts with zirconium. *Catal. Commun.* **4**, 27–32 (2003).

11. Dinse, A., Aigner, M., Ulbrich, M., Johnson, G. R. & Bell, A. T. Effects of Mn promotion on the activity and selectivity of Co/SiO2 for Fischer–Tropsch Synthesis. *J. Catal.* **288**, 104–114 (2012).

12. Paterson, J. *et al.* Manipulation of Fischer-Tropsch Synthesis for Production of Higher Alcohols Using Manganese Promoters. *ChemCatChem* **10**, 5154–5163 (2018).

13. Paterson, J., Partington, R., Peacock, M., Sullivan, K. & Wilson, J. Elucidating the Role of Bifunctional Cobalt-Manganese Catalyst Interactions for Higher Alcohol Synthesis. 2312–2324 (2020) doi:10.1002/ejic.202000397.

14. Morales, F. *et al.* Mn promotion effects in Co/TiO2 Fischer-Tropsch catalysts as investigated by XPS and STEM-EELS. *J. Catal.* **230**, 301–308 (2005).

15. Morales, F., Grandjean, D., De Groot, F. M. F., Stephan, O. & Weckhuysen, B. M. Combined EXAFS and STEM-EELS study of the electronic state and location of Mn as promoter in Co-based Fischer-Tropsch catalysts. *Phys. Chem. Chem. Phys.* **7**, 568–572 (2005).

16. Ciobîcă, I. M., van Santen, R. A., van Berge, P. J. & van de Loosdrecht, J. Adsorbate induced reconstruction of cobalt surfaces. *Surf. Sci.* **602**, 17–27 (2008).

17. Hansen, P.L.; Wagner, J. B. Atomic resolved imaging of dynamic shape changes in supported copper nanocrystals. *Science (80-.).* **295**, 2053–2055 (2002).

18. Creemer, J. F. *et al.* A MEMS reactor for atomic-scale microscopy of nanomaterials under industrially relevant conditions. *J. Microelectromechanical Syst.* **19**, 254–264 (2010).

19. Yaguchi, T. *et al.* Development of a high temperature-atmospheric pressure environmental cell for high-resolution TEM. *J. Electron Microsc. (Tokyo).* **60**, 217–225 (2011).

20. Allard, L. F. *et al.* Novel MEMS-based gas-cell/heating specimen holder provides advanced imaging capabilities for in situ reaction studies. *Microsc. Microanal.* **18**, 656–666 (2012).

21. Sun, X. *et al.* Manufacture of highly loaded silica-supported cobalt Fischer–Tropsch catalysts from a metal organic framework. *Nat. Commun.* **8**, 1680 (2017).

22. Johnson, G. R. *et al.* Investigations of element spatial correlation in Mn-promoted Co-based Fischer–Tropsch synthesis catalysts. *J. Catal.* **328**, 111–122 (2015).

23. Paterson, J. *et al.* Manipulation of Fischer-Tropsch Synthesis for Production of Higher Alcohols Using Manganese Promoters. *ChemCatChem* **10**, (2018).

24. Paterson, J., Peacock, M., Ferguson, E., Purves, R. & Ojeda, M. In Situ Diffraction of Fischer–Tropsch Catalysts: Cobalt Reduction and Carbide Formation. *ChemCatChem* **9**, 3463–3469 (2017).

25. Labat, F., Baranek, P. & Adamo, C. Structural and Electronic Properties of Selected Rutile and Anatase TiO2 Surfaces: An ab Initio Investigation. *J. Chem. Theory Comput.* **4**, 341–352 (2008).

26. Ohtani, B., Prieto-Mahaney, O. O., Li, D. & Abe, R. What is Degussa (Evonik) P25? Crystalline composition analysis, reconstruction from isolated pure particles and photocatalytic activity test. *J. Photochem. Photobiol. A Chem.* **216**, 179–182 (2010).

27. Peña, F. de la *et al.* hyperspy/hyperspy: Release v1.6.5. (2021) doi:10.5281/ZENODO.5608741.

28. Blum, V. *et al.* Ab initio molecular simulations with numeric atom-centered orbitals. *Comput. Phys. Commun.* **180**, 2175–2196 (2009).

29. Fricke, B. & Pershina, V. Atomic and Molecular Structure Calculations for Superheavy Elements. *J. Nucl. Radiochem. Sci.* **3**, 109–111 (2002).

30. Wellendorff, J., Lundgaard, K. T., Jacobsen, K. W. & Bligaard, T. mBEEF: An

accurate semi-local Bayesian error estimation density functional. *J. Chem. Phys.* **140**, 144107 (2014).

31. Akimenko, S. S. *et al.* SuSMoST: Surface Science Modeling and Simulation Toolkit. *J. Comput. Chem.* **41**, 2084–2097 (2020).

32. Riva, R., Miessner, H., Vitali, R. & Del Piero, G. Metal-support interaction in Co/SiO2 and Co/TiO2. *Appl. Catal. A Gen.* **196**, 111–123 (2000).

33. Feltes, T. E. *et al.* Selective adsorption of manganese onto cobalt for optimized Mn/Co/TiO2 Fischer-Tropsch catalysts. *J. Catal.* **270**, 95–102 (2010).

Chapter 6

Determining the Limits of Electron Energy-Loss Spectroscopy Analysis of Heterogeneous Catalysts during *In Situ* Gas Cell Scanning Transmission Electron Microscopy

The work in this chapter explores the experimental practicalities of performing scanning transmission electron microscopy (STEM) electron energy loss spectroscopy (EELS) during *in situ* gas cell application. Signal intensity loss from EELS core-loss edges is observed when performing gas cell observations, largely due to the presence of the gaseous environment and encapsulating silicon nitride membrane windows. A series of experiments using Co-based specimens were undertaken to establish the extent of scattering contribution from the gas and windows over a range of pressures and temperatures. At typical operating conditions (1 bar N_2/H_2) a temperature effect was observed which acted to diminish the increased scattering contribution from the gas. Increased temperatures (>200°C) also demonstrated much less contamination deposition, which impacts signal collection and will limit observation of some reactions, for example low temperature reduction of metal oxides.

This manuscript was drafted by M. Lindley, with contributions and edits from S. J. Haigh. Catalyst synthesis was performed industrially and provided by J. Paterson. STEM-EELS sample preparation, experimental acquisition and data analysis/processing was performed by M. Lindley. This manuscript has not yet been submitted.

Determining the Limits of Electron Energy-Loss Spectroscopy Analysis of Heterogeneous Catalysts during *In Situ* Gas Cell Scanning Transmission Electron Microscopy

Matthew Lindley[1], James Paterson[2], Chris Hardacre[3], Sarah J. Haigh[1]

[1] Department of Materials, University of Manchester, Oxford Road, Manchester, M13 9PL, United Kingdom

[2] BP, Saltend Chemicals Park, Hull, HU12 8DS, United Kingdom

[3] Department of Chemical Engineering and Analytical Science, University of Manchester, Oxford Road, Manchester, M13 9PL, United Kingdom

Abstract

The functionality of heterogeneous catalysts is influenced by dynamic surface processes that occur on the atomic scale. *In situ* gas cell scanning transmission electron microscopy (STEM) combined with electron energy loss spectroscopy (EELS) provides the ability to probe the structural, morphological, and chemical characteristics at this scale at pressures up to 1 bar and temperatures up to 1000°C. However, the combination of the relatively high pressures and the electron transparent membranes used to contain the gas leads to a significant degradation in the EELS signal achievable. As a result, little work has been published combining these techniques. In this work we assess the influence of pressure and temperature on STEM-EELS using Co-based nanoparticle catalysts and determine the presence of membrane windows to be the significant factor impacting the quality of spectra acquisition. We assess the relative thickness of the cell to distinguish the effects from the membrane, static gas (i.e., closed cell, not flowing) and applied temperature during typical in situ operation and evaluate these effects on the EELS spectrum signal-to-noise ratio (SNR) using Co-based catalysts.

Introduction

Atomic scale observation of reaction-induced transformations in heterogeneous catalysts during exposure to industrially relevant conditions is key to understanding complex and dynamic structure-activity relationships.[1] *In situ* scanning transmission electron microscopy (STEM) is a high spatial-resolution characterisation technique, which allows heterogeneous catalysts to be observed at elevated temperatures and when surrounded by gaseous atmospheres.[2] When paired with electron energy loss spectroscopy (EELS) or energy dispersive X-ray spectroscopy (EDS), STEM can also provide a wealth of high spatial resolution analytical information. For heterogeneous catalysts *ex situ* STEM-EELS and EDS have been widely used for establishing the elemental distribution of the catalyst/promoter[3] as well as the local oxidation state for nanoparticle materials.[4,5]

There are two approaches to achieve imaging of a solid material surrounded by a gaseous environment within the high vacuum of the TEM. The first demonstrated approach requires a dedicated differential pumping TEM microscope (termed environmental (S)TEMs, or E(S)TEMs) where the pumps prevent the gas atmosphere around the sample damaging the electron gun.[6] ESTEM allows for unhindered transmission of the electron beam, although the electron's mean-free path is significantly reduced by the relatively large path length of the gas around the sample (~4-7 mm), with achievable gas pressures often in the mbar range.[7] The alternative method to achieve *in situ* STEM for gaseous environments employs environmental cell (E-cell) specimen holders with thin, impermeable, electron transparent, membrane windows, which confine the gas in the microscope but allow the electron beam to penetrate. These membranes are typically made from Si_3N_4 and are ~30-50 nm thick.[8] E-cells enable the path length for the gas volume to be much smaller than is possible in an ESTEM (μm rather than mm) and the maximum achievable gas pressures are also higher (typically up to 1 bar for commercial systems).[9,10] However, this is only achieved at the cost of increased electron scattering due to the presence of the membrane window material.

Ultimately, both ESTEM and E-cell approaches lead to a loss in STEM imaging resolution and analytical capabilities compared to *ex situ* studies performed in vacuum.[11] The degradation of high-resolution transmission electron microscopy (HR-TEM) and annular dark field (ADF) STEM imaging resolution have both been quantified in previous work.[11,12] There is no doubt that interpreting the structure of heterogeneous catalysts would greatly benefit from the STEM's analytical capabilities to complement *in situ* STEM imaging and aid interpretation of local oxidation states or elemental distribution. Nonetheless, there is a notable lack of literature reporting on the use of STEM-EELS using gas cell holders.

Here we demonstrate systematically how different experimental conditions determine the detection capability for in situ STEM-EELS analysis of heterogeneous catalysts. The results provide important insights that can be applied to optimize these challenging experiments and motivate development of E-cells with improved analytical capabilities.

***In situ* Gas Cell EELS**

The Protochips Atmosphere commercial *in situ* gas E-cell comprises two Si chips, each with a thin membrane region in the centre with dimensions 300x300 μm (**Figure 6.1a)**. The membranes then contain six electron transparent Si_3N_4 windows, on which the sample is observed. All windows are 10 μm diameter with those in the top chip being ~30 nm thick while those in the bottom chip are ~50 nm. For optimal STEM imaging samples are attached to the underside of the upper membrane to minimize scattering of the electron probe before interaction with the specimen. The top chip also contains a SiC layer which is electrically contacted to supply resistive heating to the sample and gaseous environment.

To illustrate the challenge of performing *in situ* STEM-EELS for an industrial heterogeneous catalyst using an E-cell set up, **Figure 6.1b** and **6.1c** compare the high angle annular dark field (HAADF)-STEM images and summed EELS spectra obtained *in situ* (1 bar N_2 at 200°C) versus *ex situ* (in vacuum). The sample is highly dispersed Co and Mn supported on nanoparticulate TiO_2 (Degussa, P25) and prepared by wet impregnation (see methods). Although the spatial resolution of the HAADF-STEM image is slightly reduced by the presence of the gas environment, much more obvious are the differences in the summed EELS

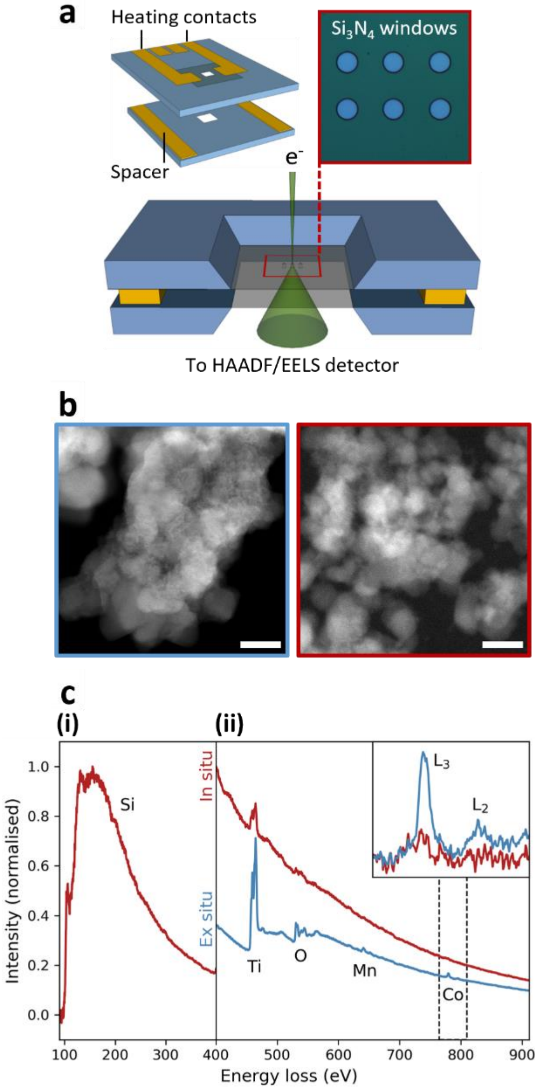

Figure 6.1: Overview of the in situ gas cell. (a) *Schematic of the gas cell components and cross section of the fully constructed cell. Electron transparent Si_3N_4 membrane windows (blue circles) contain the gaseous atmosphere and provides support for the specimen during STEM imaging/EELS acquisition.* ***(b)*** *HAADF-STEM images of a highly dispersed $CoMn/TiO_2$ catalyst. Left image is ex situ, i.e., in vacuum (blue border) while right image is in situ imaging during exposure to 1 bar N_2 at 200°C (red border). Scale bars = 50 nm.* ***(c)*** *Experimental summed EELS spectra for the $CoMn/TiO_2$ catalyst imaged* ***(i)*** *in situ (1 bar N_2 at 200°C) showing the unwanted Si signal present due to the E-cell windows.* ***(ii)*** *Comparison of the EELS in situ data (red line) with ex situ vacuum data (blue line) showing the effect this high Si background has on reducing subsequent detection of core-loss Co and Mn edges from the specimen for in situ conditions. In particular, high-loss edges, such as the L_3/L_2 peaks from Co, can become reduced below spectral noise as shown by the enlarged spectral region at ~780 eV (inset).*

spectra for *in situ* and *ex situ* imaging. Most seriously, the *in situ* EELS data contains a strong Si signal produced by the beam interacting with the SiN windows above and below the sample. No Si peak is present in the *ex situ* sample. **Figure 6.1c(i)** shows the background subtracted Si $L_{2,3}$-edges (at ~100 eV) normalized to the broad L_1 peak intensity at 149 eV. The spectrum highlights the significant intensity of the extended fine structure in the post-ionisation edge region, which is then superimposed on latter spectral peaks and acts to reduce the signal-to-background ratio (SBR) in subsequent EELS edges. This is evident in **Figure 6.1c(ii)** where the relative intensity of the CoMn/TiO_2 specimen edges is much lower for the *in situ* acquisition. Indeed, for core-loss signals at increased energy loss, such as Co (demonstrated inset) the SBR is reduced such that the signal is indistinguishable from the spectral noise.

For this experiment an unreactive *in situ* gas environment was employed to prevent any chemical or morphological change to the sample and the imaging conditions were chosen to maximize the electron dose incident on the sample while avoiding detectable electron beam damage. Identical imaging conditions were employed *in situ* and *ex situ* (see methods). To prevent thickness effects (i.e., plural scattering) from the specimen as much as possible, EELS was acquired at regions where the supporting titania particles were evenly distributed (i.e., reduced overlap of particles). To increase the SBR of the EELS signal the presented spectra were summed over the specimen region of interest (280 nm by 280 nm as shown in **Figure 6.1b**) and it is important to note that where higher spatial resolution EELS spectrum is required this will have a correspondingly poorer SBR. Furthermore, where it is desirable to investigate dynamic changes occurring as a result of a reactive gas environment *in situ*, the need for temporal resolution will likely drive a further lowering of the achievable SBR.

Relative Thickness Changes during In Situ Workflow

To propose optimal conditions for EELS detection during *in situ* STEM it is necessary to understand the origin of EELS signal loss compared to *ex situ* analysis. Various aspects of the gas E-cell could contribute to a loss of signal including the Si_3N_4 membrane, gas pressure, and temperature. First, we consider a gas cell top chip without a fully constructed cell (shown

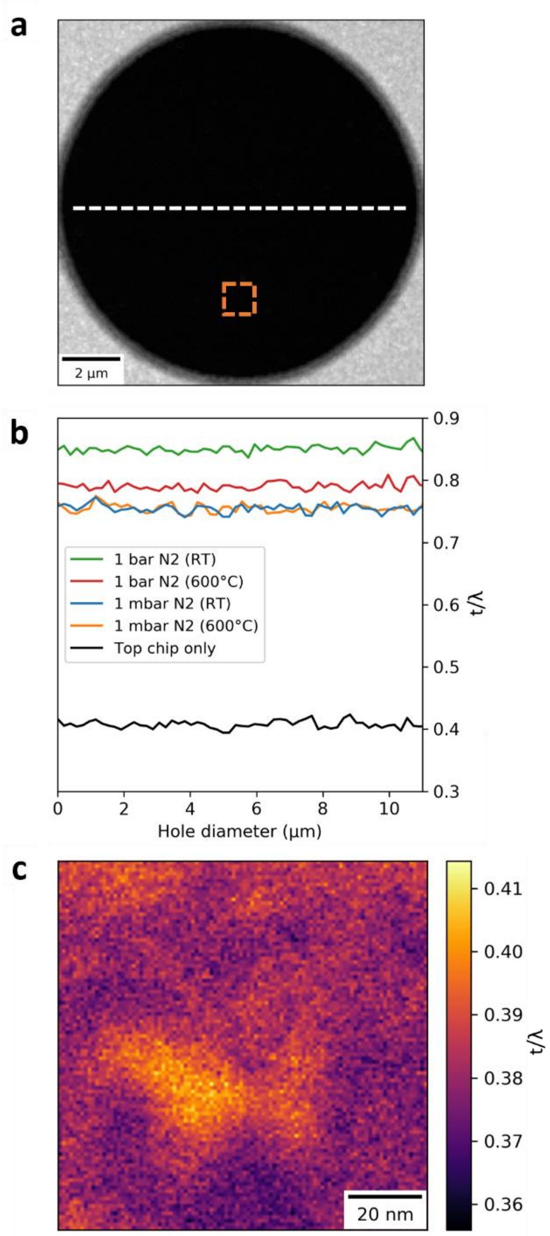

Figure 6.2: Relative thickness measurements of the E-cell for different experimental conditions. ***(a)*** *HAADF-STEM image of just the top chip showing the region of one* Si_3N_4 *window (spanning the circular void etched into the SiC heating membrane).* ***(b)*** *t/λ line profiles for the region indicated by the white dotted line in (a) for conditions of: only top chip; fully constructed E-cell filled with 1 mbar* N_2 *at room temperature (RT) and at 600°C; fully constructed E-cell filled with 1 bar* N_2 *at RT and at 600°C.* ***(c)*** *Spatial distribution of t/λ for the top chip only in the region of the orange dashed square in (a) revealing a ~20% variation in relative thickness of the membrane.*

in the HAADF-STEM image in **Figure 6.2a**). The higher intensity outer regions highlight the location of the thicker SiC heating membrane. To demonstrate the electron scattering associated with the 30 nm thick SiN membrane, EELS line profiles were acquired across the full width of the window (indicated by the white dotted line). These measurements were used to calculate t/λ values, i.e., the mean number of scattering events per incident electron, from the intensity loss of the zero loss peak (ZLP). This data was then compared to equivalent measurements for the fully constructed empty E-cell (pumped internally to 1 mbar N_2) at room temperature (RT) and at 600°C, as well as for the E-cell containing 1 bar N_2 at RT and 600°C (**Figure 6.2b**). The individual acquisitions are shown in SI Figure 6.6.

The top-chip window alone gives a mean t/λ ≈ 0.4, which increases to ≈ 0.75 when the cell is fully constructed and both windows are present, with the result the same at both RT and 600°C. The increase in relative thickness highlights the significant effect of the windows in increasing electron scattering, as we approach a situation where plural scattering (t/λ = 1) is becoming dominant before any sample interaction. This value increases to t/λ ≈ 0.85 upon introduction of 1 bar N_2 to the cell, due to the interaction with the gas molecules. Interestingly, increasing the temperature to 600°C causes a corresponding reduction in scattering (t/λ ≈ 0.8), indicating a reduction in gas molecule interaction at increased temperature.

Distinguishing Thickness Effects from Membrane and Gas

To understand the origin of the reduction in t/λ at elevated temperature, core-loss EELS spectra were collected for the N K-edge (around 400 eV energy loss) as a function of temperature (RT-800°C). As shown in **Figure 6.3a** all the spectra show a peak at ~404 eV, which arises from the nitride membrane (confirmed by EELS spectra taken of the cell with no gas present, shown in red) the intensity of which looks to be independent of temperature. For the filled cells, the spectra also contain an N_2 peak (at 402 eV) the intensity of which gradually decreases with increasing temperature. This demonstrates a reduction in beam/gas interaction, suggesting a decrease in gas density, which can be expected at elevated temperature.

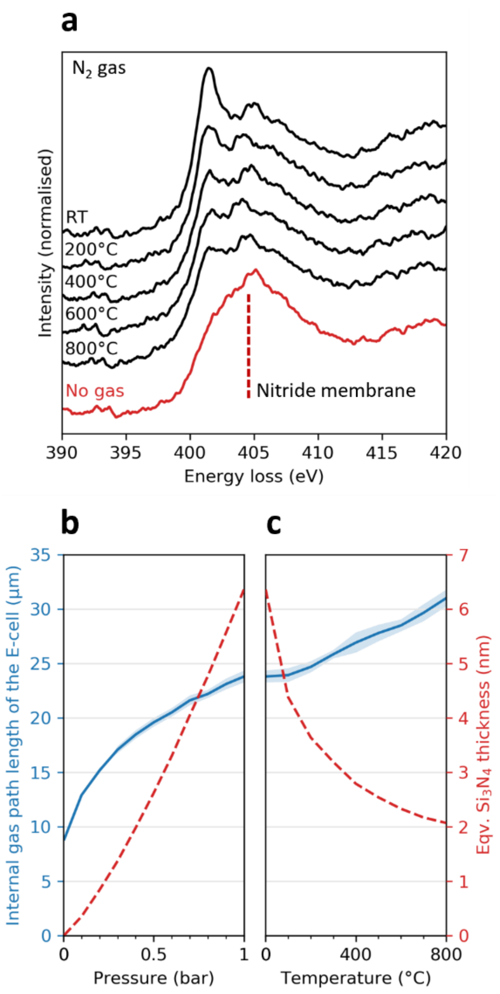

Figure 6.3: Effect of pressure and temperature on the internal gas path length of the E-cell ***(a)*** *Measurement of the effect of increasing temperature on the core-loss spectra of nitrogen when the gas E-cell is filled with* N_2 *(1 bar pressure).* ***(b,c)*** *Measurement of internal gas path length of the E-cell,* t_{gas} *(blue line) as a function of* ***(b)*** *increasing pressure (at RT) and* ***(c)*** *increasing temperature (at 1 bar* N_2*). Measurements were averaged over several particles in each of the six windows and the variability is shown as the light blue shading. Internal gas path length measurements were then used to calculate a thickness of* Si_3N_4 *that is representative of the gas present during the same experimental protocol (red dashed line, found to be up to 6.5 nm).*

An increase in either gas pressure or temperature for the E-cell is known to cause outward bulging, increasing the effective path length of the gas, with the potential to increase gas interaction.[13] Within the individual window areas the cells have relatively constant thickness (no change in t/λ), which shows that the windows themselves are not bulging. However, as illustrated schematically in Figure 6.1a, the windows are only in the central 50 μm of the 300 μm wide thinned membrane. To calculate the extent of bulging, Au nanoparticles (NPs) were deposited on the interior of both the top and bottom chip cell membranes to provide a clear focal plane. The differential focus of the STEM electron probe was then quantified to measure the internal gas path length of the cell as a function of N_2 pressure up to 1 bar **(Figure 6.3b)**, the cell was then sealed and the measurements repeated with increasing temperature from RT to 800°C (**Figure 6.3c)**. At 5 mbar the internal gas path length, t_{gas}, of the E-cell is ~9 μm, (larger than the 5 μm cell spacer due to the pressure differential between the cell and the column vacuum). As the pressure is increased the internal gas path length follows the expected logarithmic behaviour, expanding to ~24 μm at 1 bar N_2 pressure. Increasing temperature at fixed pressure produces a close to linear rate of increase for the internal gas path length, reaching ~31 μm at 800°C with only minimal variability across different windows (indicated by the light blue shading).

To quantify the relative contribution of the N_2 gas compared to the Si_3N_4 windows, we have converted the internal gas path length to an equivalent thickness of Si_3N_4 using a similar analysis used previously to account for image resolution degradation in ESTEM.[11] This method assumes the gas molecules within the cell act together as a solid thin foil, so that the ideal gas law can be applied to equate the molar volume of gas with thickness of t_{gas} to solid Si_3N_4 with a thickness of t_{Si3N4}:

$$\frac{P}{RT}t_{gas} = \frac{\rho}{W}t_{Si3N4}$$

where P is the N_2 pressure (1 bar), R is the ideal gas constant (8.3145 J mol^{-1} K^{-1}), ρ is the density of Si_3N_4 (3.2x10^{6} g m^{-3}) and W is the mean molar mass (20.0 g mol^{-1}). The results show that at RT, the equivalent thickness of gas increases approximately linearly with increasing pressure, reaching 6.4 nm at 1 bar N_2, 8.1% of the total thickness of Si_3N_4 from the membranes (**Figure 6.3b**). However, when increasing the temperature up to 800°C at constant pressure, the equivalent thickness reduces to 2 nm, just 2.5% of the total thickness of Si_3N_4 from the membranes. The additional thickness is superimposed on variations in thickness of the individual membranes which are ~3 nm, as shown by the 10% variations in t/λ for regions separated by just 10 nm (**Figure 6.2c**). This analysis demonstrates that the Si_3N_4 windows are dominating the electron scattering and, consequently, the bottleneck in providing the required dose to yield data from which a robust signal to noise ratio (SNR) can be determined.

Gas Cell Impact on Sample Spectra Acquisition

Having established the principal cause of the degraded EELS signal for *in situ* data, we now examine the effect this will have on EELS characterization for heterogeneous nanoparticle catalysts. Even before considering the closed cell, it is clear that the variations in the thickness of one window (**Figure 6.2c)** are of a similar magnitude to the thickness of many heterogeneous catalyst nanoparticles. The consequence of this is that the windows themselves will likely compromise the effective use of EELS even for just for the relatively simple measurement of specimen thickness (t/λ) within the E-cell. To consider the effect of the degraded EELS signal on analysis of specimen core-loss edges, used for elemental analysis and measurement of local oxidation state, Co_3O_4 NPs with a mean diameter of 50 nm were examined. This specimen was chosen as a representative catalyst material but one where the relatively large particle size, lack of support and sharp onset EELS peaks for Co at relatively low energy provides highly favorable conditions for EELS analysis.

Figure 6.4a shows the summed EELS spectra for Co_3O_4 NPs for temperatures in the range 100-400°C, where an increasing core-loss peak signal is observed with increased temperature. **Figure 6.4c** quantitatively demonstrates the effect of EELS acquisition temperature on the Co core loss SNR, defined as the peak intensity of the Co L_3 edge divided by the standard deviation of the pre-peak noise after background subtraction

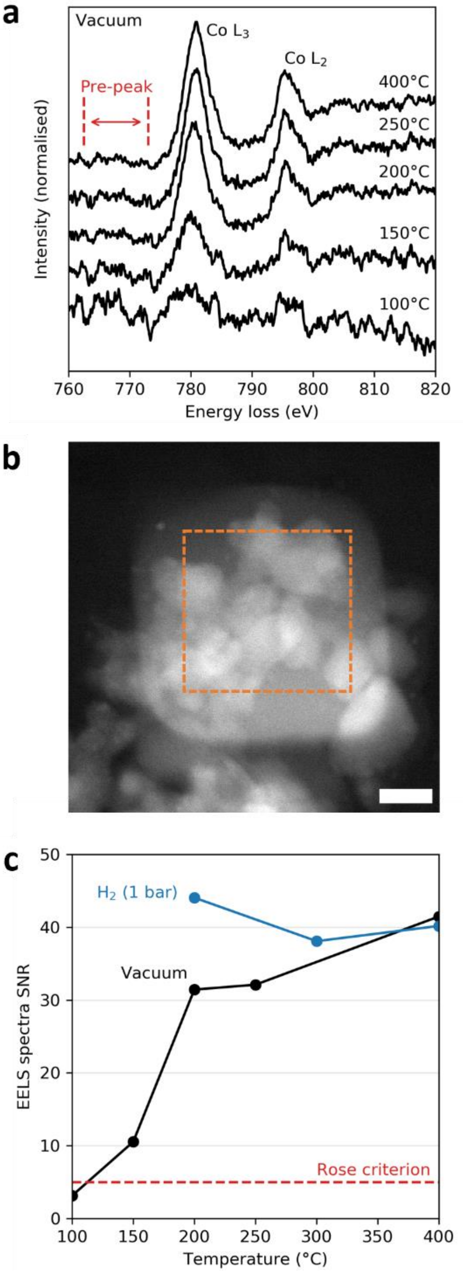

Figure 6.4: Temperature effect on SNR of EELS spectra of unsupported Co_3O_4 NPs in the gas E-cell. (a) *Summed EELS acquisitions at increasing E-cell temperatures at vacuum showing increasing Co L_3/L_2 strength relative to the background signal.* ***(b)*** *HAADF-STEM image of the Co_3O_4 NPs showing the square of contamination drawn by the electron beam during EELS acquisition at 150°C in the ROI (highlighted by the orange dashed square). Scale bar = 40 nm.* ***(c)*** *SNR plots calculated from the EELS spectra in (a) demonstrating the lower SNR at lower significant effect of contamination on Co signal strength at low temperatures. The full EELS data set is shown in SI Figure 6.7.*

($I_{Co\,L3}/\Delta I_{Co\,prepeak}$). Higher SNR is observed at higher temperatures with a significant loss of SNR below 200°C. Different particles were analyzed for each temperature and we hypothesize that at temperatures <200°C the signal degradation is dominated by a beam induced contamination layer (likely composed of hydrocarbons). Sample contamination is commonly noted as an undesirable artefact of E-cells[10,14] and we observe this to be significant at temperatures <200°C, despite use of high purity gas feeds (H_2 = 99.9995%) and the use of pump-purge cycles. Contamination is generally lower at lower gas pressures but despite acquiring the data in **Figure 6.4a** after evacuating the E-cell to vacuum, a solid contamination layer was still observed for EELS acquisitions at temperatures of 100 and 150°C as shown in **Figure 6.4b.** No significant contamination is seen above ~200°C as demonstrated in SI Figure 6.7h-j. To reduce contamination, similar data was acquired with a reducing atmosphere (H_2 gas, 1 bar) and for temperatures ≥200°C (blue line in **Figure 6.4c**). In the absence of contamination, it was possible to acquire data for the identical NP region of interest and thereby remove any chance of local thickness variation causing variability in the SNR results. This data revealed a 40% higher SNR at 200°C compared to the cell containing vacuum, converging to the same value at 400°C.

To enhance EELS signal detection, all spectra in **Figure 6.4** have been collected and summed from a relatively large region of interest (138 nm by 138 nm), with an electron flux sufficient to provide clear spectral peaks without damaging the specimen. The summation of the spectral data across the region of interest (ROI) increases the SBR and SNR, but at the expense of spatial resolution. One of the key strengths of STEM-EELS versus X-ray methods for elemental or oxidation state analysis is the potential for (sub)nanometer spatial resolution.[15] Thus, it is highly desirable to use EELS to acquire the specimen core-loss edges from a ROI and then to calculate a map of the oxidation state from the complete spectrum image. In practice the limited SNR/SBR often requires the pixelated EELS spectrum image to be binned beyond the desired spatial resolution, so as to achieve confidence in the interpretation of the data. This is particularly true for small nanoparticles or elements with weaker EELS core-loss edges at high energy loss. Nonetheless, even summed/binned data can provide useful analysis

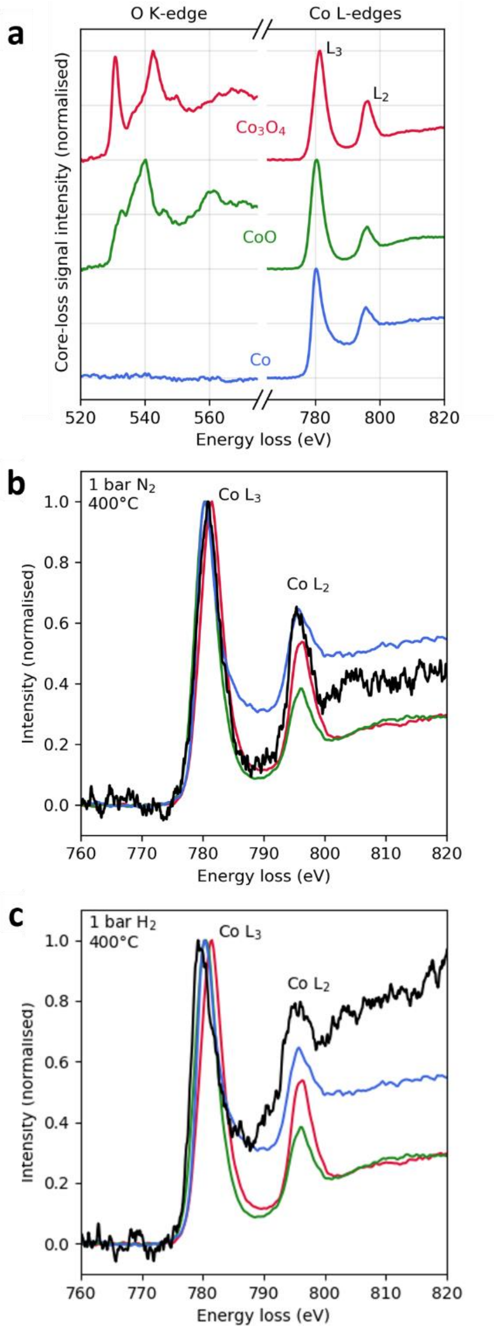

Figure 6.5: STEM-EELS analysis of the oxidation state of Co-containing nanoparticles during in situ gas cell reduction. (a) *STEM-EELS acquisitions of standard reference oxide and metallic samples for comparison to the specimen data.* ***(b,c)*** *Spectra collected for unsupported Co_3O_4 heated to 400°C for 15 minutes* ***(b)*** *in inert N_2 (1 bar) and* ***(c)*** *in H_2 (1 bar). Experimental data is indicated by the black line while the reference spectra is shown by red, green and blue for Co_3O_4, CoO and Co respectively. Heating in N_2 the sample is still Co_3O_4 whereas heating in H_2 produces Co metal. The post-edge background tails are significantly higher than the references in both in situ EELS data sets as a result of the increased background intensity induced by the presence of the Si_3N_4 windows.*

of local oxidation state as demonstrated for the reduction of Co_3O_4 particles to CoO and Co in **Figure 6.5**, complemented by higher spatial resolution HAADF-STEM imaging, which provides correlative local information such as particle size distribution.

Conclusions

The development of *in situ* gas E-cell (S)TEM holders provides new opportunities for studying the dynamic behaviour of heterogeneous catalysts during exposure to industrially relevant environmental conditions. However, these innovative approaches also bring new challenges, which much be addressed if they are to fulfil their full potential. In this work, *in situ* STEM-EELS was used to quantitatively assess the effect of temperature and gas pressure on the quality of EELS spectra acquisition, and to understand the principal origins of the observed loss of signal quality. The results reveal the overwhelming impact that the Si_3N_4 windows have on the SNR and SBR of EELS spectra. Calculations of the equivalent SiN thickness from the N_2 gas component shows that this also contributes to reduced peak intensity, but the effect is an order of magnitude lower than the contribution from the membrane windows and is reduced even further at the elevated temperatures typically used in heterogeneous catalysis. It was also demonstrated that the SNR can be improved through the spectra summation to provide an averaged spectrum, enabling useful analysis of the overall oxidation state of an industrially relevant Co nanoparticle catalyst, albeit at the expense of loss in spatial resolution. Further improvement of the SNR and consequently the achievable spatial resolution in current gas E-cell designs requires modifications to the membrane windows. For example, recent advances using graphene as the membranes for liquid E-cells may also be utilized in gas E-cells to reduce the thickness of the windows and improve the SNR of *in situ* EELS analysis.[16,17]

Experimental Section

Co_3O_4, CoO and Co metal NP catalyst reference samples were acquired from Sigma Aldrich. Samples were prepared for STEM-EELS by grinding to a fine powder. Dispersion in methanol allowed drop casting the NPs onto the Si_3N_4 membrane window of the *in situ* gas E-cell (illustrated in **Figure 6.1a**). The Protochips Atmosphere™ gas cell system was employed to perform *in situ* experiments. The top chip provides pre-calibrated heating to the sample via electrical contact to the SiC membrane and is temperature controlled using the Protochips Clarity software. The bottom chip contains spacers of controlled thickness which sit against the top chip to provide a 5 µm high channel through which gas can be held/flowed.

Scanning transmission electron microscopy (STEM) was performed using an aberration-corrected FEI Titan G2 80-200 ChemiSTEM (Thermo Fischer Scientific) operating at an accelerating voltage of 200 keV. High-angle annular dark field (HAADF) STEM imaging was undertaken using 90 pA probe current, 20 µs dwell time and 21 mrad convergence semiangle. Electron energy loss spectroscopy (EELS) was acquired using a GIF Quantum ER System (Gatan Inc.) with 0.1-0.5 eV/channel dispersion. Dual EELS collection was collected using dwell times of 10 µs for the zero-loss spectrum and 0.05-0.2s for the core-loss spectral acquisitions. Statistical and spectroscopic analysis was performed using Python packages (Numpy, Scipy and Hyperspy[18]).

Supporting Information

Determining the Limits of Electron Energy-Loss Spectroscopy Analysis of Heterogeneous Catalysts during *In Situ* Gas Cell Scanning Transmission Electron Microscopy

Matthew Lindley[1], James Paterson[2], Chris Hardacre[3], Sarah J. Haigh[1]

[1] School of Materials, University of Manchester, Oxford Road, Manchester, M13 9PL, United Kingdom

[2] BP, Saltend Chemicals Park, Hull, HU12 8DS, United Kingdom

[3] School of Chemical Engineering and Analytical Science, University of Manchester, Oxford Road, Manchester, M13 9PL, United Kingdom

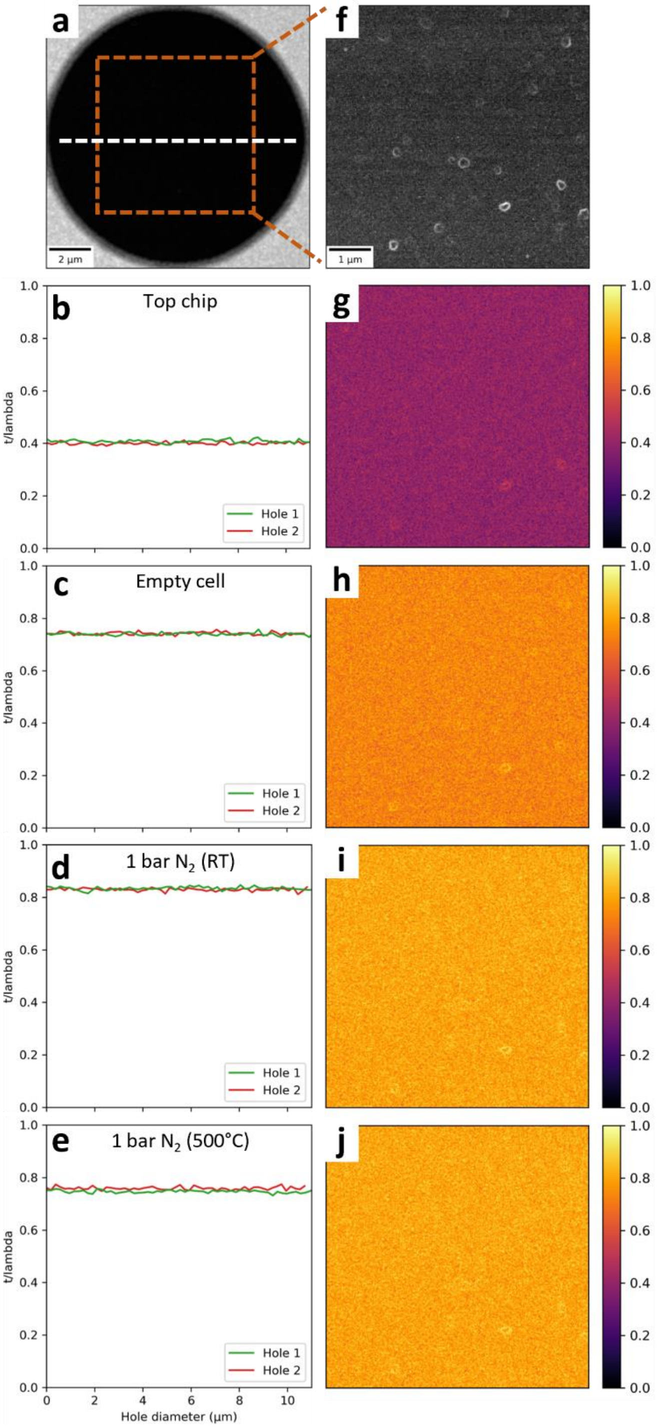

Figure 6.6: Relative t/λ measurements of the E-cell (no specimen). (a) *HAADF-STEM image of the top chip Si_3N_4 membrane window which span the circular voids etched into the SiC heater.* ***(b-e)*** *t/λ plots from the top chip, the fully constructed empty cell containing vacuum, 1 bar of N_2 at room temperature, and 1 bar of N_2 at 500°C, respectively calculated from EELS line profiles taken across the window in the position of the white dotted line in (a). Two holes were investigated to aid confidence in the results.* ***(f)*** *HAADF-STEM image of the ROI highlighted by orange dotted square in (a). Areas of relatively high intensity in the image indicate regions with varying Si_3N_4 membrane thickness.* ***(g-j)*** *Relative t/λ maps acquired from the localised ROI in (f) for the same gas E-cell conditions as described for* (***b-c)*** *in the top row.*

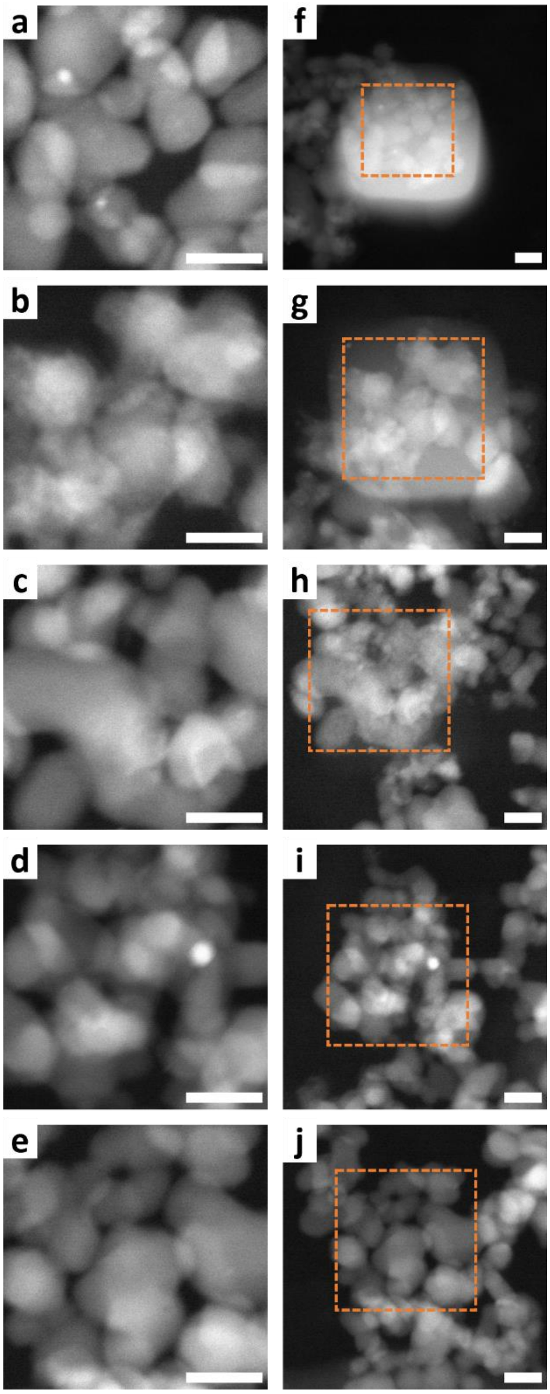

Figure 6.7: HAADF-STEM image series demonstrating the temperature dependence of beam induced contamination build-up during EELS acquisition at low gas pressure *(~1 mbar* N_2*).* ***(a-e)*** *Images of the individual ROIs used for the vacuum EELS data in Figure 4, showing the* Co_3O_4 *catalyst nanoparticles before STEM-EELS at temperatures of (a) 100°C, (b) 150°C, (c) 200°C, (d) 250°C and (e) 400°C.* ***(f-j)*** *Corresponding lower magnification images after EELS acquisition, where the increased intensity in the analyzed ROI shows the build-up of contamination (orange dashed squares highlight the region of acquisition). Contamination effects are much less obvious above 200°C. Scale bars = 40 nm.*

Bibliography

1. Somorjai, G. A. & Li, Y. *Introduction to surface chemistry and catalysis*. (John Wiley & Sons, 2010).

2. Tao, F. & Crozier, P. A. Atomic-Scale Observations of Catalyst Structures under Reaction Conditions and during Catalysis. *Chem. Rev.* **116**, 3487–3539 (2016).

3. Morales, F. *et al.* Mn promotion effects in Co/TiO2 Fischer-Tropsch catalysts as investigated by XPS and STEM-EELS. *J. Catal.* **230**, 301–308 (2005).

4. Egerton, R. F. & Malac, M. EELS in the TEM. *J. Electron Spectros. Relat. Phenomena* **143**, 43–50 (2005).

5. Tan, H., Verbeeck, J., Abakumov, A. & Van Tendeloo, G. Oxidation state and chemical shift investigation in transition metal oxides by EELS. *Ultramicroscopy* **116**, 24–33 (2012).

6. Sharma, R. An environmental transmission electron microscope for in situ synthesis and characterization of nanomaterials. *J. Mater. Res.* **20**, 1695–1707 (2005).

7. Sharma, R. Design and applications of environmental cell transmission electron microscope for in situ observations of gas-solid reactions. *Microsc. Microanal.* **7**, 494–506 (2001).

8. Wu, J. *et al.* In Situ Environmental TEM in Imaging Gas and Liquid Phase Chemical Reactions for Materials Research. *Adv. Mater.* **28**, 9686–9712 (2016).

9. Creemer, J. F. *et al.* Atomic-scale electron microscopy at ambient pressure. *Ultramicroscopy* **108**, 993–998 (2008).

10. Allard, L. F. *et al.* Novel MEMS-based gas-cell/heating specimen holder provides advanced imaging capabilities for in situ reaction studies. *Microsc. Microanal.* **18**, 656–666 (2012).

11. Zhu, Y. & Browning, N. D. The Role of Gas in Determining Image Quality and

Resolution During In Situ Scanning Transmission Electron Microscopy Experiments. *ChemCatChem* **9**, 3478–3485 (2017).

12. Suzuki, M., Yaguchi, T. & Zhang, X. F. High-resolution environmental transmission electron microscopy: modeling and experimental verification. *Microscopy* **62**, 437–450 (2013).

13. Xin, H. L., Niu, K., Alsem, D. H. & Zheng, H. In situ TEM study of catalytic nanoparticle reactions in atmospheric pressure gas environment. *Microsc. Microanal.* **19**, 1558–1568 (2013).

14. Vendelbo, S. B. *et al.* Method for local temperature measurement in a nanoreactor for in situ high-resolution electron microscopy. *Ultramicroscopy* **133**, 72–79 (2013).

15. Gloter, A. *et al.* Atomically resolved mapping of EELS fine structures. *Mater. Sci. Semicond. Process.* **65**, 2–17 (2017).

16. Min, Y. J. *et al.* High-Resolution EM of Colloidal Nanocrystal Growth Using Graphene Liquid Cells. *Science (80-.).* **336**, 61–64 (2012).

17. Kelly, D. J. *et al.* Nanometer Resolution Elemental Mapping in Graphene-Based TEM Liquid Cells. *Nano Lett.* **18**, 1168–1174 (2018).

18. Peña, F. de la *et al.* hyperspy/hyperspy: Release v1.6.5. (2021) doi:10.5281/ZENODO.5608741.

Chapter 7

Summary and Future Work

The motivation for this research was to apply recent developments in *in situ* gas cell scanning transmission electron microscopy (STEM) to study Co-Mn/TiO_2 catalysts, industrially important to Fischer-Tropsch (FT) synthesis. This was achieved through two project aims: the first investigating the influence of Mn as a promoter for Co/TiO_2 catalysts and its impact on the morphological and chemical transformations during a H_2 reduction treatment; the second establishing limitations of the current silicon nitride membrane window design of the gas cell when performing electron energy loss spectroscopy (EELS).

The main objective in studying Co-Mn/TiO_2 catalysts was to directly observe the response to an industrially relevant reduction process in order to gain insights into the environmentally-induced transformations before FT reactions initiated. Reactions in heterogeneous catalysis often benefit from maximising surface area, and therefore nanoparticle catalysts should display a dispersion sufficient for an effectively high turnover. However, dispersion of supported catalysts for the FT process often changes during synthesis due to differences in the calcination, reduction, and reaction process environments. The complexity of nanoparticle dispersion is further complicated by use different synthetic approaches (for example, wet impregnation, co-precipitation, or sol-gel methods). Characterising these transformations and establishing structure-activity relationships is crucial in providing step-changes in the design of more efficient Fischer-Tropsch catalysts. We demonstrated, for wet impregnation of a mixed Co-Mn precursor solution, the inclusion of Mn leads to significantly greater dispersion of Co upon calcination, relative to the unpromoted variant. During the reduction treatment we observed the relatively large porous cobalt clusters in the Co/TiO_2 specimen to fragment, redisperse, sinter and eventually coalesce into very large densified particles. In addition, much smaller Co particles started to form on the support at higher temperatures, suggesting sintering of residual atomic Co on the support surface. The exhibition of poor stability towards the reduction treatment is diminished for the Mn promoted catalyst, in which the high dispersion of Co led to a much narrower distribution of particle sizes close to that which show ideal activity toward FT conversion.[1] DFT calculations revealed the inclination for surface migration of Co across the support, while the opposite was true for Mn, agreeing with the in situ observations showing segregation of Co and Mn during reduction and Mn to remain heavily dispersed on the support. The result is Co particle formation which remains in close proximity to the Mn dispersion, the relationship of which has been shown previously to be crucial to the observed selectivity shift.[2]

The second aim of this project was to demonstrate the influence of gas pressure, temperature and the presence of membrane windows on the acquisition of EELS data. The results show the overwhelmingly significant contribution to electron scattering in the gas cell to arise from the ~80 nm combined thickness of silicon nitride, which can lead to high-energy core-loss edge intensities to be reduced to that of the spectrum noise. It is clear that further development in gas cells to allow sufficient EELS signal acquisition will need to arise from replacement of the silicon nitride as a membrane material. The replacement material will ideally consist of a ‘light’ atomic structure (i.e., consisting of low atomic number elements) while simultaneously displaying strong mechanical properties to accommodate the encapsulating gas pressure. 2D materials, such as graphene, are seen as a potential replacement and have already been used to fabricate liquid cells, demonstrating higher resolution imaging capabilities due to the constituting carbon composition having a low cross-section of interaction with the electron beam probe.[3] Similar advances have been made using hexagonal boron nitride (h-BN) to observe the vibrational properties of liquid water.[4] As such, it is to be expected that the extensions of these, and similar materials, will lead to substantial advances in EELS acquisition in the gas cell.

Bibliography

1. Bezemer, G. L. *et al.* Cobalt particle size effects in the Fischer-Tropsch reaction studied with carbon nanofiber supported catalysts. *J. Am. Chem. Soc.* **128**, 3956–3964 (2006).

2. Paterson, J. *et al.* Manipulation of Fischer-Tropsch Synthesis for Production of Higher Alcohols Using Manganese Promoters Higher Alcohols using Manganese Promoters. (2018).

3. Kelly, D. J. *et al.* Nanometer Resolution Elemental Mapping in Graphene-Based TEM Liquid Cells. *Nano Lett.* **18**, 1168–1174 (2018).

4. Jokisaari, J. R. *et al.* Vibrational Spectroscopy of Water with High Spatial Resolution. *Adv. Mater.* **30**, 1802702 (2018).